Ultrafast modification of the magnetic anisotropy in a CoTb alloy

Alaa El Dine Merhe

Sorbonne Université

ED 388 Chimie Physique et Chimie Analytique de Paris-Centre

Laboratoire de Chimie Physique Matière et Rayonnement / Systèmes fortement corrélés-Matériaux magnétiques

Ultrafast modification of the magnetic anisotropy in a CoTb alloy

Par Alaa el dine MERHE

Thèse de doctorat de [Chimie Physique]

Dirigée par Prof. Jan LÜNING et Dr. Boris VODUNGBO

Présentée et soutenue publiquement le [--/11/2018]

Devant un jury composé de :

Mme. Bénédicte Warot-Fonrose	Chargée de Recherche	Université Paul Sabatier	**Rapporteur**
M. Marco Cammarata	Chargé de Recherche	Université de Rennes	**Rapporteur**
Mme. Valérie Halte	Professeur	Université de Strasbourg	**Examinatrice**
M. Franck Vidal	Maître des conférences	Sorbonne Université	**Examinateur**
M. Hamed Merdji	Directeur de Recherche	CEA	**Examinateur**
M. Jan Lüning	Professeur	Sorbonne Université	**Directeur de thèse**

Je dédie cette thèse aux camarades

du passé, du présent et du futur

Remerciements

Ce travail de thèse a été réalisé au sein de l'université de Sorbonne dans le Laboratoire de Chimie Physique Matière et Rayonnement (LCPMR). Je remercie tout le personnel de laboratoire pour l'ambiance agréable qu'y règne, surtout David Massot pour m'avoir aidé dans toutes les démarches administratives.

Je tiens à remercier grandement Boris Vodungbo, Maitre de conférences à l'Université de Pierre et Marie Curie, qui m'a encadré tout au long de cette thèse et qui m'a fait partager ses brillantes idées. En outre de son appui scientifique, il a toujours été là pour me soutenir et me conseiller au cours de la réalisation de ce travail.

Je remercie également mon directeur de thèse, Professeur Jan Luning, de m'avoir guidé et conseillé tout au long de la thèse, de m'encouragé dans différents situations ainsi de me déléguer pour de nombreuses missions notamment les temps faisceaux, tout en me laissant une grande liberté.

Je tiens à remercier aussi toute les membres de l'équipe « Systèmes fortement corrélés-Matériaux magnétiques » pour leur accueil et leur sympathie. Je pense également à Emmanuelle Jal qui a toujours fait tout son possible pour aider.

Je remercie tous les collaborateurs internationales que j'ai eu la chance de travailler avec eux pendant ces trois années. Je pense particulièrement à Dr Gregory Malinowski et Dr Marwan Deeb de l'Institut Jean Lamour à Nancy, Dr Clemens von korff Schmising et Dr David Weder de Max-Born-Institut à Berlin, Dr Benedikt Rösner et Dr Adam Kubec de Paul Scherrer Institut à Zürich, Dr Flavio Capotondi de FERMI à Trieste, Dr Marion Kuhlmann de Deutsches Elektronen-Synchrotron à Hambourg.

J'adresse tous mes remerciements à Madame Bénédicte Warot-Fonrose, chargée de recherche au Centre d'Élaboration de Matériaux et d'Etudes Structurales, ainsi qu'à Monsieur Marco Cammarata, chargé de recherche à l'Institut Physique de Rennes, d'avoir accepté d'être les rapporteurs de ma thèse. Merci également à Monsieur Hamed Merdji directeur de recherche au CEA, à Franck Vidal maitres de conférences à l'UPMC, ainsi qu'à Madame Valérie Halte professeur à l'université de Strasbourg pour examiner ce manuscrit.

Je remercie tous les thésards du LCPMR pour les nombreux bons moments passés ensembles ainsi que pour la bonne ambiance de travail. Merci en particulier aux collègues de bureau exceptionnel 111, Carla Alves, Jiatai Feng, Meiyi Wu, Mehdi Khalal, Moustafa Zmerli et Xuan Liu, pour l'amusement que nous avons partagé ces trois dernières années. Nous sommes devenus amis.

A titre plus personnel, mes remerciements vont aussi à mes amis « hors Labo » avec qui j'ai pu passer des très bons moments : Christian ; Abbas, Ahmad, Alaa, Alexa, Ali, Amal, Assil, Fanny, Florian, Floriane, Fatima, Francesco, Grégoire, Hassan, Hannen, Haytham, Ibrahim, Ivette, Jessica et Samir, Joanna, Julien, Kev, Leila, Mohamad, Nida, Noujoud, Safaa, Sandra, Sarah, Thouraia,Rabih et Razan, Ram, Rami, Rana, Rayane, Rim, Rofie, Yasmine, Zeinab.

Je remercie chaleureusement ma chère Imane pour son soutien moral ininterrompu tout au long de la rédaction de cette thèse. Merci pour les très bons moments que tu m'as faits passer.

Enfin, mais non des moindres, tous mes remerciements à ma famille qui m’ont apporté toute leur aide quand j’en ai besoin. J'ai eu la chance de grandir dans deux familles. Merci à Bou Kassem, Bou Ali, Amal, Sawsan, Mimo, Ace, Aloush, Dado, Hassun, Safi and Hamoudi.

Paris,

Aladine MERHE

Contents

1 Introduction and overview

The manipulation of the magnetic order by ultra-short laser pulses is a very active area of research today. Ultrafast demagnetization is the fast significant loss of the magnetization when a magnetic layer is excited by a femtosecond optical pulse. This process was firstly observed by Beaurepaire *et al* in 1996 [1]. They showed that a strong femtosecond laser pulse can demagnetize a nickel thin film in less than 1ps. This observation was quickly confirmed by numerous studies showing an ultrafast drop of the magnetization in various materials. About a decade later, it was discovered that in some materials this ultrafast demagnetization triggers an all-optical switching of the magnetization [2]. This control of the magnetization reversal is of a strong technological interest because it could lead to advanced applications for magnetic storage of information.

Ultrafast magnetization dynamics has been intensely investigated to answer questions about the speed of the magnetic reorientation in a material and about the physical process behind this observation. Despite many experimental results obtained over the last 20 years, the physics of ultrafast magnetism is still poorly understood. On the femtosecond timescale, the material is excited in a non-equilibrium state where a thermodynamic description of the system is no longer valid. To understand these ultrafast phenomena, two questions must be answered. How the energy flow to the spin system in such a short time? How the angular momentum (magnetization being a form of angular momentum) is transferred out of the spin system to conserve total angular momentum?

Many studies and models have been proposed to answer these questions and explain the ultrafast behavior of magnetization. The two models that have been widely discussed are Elliot-Yafet electron phonon scattering [3] accompanied with spin flips events and the super diffusive spin transport [4] where spins are spatially redistributed without requiring any spin flip. Recent experiments suggest that both phenomena could occur simultaneously [5].

Using X-ray to investigate ultrafast magnetization dynamic has been rendered possible by the development of synchrotron femto-slicing, High Harmonic Generation (HHG) and Free Electron Laser sources [6]. Due to their short wavelength, X-rays offer a nanometer spatial resolution and high penetration depth. In addition, core-level electrons are accessible by X-rays. This opens the possibility of investigating the magnetism of different elements selectively. Due to the availability of highly brilliant X-ray sources, investigation of the

magnetic materials in the soft and hard X-ray becomes feasible. In this thesis, I will concentrate on the ultrashort and bright X-ray pulses generated from FEL sources.

During the last 30 years, several X-ray techniques have been developed to investigate magnetic microstructures. One of these techniques for studying nanomagnetic structure is based on the magnetic resonant X-ray scattering. This technique provides information on the collective behavior of the nanomagnetic structure and gives global statistical information. Using this technique we can extract the characteristic average properties of the material such as the average domain size, the correlation length and etc. In our studies we used the resonant small angle X-ray scattering technique.

My work focused on the investigation of ultrafast demagnetization in materials for which some composition show an all optical switching of the magnetization. To understand the dynamic induced by the ultrashort laser pulse, we studied Transition Metal-Rare Earth alloys. The magnetic structure of our sample consists of alternative up and down magnetic domains aligned along the same direction with an out of plane magnetization, forming a network of stripe domains. The boundaries between differently magnetized regions are purely magnetic and called domain walls. The response of those walls to an ultrafast excitation become an interesting aspects to follow in the field of ‘‘femto-magnetism’’, since basic magnetic properties – such as intensity of exchange interaction and anisotropy energy are directly governing the internal domain wall structure and domain wall density[7], [8].

In order to examine the effect of the superdiffusive spin transport, Pfau *et al* [9] studied the temporal evolution of the magnetization of a Co/Pd multilayer film exhibiting a labyrinth-like network of oppositely-magnetized domains. Authors proposed that an ultrafast spin transport between the opposite domains induces a spatial modification of the domain walls structure. This widening of the domain wall has also been reported recently by Sant *et al* [10] . From this point of view, magnetically ordered regions in different materials play an important role in these ultrafast phenomena[11]. To study in details this widening of the domain wall and probe magnetic domain dynamics, we employed the resonant small angle X-ray scattering method. For each pump-probe time delay the magnetic scattering is recorded on the CCD detector. This makes it possible to study the temporal evolution of the magnetic domain structure. It is shown that by using suitable models for the interpretation, information on the magnetic domain wall can be extracted. We report here an ultrafast increase of the domain wall thickness, which is not implied by a super-diffusive spin transport but by an ultrafast decrease of the uniaxial anisotropy value.

Below is the outline of my thesis:

Chapter 1 describes the basic concepts for understanding this thesis and introduces the fundamental principles of ultrafast demagnetization.

Chapter 2 discusses the fabrication of magnetic thin films by sputtering ('magnetron sputtering') and the characterization of their structural and magnetic properties (MOKE, SQUID, ...). At the end of this chapter we present the magnetic systems studied in this thesis.

Chapter 3 describes the interaction of X-rays with magnetic materials. First, we present the different sources of X-rays and more particularly the characteristics of free electron lasers (FEL). The main notions concerning the diffusion of X-rays by magnetic materials are given in order to link the diffused intensity to the magnetization of the studied sample.

Chapter 4 presents a resonant small angle X-ray scattering experiment on a CoTb alloy. The chapter begins with a description of the setup and DiProI line parameters. Subsequently, the experiment itself is described, followed by the analysis of the experimental results. Two different models are presented to analyze the different scattering orders detected on the CCD. From these models we can extract the domain wall width for each time delay and we propose that the time evolution of this width is link to a drop in uniaxial anisotropy. At the end, we present the temporal evolution of the different scattering order of a Co/Pt multilayer.

During my PhD, I also participated in several experiments realized at different XFEL installations. Some of the results obtained are presented throughout the manuscript and in the appendix.

1 Mechanism of ultrafast demagnetization

1.1 History of magnetism

The history of magnetism dates back to earlier than 600 b.c. and the first technological applications of magnetized materials, as compass needles, was in the 10^{th} century by Chinese sailors[12]. Magnetism plays a very important role in some very advanced technologies widely used today. One of the most significant discoveries in this field was the electromagnetic induction at the end of the 19^{th} century. This discovery pioneered a huge development in the industrial production of electric power generators. Another important invention was the magnetic tape recording [13]; Thanks to this technology, information like sounds could be recorded using magnetized areas on a plastic tape with a magnetic coating on it. This opened the area of magnetic data storage, featuring a write-read cycle life of information. Since then, a great deal of research effort was devoted to improve data storage technologies.

Magnetic recording materials present magnetic domains that can be aligned along a specific direction. This magnetic orientation can be modified by applying an external magnetic field. For example, the orientation state of any magnetic nanograin “up” or “down” could corresponds to ‘0’ or ‘1’ in the binary number system. This allows storing bits of information. The ability of making very small grains of magnetic materials has led to useful development of the storage devices particularly in terms of speed and capacity.

The traditional method to reverse the magnetic orientation is by applying a magnetic field in the opposite direction. In order to increase the data storage density one should think about decreasing the size of magnetic grains down to the nanometer scale. At this scale, the grain volume is so small that the thermal energy becomes comparable to the magnetic energy: the magnetic information is rapidly lost due to the thermal agitation; this is known as the superparamagnetic limit. Hence it is necessary to increase the anisotropy constant value – which increases the magnetic energy – to preserve the magnetic state of the grain. Unfortunately, this also increases the magnetic field necessary to reverse the magnetization which at some points in miniaturization becomes impossible to obtain with a tiny integrated electromagnet. To overcome this limitation many solutions were proposed and presented in Figure 1-1: Diagram presenting different magnetic recording devices. In Heat Assisted

Magnetic Recording devices(HAMR) [14], a laser is applied to heat the magnetic materials causing a decrease in the coercive field: hence a small magnetic field can reverse the magnetization. Another device is the Microwave Assisted Magnetic Recording (MAMR)[15], where microwaves lower the barrier energy between two opposite states and thus a small external magnetic field can change the bit orientation. Also, the use of multiferroic materials could provide a solution to this problem. Indeed, these materials have the ability to be both electrically charged (ferroelectric) and magnetically ordered (ferromagnetic). In some cases both of these orders are coupled and an applied electric field could reverse the magnetization much more efficiently than an external magnetic field [16]. However, these materials are complex and their behaviors upon external excitation are not very well understood.

Another path for future magnetic storage devices would be the all optical control of magnetization. Indeed, in 2007 all optical switching of the magnetization was discovered [2]. This could lead to the fastest and smallest storage devices. In all optical switching, the domain magnetization is reversed only by applying an ultrashort laser pulse, without the need of an external magnetic field or a spin current. However, the mechanism of switching is not yet understood despite all studies that discussed it. However, many groups investigating this phenomena postulate that it originates from the initial ultrafast demagnetization [17] the rapid loss of magnetization which occurs within the first few hundreds of femtosecond after optical excitation.

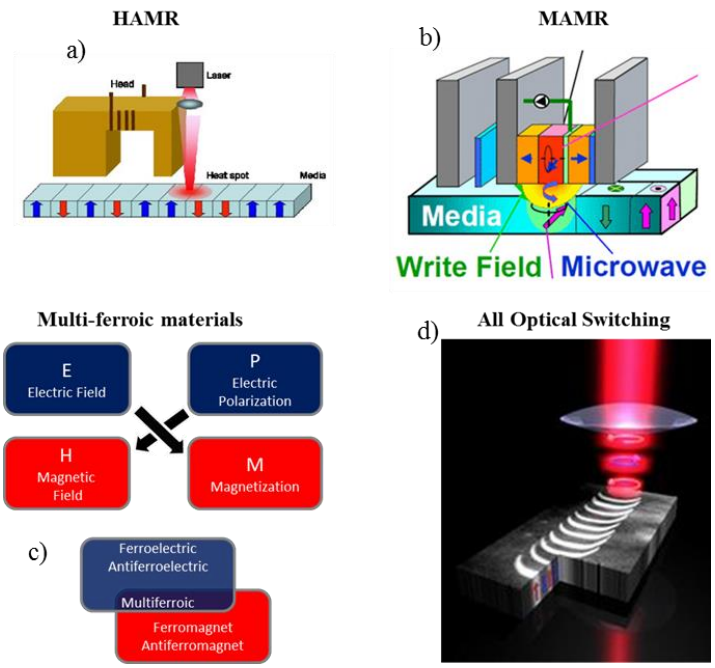

Figure 1-1: Diagram presenting different magnetic recording devices

1.2 Microscopic point of view of magnetization

1.2.1 Atomic origin of magnetism

The magnetic moment of an atom is mainly due to electrons orbiting this atom. The magnetic moment of the nucleus is a factor 1000 smaller than that of the electron [18]. Electrons are making orbital motions according to Bohr's atomic model and spin rotations as proposed by Uhlenbeck and Goudsmit [19]. A magnetic moment appears due to the charged electron rotating periodically around a nucleus. Similar to the magnetic field generated when current flows in solenoid coils. This is known as the orbital magnetic moment $\vec{m}_L$. Or, this value is not high enough to explain the magnetic moment detected experimentally. Another contribution in the total magnetic moment comes from an intrinsic angular momentum of the electron: the spin. This was proposed to explain experimental observations like the experiment of Stern and Gerlach. It is known as the spin magnetic moment $\vec{m}_S$ which is added to the $\vec{m}_L$ to give the total magnetic moment:

$$\vec{m} = \vec{m}_L + \vec{m}_S$$

This magnetic moment generated from the orbital and spin contribution of a single electron is represented as a function of the Bohr magnetron which is the smallest unit of solids magnetic

moment with $\mu_B=\frac{e\hbar}{2m}$. Where e is the elementary charge, ħ is the reduced Planck constant and m_e is the electron rest mass.

In atoms, according to Hund's rule, electrons occupy orbitals in a way that maximize the total spin moment. We also know from the Pauli Exclusion Principle that two identical fermions cannot occupy the same quantum state within a quantum system simultaneously. Since electrons are fermions, then two electrons occupying the same orbit should display opposite spin orientations (up or down). In other words most of isolated atoms carry a magnetic moment. The question that arises is: what will happen with this atomic magnetic moment during solid formation?

1.2.2 Magnetism: From atoms to solids

During the formation of molecules or solid the interatomic bonds often leads to the compensation of the spin magnetic moment. Most of the angular momentum generated from electrons spins cancel each other and does not contribute to the solid magnetic moment. In some cases, however, (mostly for transition metals or rare earth compounds) some electrons remained unpaired in the solid state. The magnetic moments of these unpaired electrons can either remain isolated and interact only with external magnetic fields (paramagnetism) or interact with one another and give rise to long range magnetic orders (ferromagnetism and antiferromagnetism), as we will show later in section 2.2.3.

In solids, electrons are distributed over the whole crystal rather than localized at an atom; therefore, the magnetic moment is better described by considering band structure but not the Hund rule like in atoms. In the band structure theory, the Stoner Wohlfarth model in its simplest version considers free electrons where energy level are filled up to the Fermi radius with $k_f =$ and$\frac{N}{V}$ being the electron density.

A non-magnetic ground state intimates that all states up to the Fermi energy E_f are filled with two electrons carrying an opposite spins.[18], [20] [21]. While for magnetic states, due to the Coulomb interaction and the Pauli principle, an exchange interaction originates between opposite spins[20].This effect induces an imbalance between spin up and spin down electrons in a way that one band presenting a specific spin configuration contains more electron(majority) than the other band presenting the opposite spin configuration (minority).Thus, introducing an exchange interaction shifts the energy level of minority to

higher energies, while the energy level of majority spin electrons is shifted downwards. This relative shifts between the majority and minority state is responsible for the formation of the magnetic moment. From a microscopically point of view, magnetism is the result of the minimization of the sample global energy. This energy is directly related to four types of interactions as we will show in the following parts.

1.2.2.1 Magnetocrystalline anisotropy

Due the bonding process, the spherical symmetry of the atom is broken in a form that the corresponding orbital magnetic moment becomes aligned to preferred lattice directions. The spin orbit interaction orients the electrons spin in certain direction, called easy axis. To magnetize the solid in this direction requires a lower energy than in any other directions (hard axis). This energy term is called the magneto-crystalline anisotropy energy. If magnetic moments in materials are easy aligned towards only one easy axis then the material is said to have uniaxial anisotropy. Otherwise if the magnetic moments can go along several different easy directions then the material possess a cubic anisotropy. In this thesis we are interested in systems presenting uniaxial crystal symmetry where the corresponding anisotropy energy responsible in rotating the moment away from the easy axis can be written as [22] :

$$E_a \approx K_u \sin^2 \theta \qquad 1.1$$

with K_u the uniaxial anisotropy constant and θ the angle between the magnetic dipole and the easy axis.

1.2.2.2 Dipolar energy

One also notes the contribution of the magneto static dipolar energy. The exchange and anisotropy energies would lead to a uniform magnetization throughout the object, with all atomic moments aligned along the easy direction. The magnetization can also interact with the magnetic field generated by the magnetic free poles at the surface of the material itself. To simplify things, let us consider the case of a film that has a finite size. The magnetic dipoles in the film create the stray field. Due to the surface charging inside the film a demagnetizing field showing the same amplitude of the stray field but directs opposite to the magnetization is created. The magneto static energy is described here using $\vec{M}$ the magnetization and $\vec{H}_d$the demagnetizing field.

$$E_d = \int -\mu_0 \frac{1}{2} \vec{H}_d * \vec{M} \; dV \qquad 1.2$$

In order to minimize the magneto static energy, most of magnetic materials tend to break into multiple magnetic domains with different orientations of magnetization as we will show later [23]. In the case of ultra-thin films (< 10 nm) this effect becomes energy dominant and thus induces anisotropy of form.

1.2.2.3 Zeeman energy

Another contribution is the Zeeman energy which accounts for the interaction between an external applied magnetic field and the material's magnetization. The Zeeman energy is represented as an integral over the magnet volume

$$E_z = \mu_0 \int \vec{M}.\vec{H}ext \; dV \qquad 1.3$$

where Hext is the external field. This energy reaches a minimum when the magnetization is parallel with the applied external field.

1.2.2.4 Exchange interaction

The exchange interaction comes from the direct interaction between two neighboring magnetic moments whereby individual magnetic moments will attempt to align all other atomic magnetic moments. The exchange energy is given by this form:

$$E_{ex}^{i,j} = -J_{ij}\overrightarrow{S_\iota} * \overrightarrow{S_J} \qquad 1.4$$

where $\overrightarrow{S_\iota}$ and $\overrightarrow{S_J}$ are the unit vectors of the two interacting spin and J_{ij} is the exchange integral with J>0 indicates a parallel arrangement of two moments, and J<0 leads to an antiparallel alignment of the two moments. This interaction will lead to the magnetic ordering of the materials and is considered as the origin of the spin system alignments. It can be a short range interaction (direct exchange) or long range interaction (super exchange).More bibliographies on this subject can be found in [24].

It's very important to highlight here on the Curie temperature which is one characteristic of magnetic materials. Above this temperature, the exchange coupling between neighboring atoms is destroyed and the domain structure gets vanished. The magnetization goes to zero at

Curie temperature. A typical plot of the magnetization vs temperature for Cobalt is reproduced in the Figure 1-2.b).

1.2.3 Different classes of magnetic materials

The magnetic behavior of materials depends on the exchange interaction of localized or itinerant spin systems. One can classify magnetic behaviors into five major groups, Diamagnetism, Paramagnetism, Ferromagnetism, Antiferromagnetism. Ferrimagnetism [21].

Diamagnetic materials are composed of atoms that do not have net magnetic moments since all the electrons are paired. Under the effect of a magnetic field, a weak magnetic moment is induced in these materials with opposite direction to the external field. Thus, these materials are slightly repelled by a magnetic field and their magnetic properties are not preserved when the field is removed. Most elements in the periodic table are diamagnetic, including Copper, Silver, Carbon, Bismuth.

Paramagnetic materials are composed of atoms showing unpaired electron in the partially filled orbitals. Each atom is considered like a magnetic dipole presenting a resultant magnetic moment. Due to the thermal fluctuation, the orientation of each atom magnetic moment is random. The net magnetic moment of a paramagnetic material is zero, as one can see in Figure 1-2.a). An external magnetic field could align all atomic moments in the direction of the field and a positive magnetization is induced. Their magnetic properties are not preserved when the field is removed and the magnetization comes back to zero like in diamagnetic materials. Some paramagnetic elements: Uranium, Platinum, Sodium.

Ferromagnetism is a special case of the Paramagnetism. The main difference is that in ferromagnetic materials the contribution of the spin magnetic moment to the total magnetic dipole moment of the atom is very large. Unlike paramagnetic materials, the atomic moments in these materials exhibit very strong interaction. Accordingly, these materials consist of large number of small units called domains. In each domain, a large number of atomic moments are aligned in the same direction due to the strong parallel exchange coupling. Ferromagnetic materials exhibit a strong attraction to an external magnetic field where each domain experiences a torque. As a results some domains rotates rapidly to be aligned parallel to the direction of the field while domains whose magnetic axes are nearly in line with the external field grow in size at the cost of the neighboring domains. These materials display a large net

magnetization due to the parallel alignment of moments even if the magnetic field is removed. Ferromagnetic materials include Iron, Nickel, Cobalt, Gadolinium, and Dysprosium. We note that at the Curie temperature the material undergoes the transition from an ordered ferromagnetic material to disordered paramagnetic material.

Antiferromagnetic materials are composed of atoms displaying equal magnetic moments with opposite directions between neighboring atoms. Antiferromagnetism is a long range order of spontaneous moments with a negative exchange coupling between two neighbors. This antiparallel spontaneous configuration depends on the Néel temperature of the material. Depending on the temperature, different responses are expected when an external magnetic field is applied. At very low temperature, the antiparallel ordering of atomic magnetic moment is rigidly maintained and consequently the material does not undergo any modification in the magnetization. Meanwhile, at higher temperature some atoms become aligned with the direction of the field. Most antiferromagnets are ionic compounds (oxides FeO, CoO or elemental Cr^{+}) and ordered alloys (Fe_3Mn, CrPt).

Ferrimagnetic materials are composed of atoms presenting also opposite magnetic moments like antiferromagnetic materials, but with these moments values are unequal. Thus, a spontaneous magnetization remains. In ferrimagnetism neighboring spins are aligned antiparallel but they do not cancel and a net magnetization appears. The ordering mechanism is more like antiferromagnetic materials, but the magnetic properties resemble to these of a ferromagnet. Therefore for a temperature higher than the Curie temperature the magnetic order is lost and the material becomes paramagnetic. In addition, ferromagnetic materials present a compensation temperature at which the two opposite magnetic moments become equal inducing a zero net magnetic moment. This temperature is easily observed in transition metal rare-earth alloys. A Ferrimagnetic material show also a strong attraction to an external magnetic field and does not lose its magnetism even in the absence of this field. Normally ferrimagnetic materials involve two or more magnetic species that are chemically different. Example of some ferromagnetic material: CoTb alloy, CoFeGd alloy, Co/Pt multilayer.

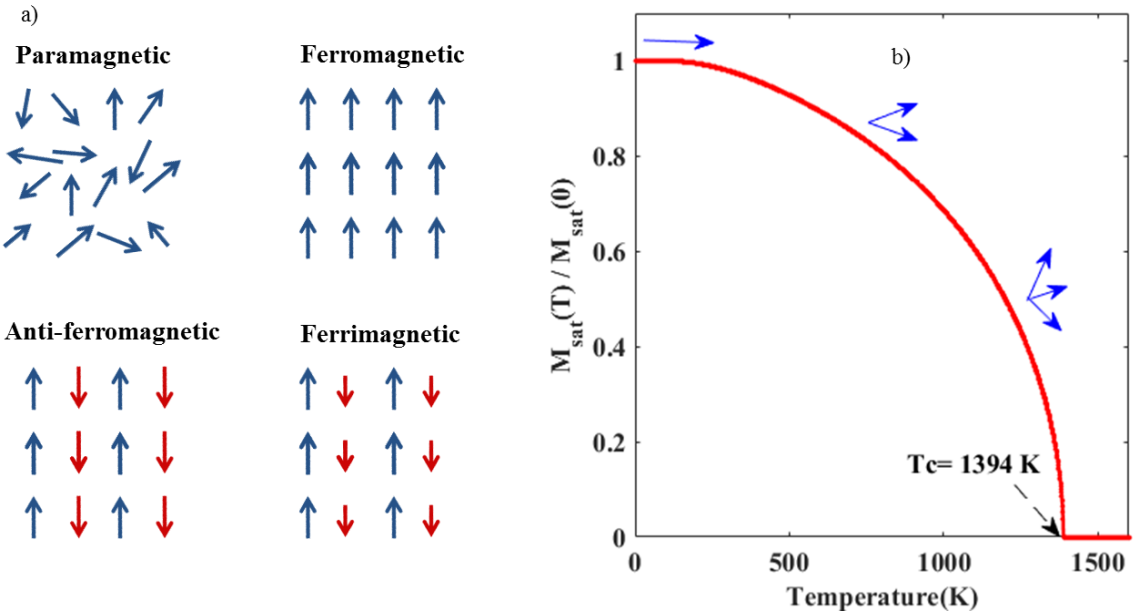

Figure 1-2: a) Different behaviors of magnetic material. b)Magnetic configuration of a Cobalt thin film in function of the heating temperature.

1.2.4 Domain wall configurations of thin magnetic films

We showed in part 1.2.2 that in order to minimize the free energy, a magnetic thin film breaks into domains showing different orientation of the magnetization. Boundaries between these domains are called magnetic domain walls. Inside this wall the magnetization rotates gradually from one direction to the other depending on the exchange and the anisotropy energies. Depending on the film thickness, there are two main types of spin structure inside the domain walls: Bloch and Neel types [25]. These two configurations are represented in the Figure 1-3. Néel walls where spins rotate in the film plane became more favorable in thin easy-plane anisotropy films. On the other hand, Bloch walls where spins rotate perpendicularly to the film plane may be energetically favored in thin perpendicular anisotropy film. We note here that other kinds of domain wall exist like the cross-tie wall which is an intermediate state between Bloch and Neel walls. In this thesis we will focus on the Bloch type wall of thin magnetic films. We will consider the case of samples that consists of alternating up and down stripe domains.

Let us consider a simple case of Bloch 180° domain wall between two opposite magnetic domain as shown in Figure 1-3.a). The wall is composed from N atoms spaced by the lattice

parameter constant "a". The angle between neighboring spins is given by θ= $\frac{\pi}{N}$. The wall width can be given as δ=Na. In the following, we will show that the number of atom inside the wall N depends on the exchange energy and the magnetic anisotropy. This means that another expression of δ could be extracted by replacing the number of lattice spacing N. The exchange energy penalty between two neighboring spins is given by [26]:

$$\Delta E_{ex} = E_{ex} - E_{ex}^{\theta=0} = -2JS^2 cos\theta + 2JS^2 \approx 2JS^2 \frac{\theta^2}{2} = JS^2 \frac{\pi^2}{N^2} \quad 1.5$$

Meanwhile, the total exchange energy penalty is the sum of the penalties between each pair of spins over N lattices spacing. Thus the total exchange energy becomes: $\Delta E_{ex}^{total} = JS^2 \frac{\pi^2}{N}$. If we take into accounts "a" as the lattice constant, then the exchange energy per unit area of the Bloch wall is given by:

$$\sigma_{BW}^{ex} = \frac{\Delta E_{ex}^{total}}{a^2} = JS^2 \frac{\pi^2}{Na^2} \quad 1.6$$

It is clear from this expression that $\sigma_{BW}^{ex} \rightarrow 0$ when N→∞. Hence it is energetically advantageous to have infinitely thick domain walls, which means that there will be no domains but just randomly oriented spin where each spin is rotated by an angle in the same direction as its neighbor. Obviously this is not the case in ferromagnetic materials where spins are oriented in the same direction along the easy axis. This will cause an increase of the anisotropy energy. Thus, the domain wall width in magnetic materials is determined by the balance between the two energies: Exchange and anisotropy.

To calculate the total anisotropy energy associated with the spins of the wall, we have to take into account the sum of the N lattice spacing[27].

$$E_a^{total} = \sum_{i=1}^{N} K_u sin^2\theta_i \approx \frac{1}{d\theta} K_u \int_0^{\pi} sin^2\theta d\theta = \frac{NK_u}{2} \quad 1.7$$

Or the anisotropy constant is given per unit volume. The total anisotropy energy per unit area of the Bloch wall is given by:

$$\sigma_a^{total} = \frac{NK_u}{2} \frac{a^3}{a^2} = \frac{NK_u a}{2} \quad 1.8$$

Bringing together the two contributions of the exchange energy and the magnetic anisotropy energy, we can define the energy associated with a unit area of the Bloch Wall as:

$$\sigma_{BW} = \sigma_a^{total} + \sigma_{BW}^{ex} = JS^2 \frac{\pi^2}{Na^2} + \frac{NK_u a}{2} \quad 1.9$$

Now in order to find the expression of the domain wall width, all what we have to do is to find the number of lattice spacing N that minimizes the energy of the wall:

$$\frac{d\sigma_{BW}}{dN} = -JS^2 \frac{\pi^2}{N^2 a^2} + \frac{K_u}{2a} \rightarrow N = \pi S \sqrt{\frac{2J}{K_u a^3}} \quad 1.10$$

We note that the exchange stiffness constant is given by $A_{ex} = \frac{nJS^2}{a}$ with n is the number of the nearest neighbor. If we consider that n=2, then the domain wall width can be defined as:

$$\delta = Na = \pi \sqrt{\frac{A_{ex}}{K_u}} \quad 1.11$$

Thus, it's clear from equation 1.11) that any modification of the uniaxial anisotropy induce changes of the domain wall width and vice versa. Higher anisotropy values yield thinner walls and films showing large exchange integral possess wider walls. Normally the domain wall width is of the order of a few nm for hard materials (high Ku) and up to 50 nm or more for soft magnetic materials[28]. The total energy per unit domain wall area is written in this form:

$$\sigma_{BW} = \pi \sqrt{A_{ex} K_u} \quad 1.12$$

We note here that the anisotropy favors two types of orientations of the magnetic moments, in plane and out of plane. In this thesis, we are interested in studying magnetic thin films presenting perpendicular anisotropy for two reasons. One reason is the symmetry of systems holding an out of plane anisotropy. This means that magnetic moments in domains can have two configurations up or down by using a special method represented later in section 2.3.1. The second reason is the potential that these configurations present for the investigation of the supper diffusive spin transport during the ultrafast demagnetization process.

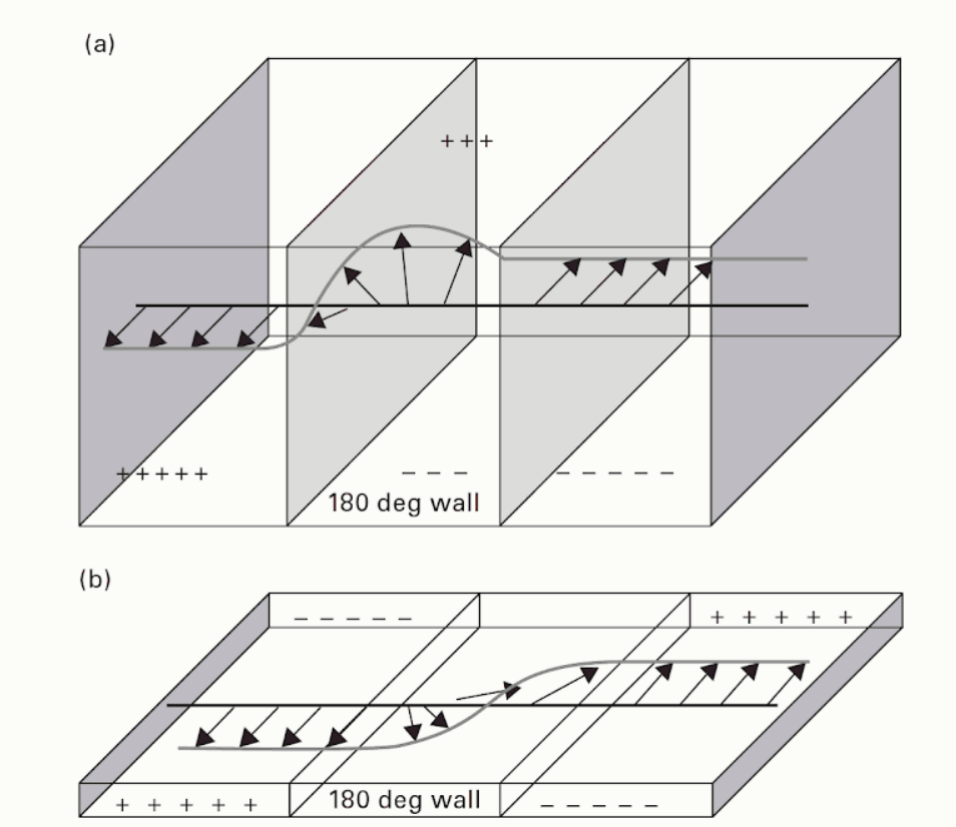

Figure 1-3: Magnetic domain wall configuration (a) Bloch wall and (b) Néel walls [29].

1.3 Mechanisms of demagnetization

1.3.1 Magnetization dynamics at different timescales

In the previous part we showed that the microscopic origin of magnetism in materials depends on their intrinsic properties. In this part we will discuss different ways of manipulating the magnetization of permanently magnetized systems (i.e. ferro and ferrimagnets). We will consider different demagnetization and switching processes that happen on different time scales. We should mention before that the macroscopic magnetization of any material is the product of two separate phenomena: spontaneous magnetization and magnetic domain alignment. Microscopically, the magnetization of ferromagnets is always at saturation; but individual magnetic domains are pointing in different direction in order to minimize the internal energy of the solid. This causes a reduction of the macroscopic magnetization. To obtain the macroscopic saturation one should apply an external field to align all these magnetic domains in one direction.

It’s very important to keep in mind that a ferromagnet (or ferrimagnet) is the result of an excess of electrons total angular momentum. Therefore, any reduction in the magnetic moment of a ferromagnetic material should be accompanied with a reduction of the angular momentum of the relevant electrons. These relevant unpaired electrons are those in the 3d band for transition metals and 4f band for rare earth elements. Another very important postulate is that the angular momentum is a conserved quantity. This means that any loss of electrons angular moments should be recovered by a transfer to another entity.

Several processes can be used in order to demagnetize a magnetic material like Thermal effects, external magnetic field effect, spin injections and Photo-induced effects. Those different processes lead to different demagnetization dynamics that happen on different timescales, as indicated in the Figure 1-4.

At the nanosecond time scale and above, the demagnetization is dominated by domain wall nucleation and propagation. One can reverse the magnetic orientation of a ferromagnet by placing it in a reversed external magnetizing field. In this case magnetic domains inside the materials rotate and point in the direction of the applied magnetic field. This mechanism is due to the domain nucleation and domain wall motion that occurs in a nanosecond timescale. This mechanism will lead to the switching of the magnetization in a microsecond timescale and the applied magnetic field should be bigger than the anisotropy field of the material. For example, when ferromagnetic materials are exposed to extreme heating conditions, atoms vibrate more rapidly and thus disturb magnetic domains and properties. We also note that domain nucleation and domain wall propagation can be subjected to thermal activation [30].

At the picosecond timescale, the demagnetization of the material is induced by a precession of magnetic moments which occurs within 10-100 ps [31].This phenomena could generate a switching of the magnetization that gets damped in a sub-ns to tens of ns timescale. This magnetic precession is induced by applying an ultrashort(~2ps) magnetic pulse perpendicular to the initial magnetization direction [32] or by injecting a spin polarized current[33].

At the femtosecond timescales, an ultrafast optical manipulation of spins in magnetic thin films and nanostructures is possible. One notes that this timescale corresponds to the exchange interaction which is responsible for the existence of a magnetic ordering. It looks like this ultrafast demagnetization is the result of reducing the spontaneous magnetization, not of any magnetic domains realignment [17]. This demagnetization is closely related to the all

optical switching of the magnetization that happen in a sub ps timescale. Despite all efforts, the main mechanism behind this ultrafast demagnetization is not very well understood. In the following parts we will discuss the ultrafast demagnetization dynamics induced by a femtosecond optical pulse.

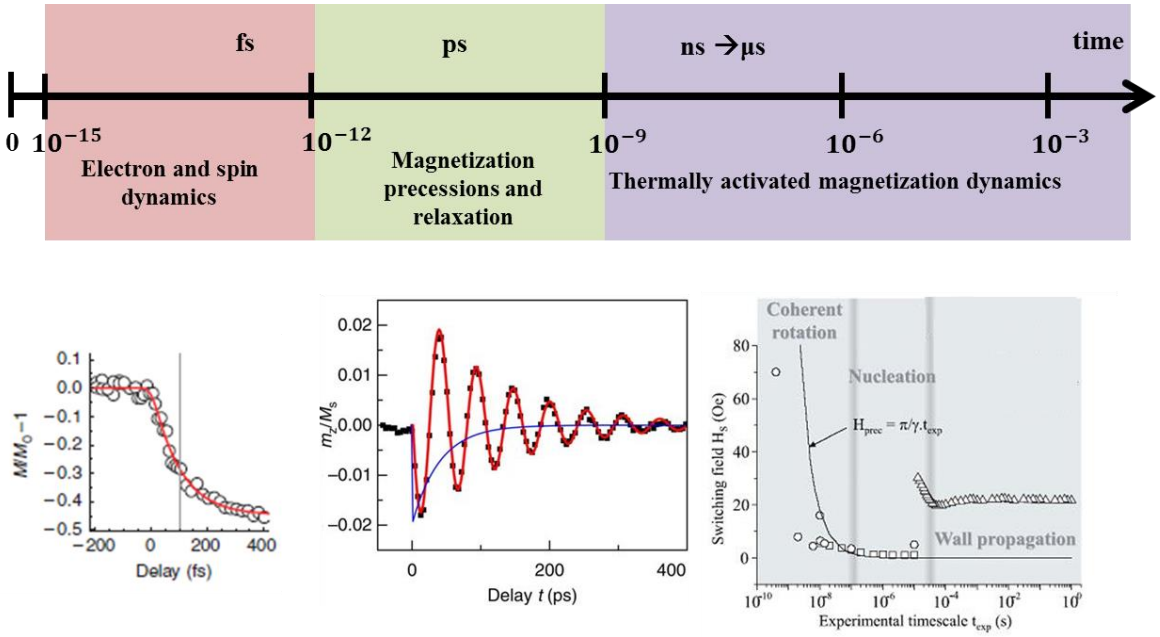

Figure 1-4 Characteristic time scales for the magnetization dynamics. Bottom figure are taken respectively from [11], [34], [35].

1.3.2 First discovery of the ultrafast demagnetization

In 1992, pump probe experiments were performed on a gadolinium samples by Vaterlaus *et al.* [36]. A nanosecond pump pulse excited the magnetic sample and after a precise time delay the probe pulse arrived to detect variation induced by the pump. The film magnetization decreased to 40 % of its initial value in 100 ps. The demagnetization timescale was then supposed to be of the order of tens of picoseconds. However, in 1996 and due to the huge developments of laser, Beaurepaire *et al.* [1] were able to pump a nickel sample with a femtosecond laser pulse. Authors found that the magnetization of the nickel film achieved its minimum value in less than 1 ps as one can see in Figure 1-5.b). This value wasn't expected

or observed in any experiment before. This observation was quickly confirmed by numerous studies showing an ultrafast quenching of the magnetic order in a variety of materials.

To explain this observation, authors proposed the phenomenological three temperature model (3TM) which considers three different degrees of freedom in a solid (the charge, lattice and spin) and their mutual interactions. When an infrared laser pulse hits a solid, it will be primarily absorbed by the electron. Then by energy equilibration the spin and the phononic system will be heated up. The three temperature model cannot provide deeper insights into microscopic processes responsible for the demagnetization since the description of magnetic phenomena in terms of thermodynamics is no longer valid. This model also leaves the angular momentum transfer undetermined. To understand phenomena in the sub-picosecond timescales two questions should be answered. How the energy flow to the spin system in such a short time? How the angular momentum is transferred out of the spin system?

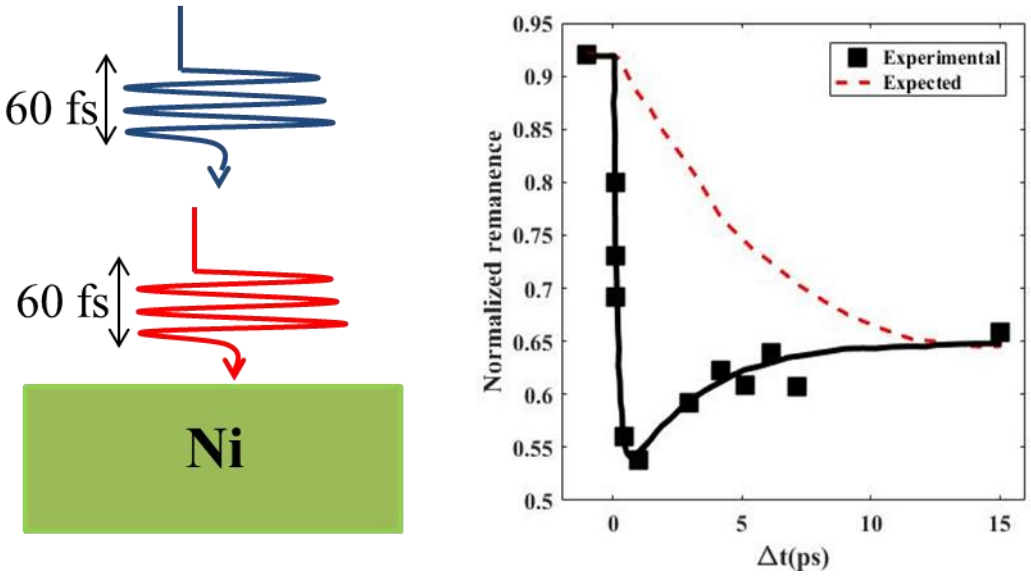

Figure 1-5 a) Sketch of the pump probe used in the Beaurepaire experiment [2]. b) The black line shows the longitudinal MOKE signal at remanence presenting an ultrafast decrease of the magnetization. The red line presents the expected behavior of the magnet.

1.3.3 The three Temperature model

The original model describing the initial perturbation of a ferromagnet by an ultrafast short pulse is the two-temperature model developed by Vaterlaus *et al*[37]. This model link the temperature of two coupled components the lattice bath and the spin bath. One of the fundamental problems of the Two-Temperature model is that a laser pulse can heat the lattice

but cannot directly couple to the spin system. The Three-Temperature model was proposed later by Beaurepaire *et al*. [1] to give a phenomenological explication of their obtained results. This model can be considered as an expansion of the Two-Temperature model where three separated reservoirs are coupled to each other. Electron reservoir, lattice reservoir and spin reservoir. The energy flows between the electron bath with temperature T_e which is thermally coupled to the lattice bath with temperature Tl, this energy rate is proportional to the temperature difference between the two baths (T_e-T_l). This is represented in the Figure 1-6.a). The constant of proportionality for this link is the coupling factor G_{el}. Similar relations exist between the electron reservoir, the lattice reservoir and the spin reservoir. The coupling term $G_{12}(T_1-T_2)$ appears twice, once in the equation for each reservoir it represents, but with an opposite sign so the model is energy conserving(excepting the input of energy by the pulse function). Below the model is reproduced with T representing the temperature, G representing the coupling constants, P representing the energy input by the pulse and C representing the specific heat. The subscripts define which bath the quantity retains to: e for the electrons, l for the lattice, s for the spins. The coupling constants relate to a pair of reservoirs and the units of each side of the equations are $W.m^{-3}$, power volume in SI:

$$C_e(T|e)\frac{dT_e}{dt} = -G_{el}(T|e - T_l) - G_{es}(T|e - T_s) + P(t) \quad 1.13$$

$$C_l(T|l)\frac{dT_l}{dt} = -G_{el}(T|l - T_e) - G_{sl}(T|l - T_s) \quad 1.14$$

$$C_s(T|s)\frac{dT_s}{dt} = -G_{sl}(T|s - T_l) - G_{es}(T|s - T_e) \quad 1.15$$

The heat capacities are modeled with a constant heat capacity where the lattice specific heat was taken as a constant [38], the electronic specific heat was taken as a linear function of electron temperature and the spin heat was taken to be the remainder of the total heat capacity:

$$C = Cl + Ce + Cs \quad 1.16$$

$$C=4 \times 10^6\ J.m^{-3}.K^{-1}$$

$$Cl=2.2 \times 10^6\ J.m^{-3}.K^{-1}$$

$$Ce= (6 \times 10^3)*T_e\ J.m^{-3}.K^{-1}$$

$$C_s=C-C_l-C_e$$

$$=4 \times 10^{6} - (6 \times 10^{3}).T_e \ J.m^{-3}.K^{-1}.$$

The degree of thermal conductivity between the reservoirs is represented by the coupling constants. Those coupling represent the probability of an interaction between reservoirs multiplied by the energy transferred. To align the model with experimental observations those coupling constants are chosen:

$$Gel = 8 * 10^{17} \ W.m^{-3}.K^{-1}$$

$$Ges = 6 * 10^{17} \ W.m^{-3}.K^{-1}$$

$$Gsl = 3 * 10^{16} \ W.m^{-3}.K^{-1}$$

These values are used to reproduce the three temperature model developed by Beaurepaire *et al* and represented in the Figure 1-6. Another developed model that gives a more accurate figure for the three temperature model exist: like Non thermal Electron Model [39] and Microscopic Three Temperature Mode [40]. Describing these models is beyond the main objective of this thesis.

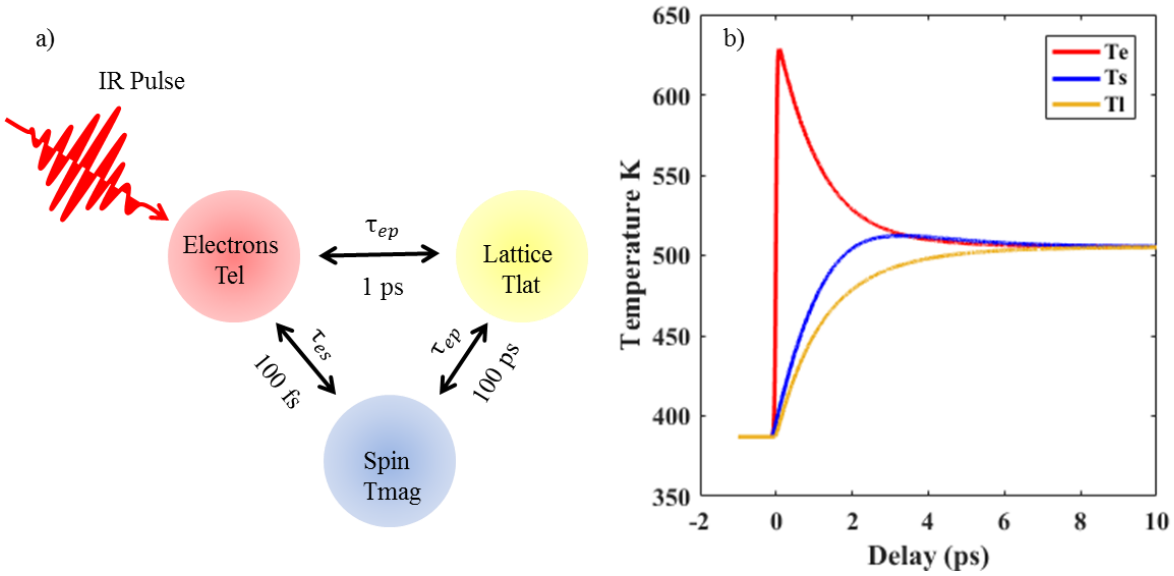

Figure 1-6 Diagram of the three temperature model showing the time constants for interaction of the reservoirs. b) A reproduction of BeaurePaire *et al*. model using the three temperature model equation. The values of coupling constants and heat capacities are reported in the text.

1.4 Microscopic models trying to explain the origin of femtosecond demagnetization

Many studies and many models were proposed to explain ultrafast demagnetization dynamics. Some theory assumed the existence of an ultrafast channel for the dissipation of spin angular momentum since any reduction in the magnetization is due to a reduction in the magnetic moment of a ferromagnet. This must implicate a reduction of the angular momentum of the relevant electrons. Thus, any loss of electrons angular momentum should be compensated by phonon, magnon or impurities. Another model considers an ultrafast transport of the laser excited spin polarized electrons with high mobility. In this thesis the two most broadly discussed models: Elliot-Yafet scattering and superdiffusive spin transports are presented.

1.4.1 Elliot-Yafet spin Flip Interactions

The electron phonon scattering spin flip based on the Elliott-Yafet scattering was first explicitly addressed by Koopmans *et al*. in 2005 [3]. This model is described by a probability a_{EY} that an electron flips its spin on emission or absorption of a photon. Then a dissipation of angular momentum from the spin system to the lattice system occurs as one can see in Figure 1-7. Two scenarios would be expected in this electron phonon spin flip. In the first case, angular momentum is transferred directly from the spin system to the phonon system. Another way is a conversion of the orbital angular momentum to the spin without any angular momentum transfer to the lattice. XMCD measurements performed by Stamm *et al*. [41] showed that a rapid momentum transfer between orbital and spin moment doesn't exist. This leaves the dissipation of angular momentum to the lattice as a possible channel. In 2010 another model was proposed by Koopmans *et al*, called microscopic three temperature model (M3TM) [39]. This model is based on ab initio calculation of the Elliot Yafet spin flip probabilities a_{sf}. A material with a high spin flip energy will transfer energy from the electron to the spin system more rapidly. This model is able to reproduce a similar behavior of Cobalt and Nickel demagnetization for different laser fluences.

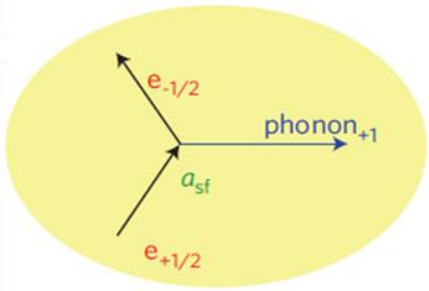

Figure 1-7 Sketch of the Elliott–Yafet spin-flip scattering mechanism. Figure taken from Ref [39].

Meanwhile, Essert and Schneider [42] showed in their calculations that this Elliot-Yafet spin flip type is not large enough to explain the experimentally observed dynamics and that a dynamical change of the band structure should exist in this femtosecond timescale. Also Illg *et al* [43] showed that the electron-phonon spin flip and the reduction of the exchange splitting value cannot explain the demagnetization rate observed experimentally. They suggest that a possible explanation of this ultrafast behavior should include an electron magnon spin flip. These contradictions in calculations doubt that this Elliot-Yafet spin flip scattering phenomena cannot explain alone the demagnetization rate observed experimentally and that another process should be taken into account.

Recently Shokeen *et al* [5] highlighted that the demagnetization phenomena is material dependent. They propose that spin flips in nickel samples driven by the spin orbit coupling are the main contributors of the demagnetization process, which is not the case for the Cobalt sample. Also Leckron *et al* [44]showed that if a precession of a spin around the exchange energy could happen before the electron phonon scattering, spin flip transitions can explain the demagnetization rate. Otherwise for high precession period the demagnetization dynamics are slower and less pronounced.

1.4.2 Super diffusive transport

Another point of view considers that demagnetization comes from a relative change in the propagation of spin minority and spin majority in the probed area. This model is based on a spin dependent transport of hot electrons. So non equilibrium electrons, initially excited by the laser pulse are spin polarized and they will travel with very high velocity (~ 1nm/fs) out of the magnetized region as one can see in Figure 1-8. In ferromagnetic materials the majority and the minority spin channels occupy different bands. Thus, the transport proprieties are spin

dependent and it is easier for majority electrons to leave an area irradiated by a laser pulse. This generates a femtosecond spin currents. The demagnetization phenomenon is proposed to be driven by a magnetization flux away from the ferromagnetic film. Super diffusive transport mechanism was proposed by Oppeneer as a driving mechanism of the ultrafast demagnetization then subsequently experimental studies and theoretical models present direct proofs for the validity of this mechanism[4]. As a follow up of this work, Battiato *et al* [45] compared the different demagnetization dynamics of a ferromagnetic/nonmagnetic metallic layered junction such as Ni/Al with a ferromagnetic/nonmagnetic insulator junction such as Ni/MgO. According to their calculations, they showed that the average magnetization of the ferromagnet in contact with the insulating layer is conserved; in a way that the region close to the ferromagnet surface excited by the laser pulse is demagnetized due to a migration of the spin majority while the area in contact with the insulating layer show an increase of the magnetization due to the accumulation of spin majority carriers. Therefore, they suggested that the demagnetization is larger when the ferromagnetic layer in contact with a metallic layer.

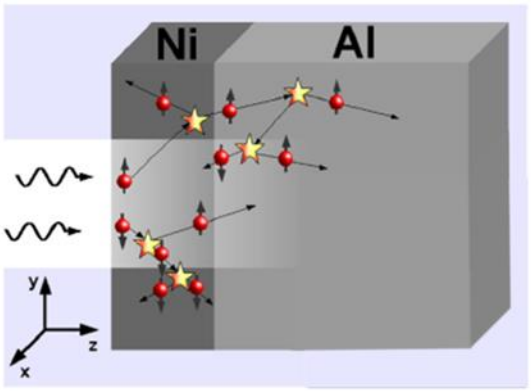

Figure 1-8 A sketch of the super diffusive phenomena caused the laser excitation. Majority and minority spin carriers show different mean free paths and also a cascade of electrons is generated after an inelastic scattering [4].

Additionally, Rudolf *et al* [46] investigated the ultrafast spin dynamics induced by an ultrashort laser excitation of Ni/Ru/Fe trilayers, where the magnetization of the Ni and Fe layers can be parallel or antiparallel (see Figure 1-9.a). They found that when the Fe and Ni layers are antiferromagnetically coupled, then the magnetization of both elements decreases (see Figure 1-9 c)). One the other hand, if the two layers are coupled ferromagnetically, then the magnetization of Ni layer excited by the laser pulse decreases while the magnetization of

the Fe is enhanced by the demagnetization of Ni(see Figure 1-9 b)). This comparison between the reduced and enhanced magnetization of the two systems on the femtosecond timescale demonstrated that optically induced demagnetization generates superdiffusive spin current between the Fe and Ni layers. From this point of view, the superdiffsuive transport model obtained a great success to predict the contribution of non-local majority and minority electrons.

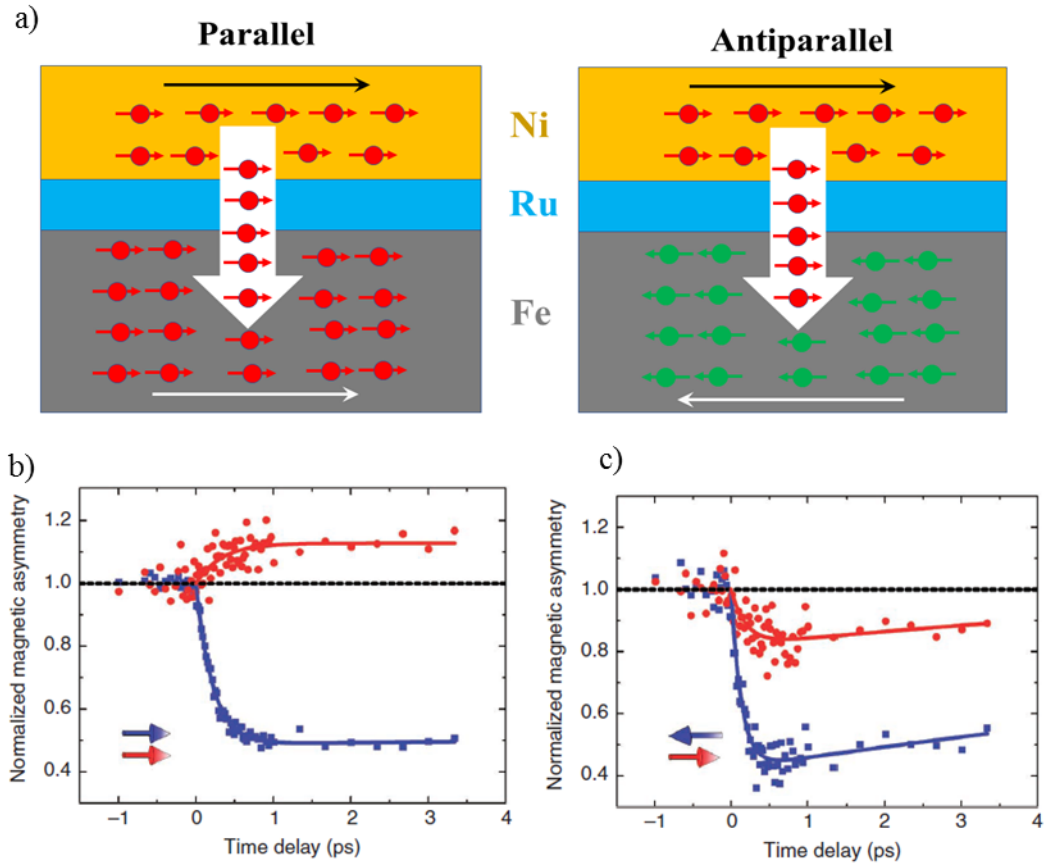

Figure 1-9 a): illustrate schematically the relative magnetization of the Ni and Fe layers (thin black and white arrows), the majority spin alignment in the layers (red and green circles) and the flow of the spin current (large vertical white arrow). b) and c) Time-resolved magnetization of the Fe and Ni layers for respectively parallel and antiparallel magnetization alignment [46].

However, Schellekens *et al* [47] investigated the contribution of the spin transport to the ultrafast demagnetization of the Ni film. By comparing front-pump with back-pump measurements of Ni film on an insulating sapphire substrate, they pointed out that spin transport is not the main contributor to the demagnetization process. Even by adding a conductive buffer layer, the demagnetization rate has not been significantly increased, which contradicts the prediction of the superdiffusive spin transport model. They conclude that spin

currents isn't the dominant effect of laser induced magnetization dynamics in simple ferromagnetic Ni films. A recent experiment manifested that demagnetization phenomena is material dependent. In his same article Shokeen *et al* [5] show that the major part of demagnetization is caused by spin currents in the early time for Cobalt sample.

1.4.3 Other microscopic models

We note here that neither one of the two models discussed above has convinced the entire community. Current experiments suggest that potentially both of them occur simultaneously.

Other explications of this ultrafast phenomenon were also proposed. Several authors suggested that this drop in the magnetization is due to the direct interaction with the laser photons where their an angular momentum $<L_{ph}>$ is transferred to the electron spin <Se>[48],[49]. Other authors believe in an angular momentum flow from the electron spin <Se>to the electron orbit $<L_e>$ due to the spin orbit coupling during the electron-electron scattering in a very fast process [50]. Another explanation is that due to the electron-magnon scattering [51], an angular momentum is transferred from $<S_e>$ to $<L_e>$ via this scattering mechanism and subsequently $<L_e>$ is quenched by the crystal field. Others postulate that due to Einsten-de Haas effect (phonon-phonon interaction) the reduction of the electron spin <Se> results in a net rotation of the irradiated area of the sample[52]. Finally, electron defect and electron interface scattering in magnetic samples could participate in the femtosecond demagnetization process [53].

2 Sample growth and characterization

2.1 Sample growth by Magnetron Sputtering

Thin films can be fabricated by different deposition process and fabrication techniques; it is possible to classify these techniques in two branches: Physical Process and Chemical Process. In this part, we will introduce the magnetron sputtering technique which is considered as a physical process. The “Sputtering gun” was the first sputtering source and it was developed in 1970 by Peter J. Clarke[54]. In 1974 J.S Chapin improves this source by designing a planar magnetron[55]. Since then, this technology became one of the most common ways to achieve accurate and reliable deposition on an atomic level. This technique aims to grow thin films with thicknesses ranging from nanometers up to micrometers.

Magnetron sputtering is based on energetic plasma which ions will bombard a target made in the material we want to grow. Due to the strong collision target atoms are ejected. The substrate that we want to grow the layer on is facing the target. Ejected atoms travel some distance until they reach the substrate and start to form a film. At the molecular level, as the number of collision increase, atoms begin to bind to each other forming a tightly bound atomic layer on the substrate. Depending on the sputtering time and on the chosen source (target), one can produce a precise layered thin film. Even though the basic process behind this technique seems easy to understand, actual mechanisms are quite complex. In Figure 2-1 a schematic of this technique is presented. As one can see that the magnetron sputtering technique consists of many cathodes and one anode enclosed in a vacuum chamber. The cathode holds the target material at a negative potential. The substrate can be considered as the anode. Now at very low pressure (8 mbar), Argon atoms are introduced into the vacuum chamber. A DC voltage applied between the target and the substrate ionizes these atoms and creates plasma in the chamber. These charged argon ions are accelerated to the cathode target and collide with it, ejecting atoms that will travel and settle on the substrate. Electrons released during the ionization process moves spirally along magnetic field lines near the target. We note that the cathode is placed above a permanent ring magnet. Due to the strong magnetic field imposed by the permanent magnet, the plasma is confined to an area near the target while electrons travel for longer distance increasing the probability of further Argon atom ionization.

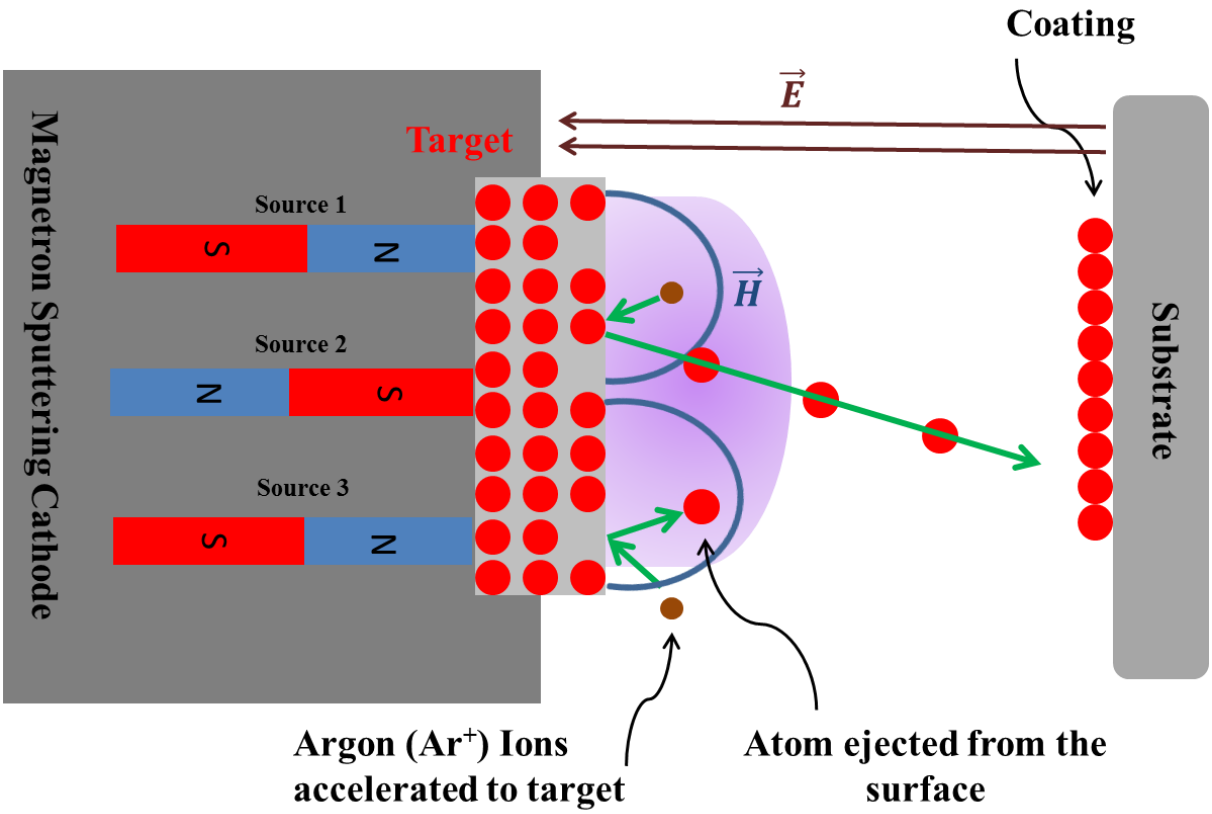

Figure 2-1: Schematic of a magnetron sputtering process in a sputter down configuration

One notes that in order to fabricate thin films of good quality, many parameters have to be taken into account like the penetration depth and the deposition pressure etc. These parameters depend on the mass and energy of ions, and also on the composition and structure of the target. The microstructure is also affected by the sputtered atom kinetic energy and momentum. In order to avoid any lose in the energy of the sputtered atom due to collisions with the background gas, it is desirable to operate coating at very low pressure. At this pressure the mean free path of atoms is comparable to or larger than the target-substrate distance.

Another important parameter of the magnetron sputtering process is the deposition rate. In order to determine the thickness of the fabricated thin film one should measure this rate given in Å/s. This deposition rate is affected by many parameters like gas sputtering pressure, gas mixture, gas purity, power in the target and the strength of the magnetic field in the cathode. There are many different way to measure or calculate this rate but in our setup we use piezoelectric crystal quartz which measures a mass change per crystal area by detecting the

change of the deposition frequency. This frequency changes due to the growing mass of a material on the surface of the quartz crystal during the deposition.

In Figure 2-2 the setup of the LCPMR magnetron sputtering used during this thesis is represented. As one can see it is formed from two different main chambers, SAS (load lock) where one can change the sample and the main chamber where the coating process takes place. Once the desirable value of vacuum (< 10^{-8} mbar) is obtained, the substrate can be transferred to the sample holder by the transfer cane. The sample holder and the crystal quartz are mounted on a metal bar connected to two manipulators that allow it to move transversally and rotationally. There are four targets installed in the main chamber meaning that four different metals can be deposited during one process of sample preparation. This allows us to fabricate multilayers and alloys samples. All sputter guns are water cooled to avoid overheating of the target, the underlying magnets and the other front parts of the sputter gun by the plasma discharge. Another larger system (8 sources) has been designed and realized in our group during my PhD.

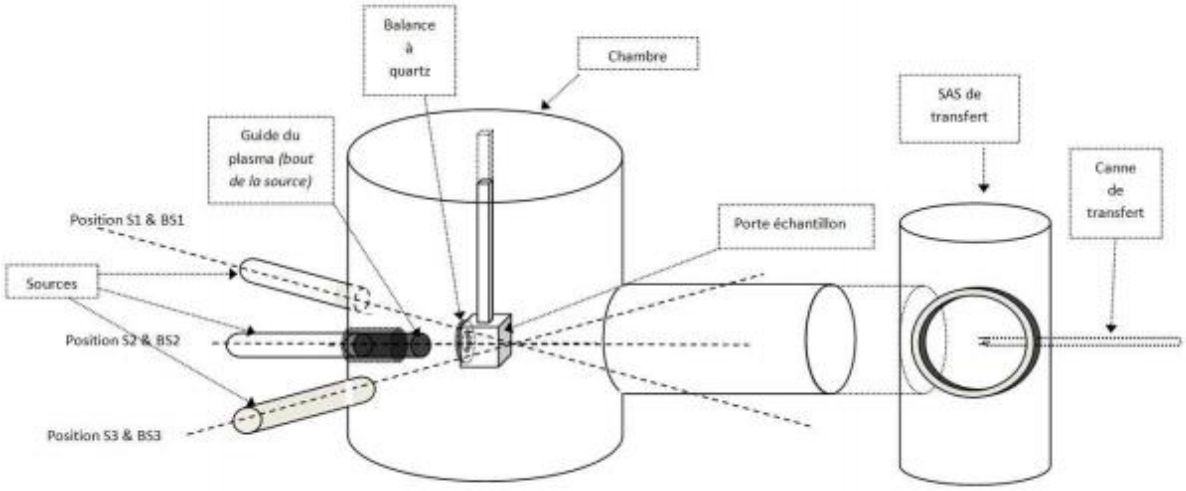

Figure 2-2: Sketch of the Magnetron sputtering machine at the LCPMR

In our studies, fabricated samples are restricted to thin magnetic films. Normally sputtered samples prepared during this thesis are composed by a substrate, buffer layer, magnetic layer and the capping layer. For the substrate two types were used depending on the experiment, a square silicon wafer slice or silicon nitride window. The buffer layer reduces the substrate defects (stress, adhesion) and accommodates the lattice parameter between the substrate and

the subsequent magnetic layer. The choice of the buffer layer depends on the materials we want to grow. In this thesis, Aluminum, Platinum, Palladium and Chrome thin buffer layers were deposited on the substrate with a thickness that can go from 3 to 10 nm. Three magnetic systems were investigated for different purposes: Monolayers, Multilayers and alloys. The capping prevents the oxidation of the magnetic thin film. It is important to note that different behaviors of the ultrafast demagnetization are observed between alloys and multilayers system.

2.2 Sample characterization

In order to characterize the magnetic properties of the film we grow we used a Magneto Optical Kerr Effect. The SQUID-VSM technique was employed to measure magnetization hysteresis curves as function of temperature. Magnetic Force Microscopy was used to characterize the magnetic domains configuration.

2.2.1 Magneto Optical Kerr Effect

Magneto Optical effects arise from the optical anisotropy caused by the magnetization within materials. In fact the optical anisotropy alters the state of light when interacting with magnetic materials. In 1846 Faraday found that the polarization of light is rotated through a transparent material subjected to a magnetic field [56]. Thirty one years later, the Magneto-Optical Kerr Effect was discovered by John Kerr in 1887 [57]. This effect is analogous to Faraday Effect and describes the changes of light polarization and intensity when it is reflected by a magnetic surface. The MOKE is highly sensitive to the magnetization within a depth of 10 to 20 nm in most metals [58]. This makes it particularly useful for the study of magnetism since the effect is proportional to the magnetization. It is a relatively simple technique to implement and provide hysteresis loops or magnetic domain images (in microscopy experiment).

Before describing the MOKE set up used during this thesis, I will introduce the principles of MOKE.

Depending on the orientation of the magnetization to the incident light, three main configurations exist as one can see in the Figure 2-3. In polar geometry, the magnetization M is perpendicular to the sample surface. In the case of longitudinal geometry M is parallel to

both the plane of incidence and the sample surface. However, in the transverse configuration M lies parallel to the sample surface but perpendicular to the plane of incidence.

For linearly polarized light the electric field is confined to a single plane along the direction of propagation. The two orthogonal linear polarization states that are most important for reflection and transmission experiments are referred to as p and s polarization. If the electric field is polarized in the plane of incidence, it is referred to as p-polarized light. Conversely, if the electric field is polarized perpendicular to the plane of incidence, then it is referred to as *s*-polarized light.

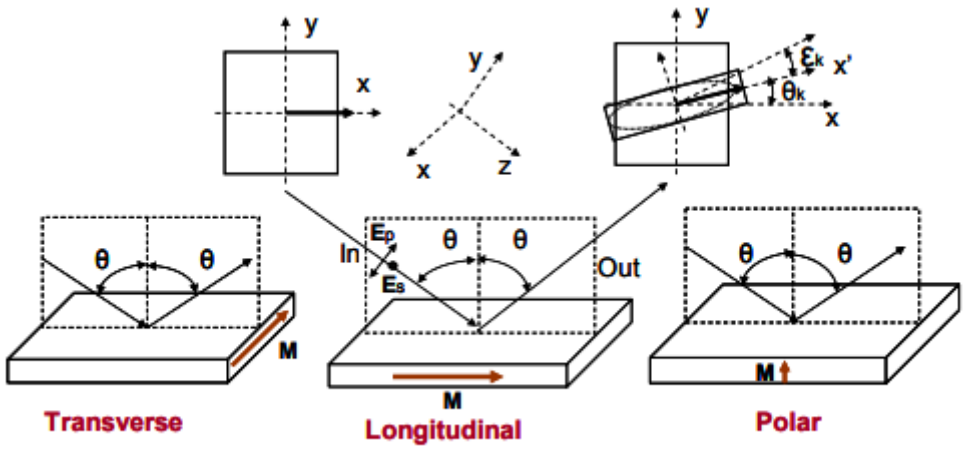

Figure 2-3: Three different geometries for the MOKE experiments and a schematic of the polarization states of the light, before and after the reflection on a magnetic film. [59]

In the longitudinal and polar Kerr effects, due to the Lorentz force the reflected light is not polarized in the same plane of the incident light. The electric field of the incident light excites the electrons to oscillate along the incident polarization direction. Due to Lorentz force, an additional small component (qv*B) perpendicular to the normal component and to the magnetization is induced. For example let us consider an s-polarized light reflected from a magnetic sample. The magnetization does not affect the light s-component but a small p-component appears in the reflected light. Therefore the polarization becomes elliptical and the major axis undergoes a rotation around its initial incident polarization plane [60], as one can see in figure 2-4. These effects are Kerr rotation and Kerr ellipticity. However, there is no change in the polarization state in the transversal MOKE because the incident light is not normal to the reflection surface. In this case, the reflectivity R is measured instead of

measuring the polarization. Analytical expressions are beyond the scope of this thesis. For more details, Magneto Optical Kerr Effects are described macroscopically in [61] and microscopically in [62].

The MOKE set up implemented at LCPMR can exploit magnetic samples in the longitudinal and polar geometries. This setup is used widely and introduced in the Figure 2-5 below. The laser radiation goes through a polarizer where a highly polarized light is produced with an extinction coefficient of 10^{-5}. The light is then focused on the sample surface. The sample is placed between the 2 poles of the electromagnet and is mounted on a rotatable sample holder which allows a 360° for the sample rotation. The electromagnet is attached to a bipolar power supply and generates a magnetic field up to 0.7 T. The reflected light is then modulated by a photo elastic modulator before passing through the analyzer and finally being detected by a photodetector. The acquisition system is fully computer controlled. In Figure 2-5 b) and c) we show the hysteresis loop of Co film (20 nm) measured in the polar mode and longitudinal mode. The square loop showing a low coercive field of the longitudinal measurement indicates the in plane magnetic anisotropy of the film. The polar measurements show that it is hard to magnetize this sample out of plane.

All samples fabricated during this thesis by the magnetron sputtering show an out of plane or in plane magnetization. These samples were characterized by doing longitudinal and polar MOKE measurements.

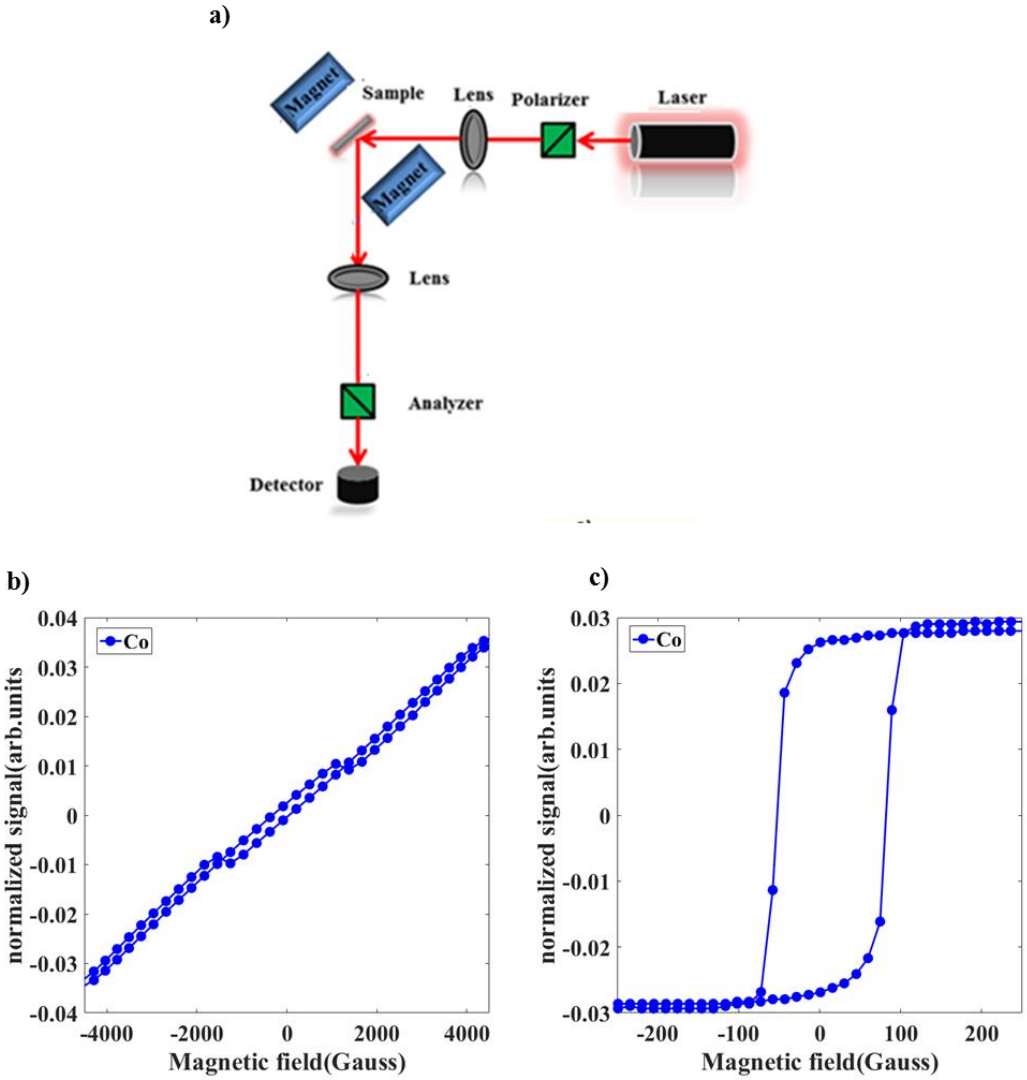

Figure 2-5: a) Schematic of the MOKE setup. The light pulses generated by the laser source are linearly polarized by a polarizer with a high extinction ratio. The light is then reflected by the sample which is magnetized by an electromagnet. b) and c) Hysteresis loop of a Co film measured respectively in polar mode and longitudinal mode.

2.2.2 SQUID-VSM

SQUID-VSM is the abbreviation for Superconducting Quantum Interference Device and Vibrating Sample Magnetometer. The SQUID technique probes the whole volume of the sample contrary to the MOKE technique which is only sensitive to the surface as we discussed before. The SQUID was invented in 1964 by scientist at the Ford Research Labs[63] after the fabrication of the first Josephson junction (thin insulating barrier) at Bell Labs in 1963 [64]. It consists of two superconductors separated by two Josephson junctions connected in parallel mode as one can see in Figure 2-6. However, the electrical current

density through a weak electric contact between two superconductors depends on the phase difference $\Delta\varphi$ of the two superconducting wave functions [65]. Any additional magnetic flux through the ring induces a variation of $\Delta\varphi$. Or the flux is quantized [65] and this phase changing can be converted into an electrical voltage. This ring is coupled to a superconducting flux transformer comprising a pick up loop and an input coil tightly coupled to the SQUID.

In a conventional SQUID magnetometer, the magnetic sample is moved through the superconducting pick up loop in the form of a first gradiometer (see Figure 2-6). This will cause changes in the magnetic flux through the pickup loop and therefore a screening current flow in the loop. This same current flow in the device input coil and generates a magnetic field that changes the magnetic flux in the SQUID. The SQUID responds by generating a proportional output voltage that can be recorded as a function of the sample position. The potential difference is fed into a feedback circuit known as a flux locked loop. An additional field via the flux locked loop coil is applied to return the SQUID to its initial state. The magnetization of the sample is determined by measuring the current in the flux locked loop. However since a full profile has to be recorded at each value of H, measurements over an extended range of H tend to take a long time.

In Vibrating Sample Magnetometer, the sample is placed inside a uniform magnetic field that undergoes a sinusoidal vibration through the use of piezoelectric materials. A time dependent magnetic flux is produced through a nearby pick up coils. Due to Faraday's law of induction, the magnetic flux converted into a voltage in the coils is measured. This method is relatively faster than the SQUID measurement but it does not have the same sensitivity. Simon Foner at Lincoln Laboratory MIT invented the first VSM in 1955 and reported it in 1959[66].

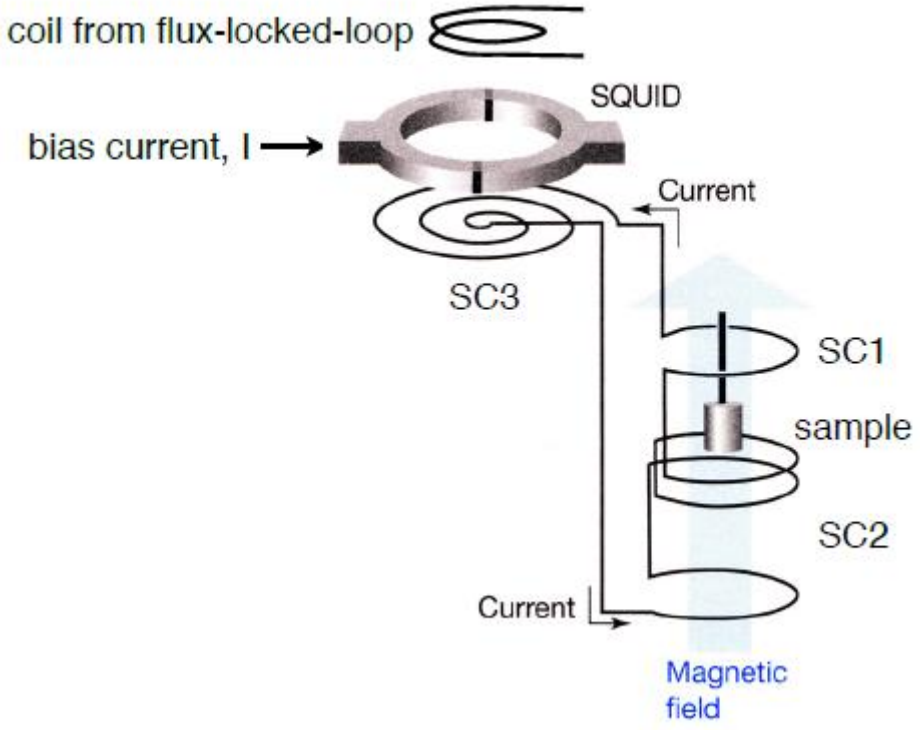

Figure 2-6: Schematic representation of the SQUID [67].

The SQUID-VSM technique combines the high sensitivity of the SQUID with the high speed measurements of a conventional VSM. First, one should fix the sample at the point where the slope of the flux profile is maximum. Then the SQUID output as a function of temperature is recorded while the sample vibrate around his mean position at a low frequency. Measurements over an extended range of T and H can be completed in a relatively short period since the full flux profile does not have to be recorded.

In this thesis we are interested in the variation of the uniaxial anisotropy constant in function of the heating temperature. For this reason SQUID VSM hysteresis loop at different temperature were recorded for three different magnetic samples (CoTb,CoPd,CoPt). Both in plane and out of plane configurations were recorded. Hysteresis loop of CoTb and Co/Pt are represented in Figure 2-9.b) and Figure 2-11.b) respectively.

By following the variation of the in plane hysteresis loop obtained as function of the heating temperature, one can trace the value of the uniaxial anisotropy. The magnetic anisotropy can be determined if the anisotropy field H_A and the saturation magnetization M_S are known. The effective anisotropy K_{eff} can also then be directly obtained with:

$$K_{eff} = \frac{1}{2}\mu_0 M_s H_A \qquad 2.1$$

And the uniaxial perpendicular anisotropy constant Ku as:

$$K_u = \frac{1}{2}\mu_0 M_s H_A + \frac{1}{2}\mu_0 M_s^2 \qquad 2.2$$

2.2.3 Magnetic Force Microscopy

Magnetic Force Microscopy (MFM) is just a special operation mode of the Atomic Force Microscope (AFM). MFM was developed shortly after the invention of the AFM by Martin & Wickramasinghe in 1987 [68] and became a popular technique that offers high imaging resolution of the magnetic field spatial distribution without the need for special sample preparation conditions. In this technique a sharp magnetic tip scans a magnetic sample. Tip-sample interactions are detected and used to reconstruct the magnetic structure of the sample surface. MFM can be used to image various magnetic domains for different materials like thin films, nanoparticles, nanowires, permalloy disks and recording media. Domain unification due to an external magnetic field can also be studied for samples presenting big domain walls. This method presents a lot of advantages but the spatial resolution is still lower than 20 nm and so inconvenient for following domain walls. In this thesis, we employed the MFM technique to get information on the magnetic domain of our samples as one can see in Figure 2-8.

2.3 CoTb based alloys and Co/Pt multilayers

2.3.1 Magnetic properties of transition Metal-Rare Earth alloys $Co_{88}Tb_{12}$

The magnetization of the TM-RE alloy results from the magnetization of the rare earth and the transition metal sub lattices. In 3d transition metals, a strong coupling is observed because the 3d electrons occupy an outer shell and thus participate in the band structure. Also their itinerant character is at the origin of the coupling between atomic moments. In Cobalt, the 3d band is nearly full and the Fermi wavelength λ_F (electrons jump from one site to other without changing his spin configuration) is much larger than interatomic distance causing a ferromagnetic coupling of electrons moments. In Rare Earth metals, the magnetic interactions between neighboring spin are much weaker than in 3d elements. Actually, in rare earth elements the magnetism is due to their 4f electrons. In fact, the 4f electrons strongly localized on an inner shell do not participate in interatomic bonds and so no direct interaction may occur. The exchange interactions between 4f electrons is considered as long range and mediated by 5d, 6s electrons. Due to strong spin orbit coupling in rare earth atoms, the spin

and orbital moments may be large and are maintained parallel to each other. Terbium is among the heavy rare earth with 8 electrons in the f shell and possessing a big orbital value L=3. In a CoTb alloy the magnetic moment is due to the exchange coupling between the itinerant moment of the Co sub lattice and the localized 4f electrons of the Tb sub lattice. The two sub lattices are coupled antiferromagnetically. Thus, alloys are considered ferrimagnetic as the sub lattice magnetizations have different magnitudes.
One can see it in this way, the exchange constant between two Co moments is positive and between two Tb is positive but that between a Co and a Tb moment is negative. The coupling between the two different sub lattice of Co and Tb happens on indirect way via the conducting 5s electron of the Tb atoms. This model from [69] is schematically represented in Figure 2-7. Due to this interaction between the two sub lattices the total magnetization of the CoTb alloy is obtained then from [69] by making the difference of the two contributions in this way:

$$| M_{CoTb}(x_{vol},T)| = |M_{Co}(T)*(1-x_{vol}) - M_{Tb}(T)*x_{vol}| \qquad 2.3$$

with x_{vol} is the Tb volume composition and T is the temperature. One can see it clearly from the expression above that the magnetization of the sample is affected by a temperature changes. This is due to the Tb sub lattice which is very sensitive to temperature due to the low Curie temperature, 273 K, of Tb[70]. Consequently a lot of studies were focused on the change of the CoTb magnetization as a function of the sample composition and temperature. The value of the magnetization M for five different sample compositions from [69] is represented in the Figure 2-7-b).

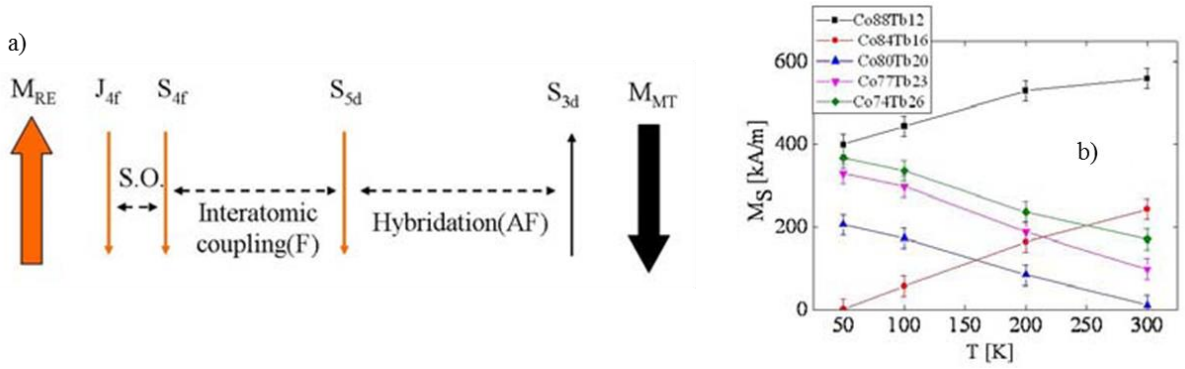

Figure 2-7: a) Schematic representation of the indirect exchange coupling between a RE and a TM in the case of an alloy. b) Magnetization vs temperature for different sample compositions from [69].

It is important to note also that if the x_{vol} of the Tb is higher than 21 %, the net magentization is parallel to the Tb sublattice at the room temperature and the sample is called a Tb-rich composition. Otherwise, the net magnetization is parallel to Co sublattice and the film is called a Co rich composition.

In this thesis we investigated the ultrafast demagnetization dynamics of the $Co_{88}Tb_{12}$ alloy. The sample consists of 50 nm thin $Co_{88}Tb_{12}$ film deposited on Si_3N_4 square membrane of 50 μm in size with 10 nm of tantalum as a buffer layer. Our sample exhibit a perpendicular out of plane anisotropy and is prepared to present a network of stripe domain with opposite direction of the magnetization, as one can see in the MFM image below Figure 2-8. The origin of this perpendicular magnetic anisotropy in these samples is still an open question, despite all studies that discuss the ordering effects in these amorphous RE-TM alloys.

The magnetic domain structure of aligned stripe domains, comes from an in plane demagnetization procedure of the sample using a decreasing oscillating magnetic field as described in[71]. We can deduct from these images that the magnetic periodicity is around 210 nm, indicating a magnetic domain width of 105 nm.

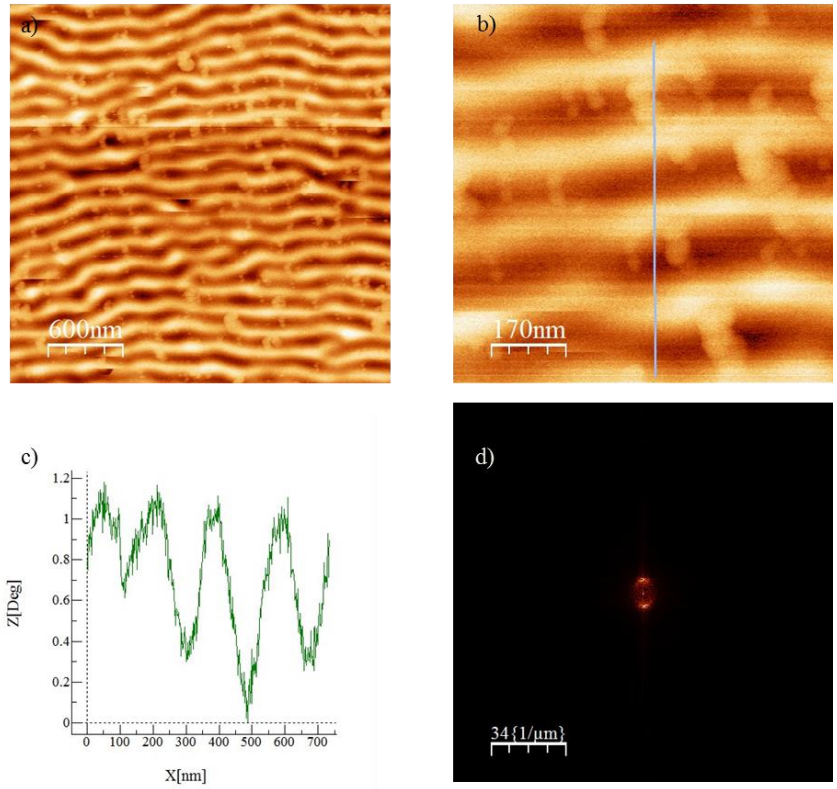

Figure 2-8: MFM image of magnetic stripe domains patterns in Co88Tb12 samples in (a) and zoom in (b). In (c) MFM profiles along the cross line of the gray color in (b) is obtained. (d) FFT of the images to estimate the magnetic domain size.

Information about the magnetic configuration and sample parameters are obtained from the polar MOKE measurement, already described in section 2.2.1. The out of plane MOKE measurement is presented in the Figure 2-9.a). The uniaxial anisotropy constant and the magnetization at saturation are determined by applying an out of plane and in plane SQUID-VSM experiments. Results of the SQUID-VSM measurement of the CoTb sample at the room temperature are presented in the Figure 2-9.b). To calculate the uniaxial anisotropy constant using the equation (2.2), one has to find the anisotropy field and magnetization of the sample. The magnetization at saturation is extracted from Figure 2-9 and Ms was found to be around 640 kA/m(see section 4.4.6). The anisotropy field where the magnetization saturate at maximum value is also extracted from the Figure 2-9.b), $H_A=1.5*10^4$ Oe. The uniaxial anisotropy constant is easily calculated and $K_u=737$ KJ/m^{-3}.

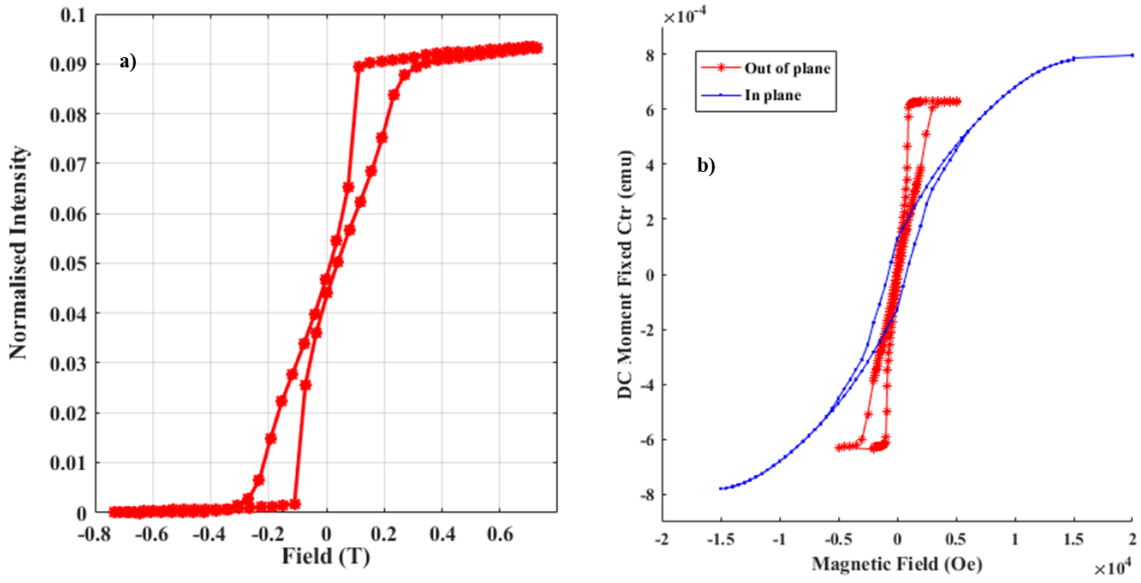

Figure 2-9: a) Hysteresis loops obtained from polar MOKE measurement of the $Co_{88}Tb_{12}$ sample. b) SQUID-VSM hysteresis loops in two configurations, out of plane with the red graph and in plane with the blue dot points.

2.3.2 Magnetic properties of the Co/Pt multilayer system

In the previous part we explained the main reason behind the ferromagnetic order in the Cobalt materials. Here, we will be more interested by the magnetism in 5d transition metals and especially at Platinum. Actually, all studies made Platinum clusters showed that it is paramagnetic in the bulk states at all temperatures [72]. Some studies have indicated that Platinum atoms become magnetic when grouped together in nanoclusters [73]. It was shown also by Tang *et al* that Pt nanowire are ferromagnetic at room temperature, in contrast to their bulk form[74]. In the case of ultrathin films depending on the sample composition and the substrate, a ferromagnetic order can be induced in the Pt films [75], [76]. In 1988 Carcia *et al*.[77] reported a Co/Pt multilayer system that exhibits a perpendicular magnetic anisotropy. Depending on the growth behavior, the Co/Pt systems could display equivalently large lattice mismatches of 9 %. In multilayers systems, the out of plane configuration is due to many factors like roughness, interface alloys, patchiness and etc [74].

In this thesis we followed the demagnetization dynamics of the ferromagnetic Co/Pt sample with the composition $(Co_{0.6nm}/Pt_{0.8nm})*20$ multilayer grown on Si_3N_4 membrane, 3nm Ta as a buffer layer and 3nm of thin Al cap layer. Our sample presents also a network of stripe domain with opposite directions of the magnetization, as one can see in the MFM image

below. We can deduct from these images that the magnetic periodicity is around 170 nm, indicating a magnetic domain width of 85 nm.

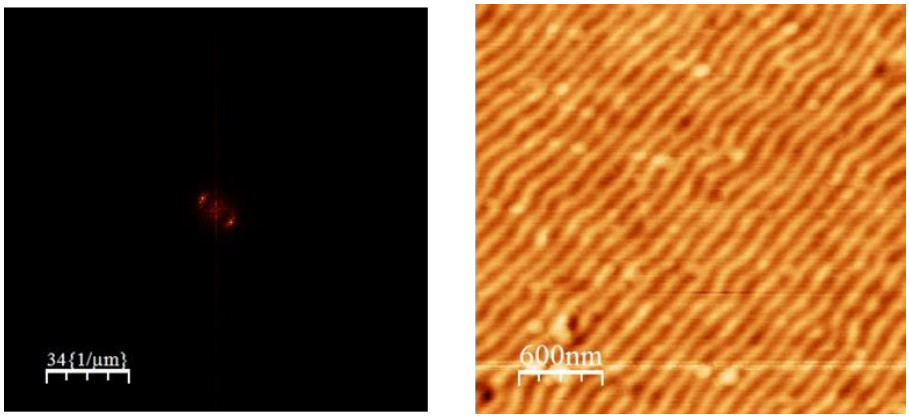

Figure 2-10: MFM image of Co/Pt sample with a FFT of the image.

The out of plane hysteresis loop of the Co/Pt is measured using polar MOKE and presented in Figure 2-11. The uniaxial anisotropy constant is calculated after finding the magnetization at saturation and the coercive field from the in plane SQUID-VSM hysteresis given in Figure 2-11.b). The uniaxial anisotropy constant of the Co/Pt sample is calculated from equation (2.2) and Ku=7500 kJ/m^{-3}.

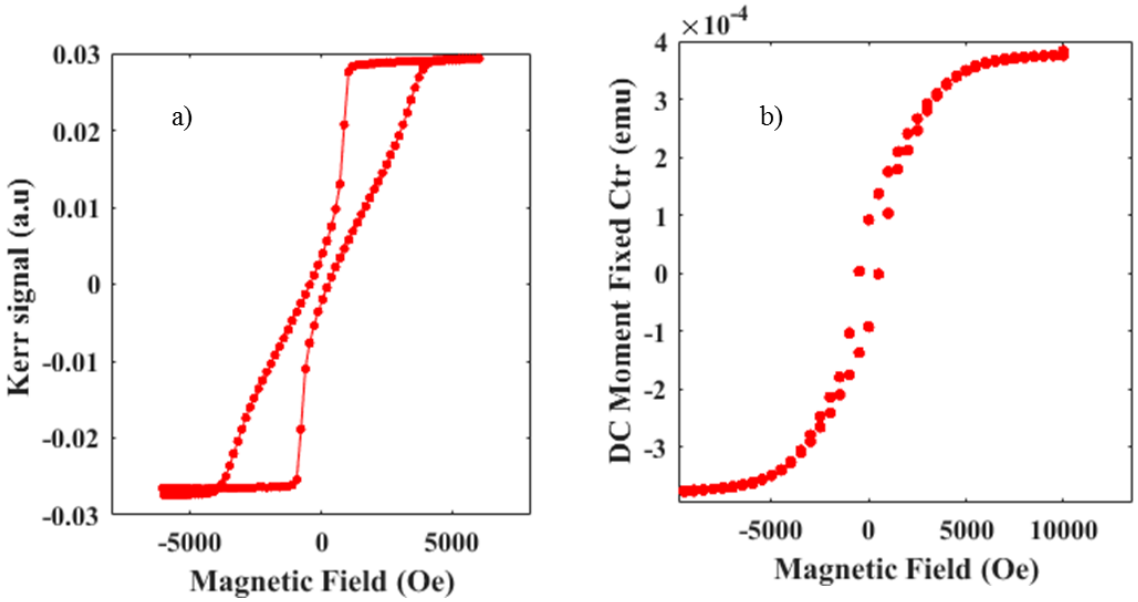

Figure 2-11: a)Polar MOKE measurement of the Co/Pt sample. b) In plane hysteresis loop obtained by SQUID-VSM measurement.

3 Resonant soft X-ray scattering on magnetic stripe domains

3.1 Introduction

In this chapter we discuss the fundamentals of resonant soft X-ray techniques used in this thesis.

In the first part, we will introduce the advantages that X-rays offer to investigate materials and we will compare the properties of different X-ray sources. This will lead us to the conclusion that the X-rays generated by FEL sources are indispensable for the investigation of ultrafast dynamics. In the second part, we will focus on the interaction of X-rays with matter in general and then more precisely with magnetic materials. We review first the absorption of X-rays by materials by showing the relation between the refractive index and the X-ray cross section. This relation will be used latter to make a direct connection between the scattering amplitudes and the absorption index which depends on the incident wavelength. We discuss then the dependency of X-ray absorption on the incident polarization and how this effect can be employed to study magnetic materials. We show later how the linear absorption coefficient is directly linked to the scattering term which depends linearly on the magnetic moment. After that, we discuss in detail the case of small angle scattering form samples presenting a network of stripe domains. For the case of magnetic materials we show that the detected intensity is proportional to the square of the magnetization.

Finally, as a direct application of these techniques we will present the results obtained from our prof of principle experiment demonstrating the feasibility of multicolor imaging.

3.2 Why X-rays for studying magnetism

3.2.1 Key Advantage of X-ray for the investigation of materials

Generally, depending on the technique used to probe materials, different aspects are emphasized. This holds true also for the investigation of magnetic materials with optical and X-ray based probe methods. Optical techniques like MOKE and Faraday are powerful techniques which are broadly applied to study magnetic materials. Although quantitative magnetization measurements are generally difficult to obtain, they are very sensitive for probing of magnetization changes. Furthermore, they exhibit several short comings which X-ray based techniques overcome. In optical techniques, it is not possible to obtain nanometer spatial resolution due to the wavelength which is on the order of hundreds of nanometers; element specific studies are generally not possible due to the employed optical probing of valence band electrons; and buried layers are generally difficult, or not at all, accessible.

In contrast, X-ray based techniques offer nanometer spatial resolution, element specificity, high penetration depth and resonant probing provides a high sensitivity for probing of magnetic properties, which is often quantitative.. These advantages follow from two main properties of X-rays. Nanometer spatial resolution and high penetration depth follow from the short X-ray wavelength which is in the range of fractions to a few tens of nm. One distinguishes generally between hard ($\lambda < 0.4$ nm) and soft (0.4 nm $< \lambda <$ 40 nm) X-rays. Chemical selectivity results from the interaction of X-rays with core electrons, since these have element specific binding energies. By tuning the X rays to an element's absorption edge we can therefore study selectively the properties of this element within a complex compound material.

3.2.2 X-ray sources: A short overview from Tubes to Free Electron Lasers

The first paper on X-rays was written in 1895 by Wilhelm Röentgen, Professor at Würzburg University [78]. He discovered that when an electric current is passing from an induction coil through a partially evacuated glass tube, an invisible light is emitted. Even though the tube was covered by black paper and the room was completely dark, the screen covered by a fluorescent material was illuminated by those rays [79]. He called this new type of radiation

“X-ray”, because in mathematics ‘X’ is used to indicate an unknown quantity. Today we understand that the electrons accelerated by the high voltage will lose kinetic energy when colliding with the target and this energy is emitted as X-rays (so-called Bremsstrahlung). Note that most of the kinetic energy of the electrons striking the target is converted into heat and less than 1% is transformed into X-rays. The advent of commercial X-ray tubes created the field of radiography and such tubes are today broadly used in a variety of applications ranging, for example, from medicine to material inspection.

For scientific experiments, X-ray tubes present two crucial short comings: The radiation is emitted in all directions, which cannot be collected and redirected to a common focal point; and the radiation is only intense at a single (few) specific wavelength which makes them ineffective for spectroscopy application.

In 1947 the electromagnetic radiation resulting from the acceleration of electrons in a circular accelerator was observed for the first time in the 70 MeV synchrotron at the General Electric Research Laboratory in New York by Frank Elder, Anatole Gurewitsch, Robert Langmuir and Herb Pollock[80]. Decades later, this synchrotron radiation became widely recognized as an important research tool for physicists, chemists, and biologist leading finally to the construction of electron storage rings all over the world. Synchrotron radiation is characterized by a very high intensity, a high degree of collimation, a continuous energy spectrum and a very high degree of adjustable polarization.

The time resolution in synchrotrons is given by the electron bunch length, which is usually between 50 and 100 ps (FWHM)[81]. Despite all the progress and upgrade in synchrotron sources to make shorter pulses, sub-ps time resolution is not accessible without losing dramatically in intensity. To apply X-ray techniques in order to investigate femtosecond dynamics other sources are needed. Since about 2005,High-order Harmonic Generation provides with significant intensity femtosecond short pulses covering the low energy part of the soft X-ray range (< ~100 eV, also referred to as XUV) [82]. Although this energy range covers the core electron absorption edges of a variety of elements, the significant overlap with valence band electron excitations complicates experiments in this spectral range [83]. This is overcome by X-ray Free Electron Laser light source. This new sources offer femtosecond short, very bright X-ray pulses with tunable photon energy as illustrated in Figure 3-1 [58]. The first XFEL user facilities became operational in 2005 (Flash, soft X-rays), in 2009 followed the first XFEL emitting in the hard X-ray photon energy range (LCLS).

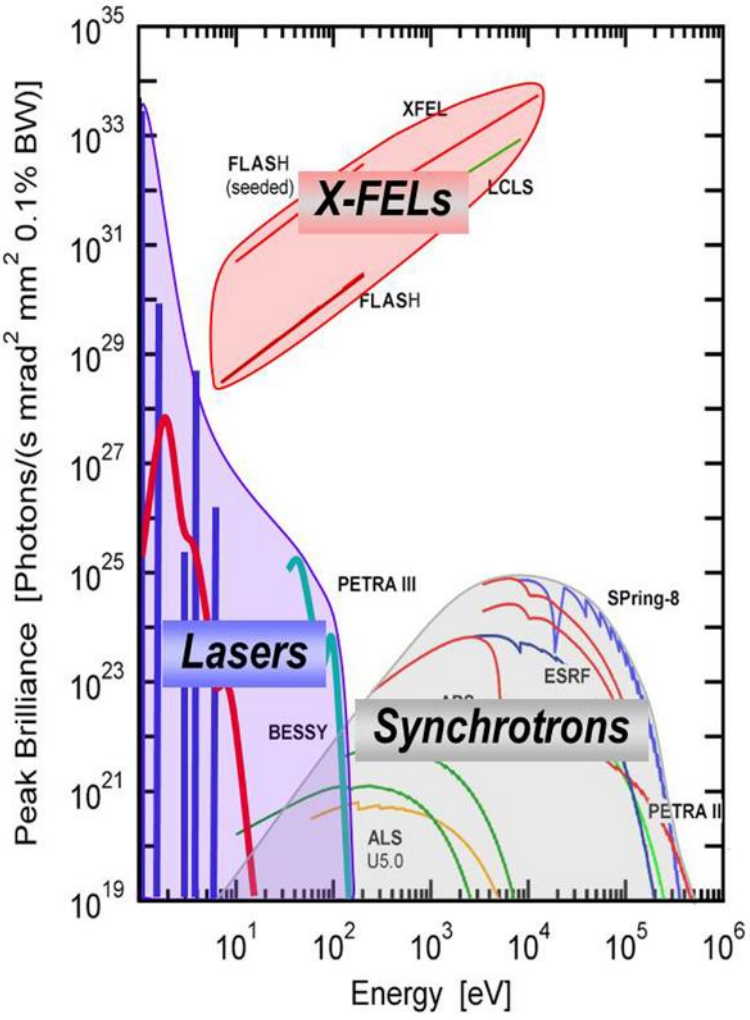

Figure 3-1: Peak Brilliance of different photon sources form [58]

3.2.3 Properties of the XUV-FELs FLASH and FERMI

Free Electron Laser is another radiation source where highly accelerated free electrons fly almost at the speed of light within a vacuum tube through a magnetic structure. X-ray Free Electron Lasers consists of a linear accelerator and a subsequent long periodic arrangement of magnets with alternating poles across the beam path. Initially all electrons are distributed evenly and they emit incoherent spontaneous radiation. Through the interaction of this radiation with the oscillating electrons, the electron bunch is structured in micro bunches that are separated by a distance equal to one radiation wavelength. This is illustrated in Figure 3-2 [58].Depending on the relative phase between the radiation and an electron's oscillation; it experiences either a deceleration or acceleration. It results in a modulation of the electron's velocity which eventually leads to a concentration of the electrons in micro- bunch. The

distance between these micro bunches is given by the wavelength, hence, each microbunch has a length which is short with respect to the wavelength. Thus, in each slice, electrons radiate like a 'point-like macro particle' and the radiation of an X-ray FEL is therefore transversely coherent (see Figure 3-2). The intensity of the emitted radiation is this high pulse intensity builds up exponentially during the amplification process within the long undulator. This is the so-called Self-Amplified Spontaneous Emission (SASE) mechanism; the electrons produce spontaneous radiation in the first part of a long undulator which is then amplified in the main part of the undulator (see Figure 3-2). This process is characterized by fluctuations in wavelength and FEL pulse energy.

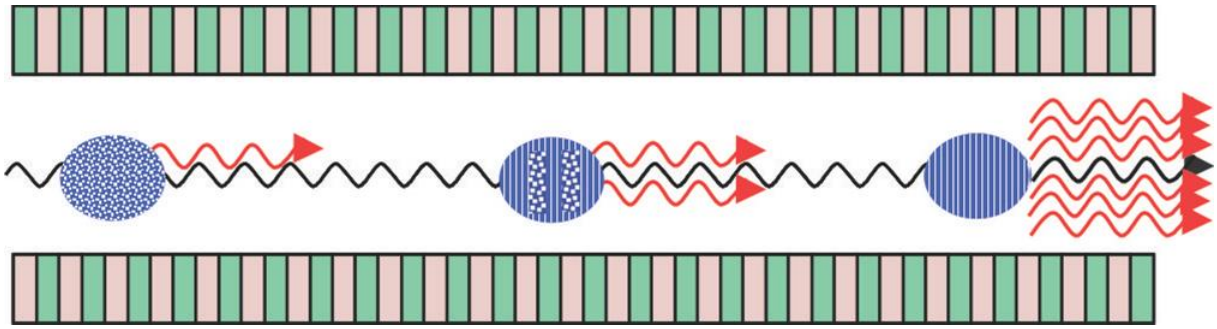

Figure 3-2: Scheme of the Self Amplified Spontaneous Emission mode from [31]. An electron bunch is injected in a long undulator. Interaction of the electrons with the emitted photon field (red) leads to spatial structuring of the electron bunch, which consists at saturation of slices of electron bunches, which are separated by one wavelength from each other.

This issue can be overcome by the so-called seeding of the FEL. In this mode, an external laser pulse is used to introduce within a first undulator (modulator) a well-defined sub-structuring of the electron bunch. In the subsequent undulators (radiators), the radiation corresponding to a higher harmonic of this sub-structure is amplified. Such seeded FELs exhibit a higher stability in intensity and also in photon energy, as well as a higher degree of longitudinal coherence [85]. Thus, the pulse photon energy is better defined and the intensity is less fluctuating.

In the following, we describe in more details the two XFELs at which the experiments discussed in this manuscript were realized:

FLASH is the world's first FEL designed and constructed to emit in the extended ultraviolet and soft X-ray photon energy range. It is located at DESY in Hamburg, Germany. It started user operation in summer 2005. This XUV-FEL is based on the SASE operation mode

described above. One of FLASH particularities is that the electron beam is accelerated and compressed in superconducting linear accelerator cavities. This allows using a long bunch train where up to 800 pulses per train can be obtained with an overall 10 Hz repetition rate of the accelerator. Today, the linear accelerator feeds two undulator lines, FLASH1 and FLASH2, providing XUV-FEL radiation for two experiments 'at the same time'. At Flash 1, the wavelength of the X-rays is tuned by adapting the electron energy of the accelerator, since the undulator gap is fixed. At FLASH2, it is possible to vary the gap size of the undulator magnets and the radiation wavelength can be changed in a wide range without changing the electron energy, i.e., without influencing the operation of FLASH1. The beam parameters of the two facilities are listed in the Table 1. Note that the light pulses delivered by FLASH1 and FALSH2 are linearly polarized Table 1.

Beam Parameters	FLASH-1	FLASH-2
Photon Energy(ev)	25-300	15-300
Average Pulse energy [μJ]	10-500	10-1000
Pulse duration[fs]	30-200	10-200
Peak Power[GW]	1-5	1-5
FEL mode	SASE	SASE
Spectral width [%] (FWHM)	0.7-2	0.5-2
Polarization	Linear Horizontal	Linear Horizontal

Table 1 Parameters of the photons generated at FLASH facilities[86]

During this thesis, I have participated in the implementation of a new device at FLASH1 to control the polarization of the generated radiation. This equipment uses a four metallic mirror based polarizer that converts the initially linear polarization to an elliptical polarization. In the spectral range of (35 eV to 80 eV), this device assures a high degree of circularly polarized radiation (up to 90%) while maintaining high total transmission values exceeding 30%. This device enables the realization of experiments at FLASH, which require circular polarization. For example, magnetic imaging by Fourier transform holography (FTH) [87]relies on the X-ray magnetic circular dichroism. To demonstrate the performance of this device, we realized such a FTH imaging experiment. More details are given in appendix and can be found in [88].

FERMI (Free Electron Laser Radiation for Multidisciplinary Investigations) is a seeded XUV-FEL source based on high gain harmonic generation [89]. It is the world's first seeded

XUV-FEL user facility and it covers the same energy range as FLASH. Another crucial difference that distinguishes FERMI from FLASH is that FERMI uses a variable gap Apple II-type undulator. This gives users the ability to control the polarization of the emitted light. There are two FEL undulators lines at FERMI, FEL-1 and FEL-2, optimized to deliver radiation in the ranges of 4-20 nm and 20-100 nm, respectively. The characteristic of pulses generated from FEL1 and FEL2 are listed in Table 2.

Also, it is important to note that a multi-color mode was recently developed at FERMI [90]. This opens up the field of two color experiments like FEL-pump – FEL-probe and multicolor FEL probing.The first demonstrated two-color scheme [90] uses two seed pulses with distinct wavelength $\boldsymbol{\lambda}_{\text{Seed1,2}}$ can be used to introduce different micro-bunchings in the modulator undulator. Note that these pulses are time delayed with respect to each other, hence, they modulate the energy in distinct regions of the electron bunch, each region exhibiting an electron density modulation that carries all harmonics of the corresponding seed wavelength $\boldsymbol{\lambda}_{\text{Seed1,2}}$. The resonance condition of the final radiator undulator determines the photon of the XUV radiation emitted by these sections of the electron bunch. To obtain two different energies, the radiator is separated into two subsections, one resonant at $\boldsymbol{\lambda}_{\text{FEL\_1}}= \boldsymbol{\lambda}_{\text{Seed1}}/\text{m}$ and the other at $\boldsymbol{\lambda}_{\text{FEL\_2}}= \boldsymbol{\lambda}_{\text{Seed2}}/\text{n}$. It is important to note here that a temporal separation between the two FEL pulses is required to avoid overlap between the two optical seed pulses.

Photon Beam Parameters	FEL-1	FEL-2
Photon Energy(ev)	12.4-65	65-310
Average Pulse energy [μJ]	25-200	10-100
Pulse duration[fs]	50-100	20-60
Peak Power[GW]	0.4-3	0.4-2.5
FEL mode	SEEDED	SEEDED
FEL Bandwidth Fluctuations[mev][rms]	3-5	3-40
Polarization	Linear Horizontal Linear Vertical Circular Left Circular Right	Linear Horizontal Linear Vertical Circular Left Circular Right

Table 2 Parameters of the pulses generated at the XUV-FEL FERMI [91]

3.3 Fundamentals of soft X-ray magneto-optics

3.3.1 X-ray absorption and optical constants

When X-rays interact with matter, primarily, the electric field of the electromagnetic radiation interacts with the electrons of the atom. X-rays will be either scattered by electrons or absorbed and excite electrons. The absorption of X-rays by matter can be understood in terms of a plane electromagnetic wave E(z,t) passing through a material, which is represented by the complex refractive index n(E)=1-δ(E)+iβ(E). The real part δ(E) represents the refraction (dispersion) and the imaginary part β(E) represents the absorption of the electromagnetic wave in the material. It's important to note here that δ and β are both small compared to unity in the x-ray region [92].

An electromagnetic plane wave propagating as a plane wave through the material along the z direction can be written as[92]:

$$E(z,t) = E_0 e^{-i(wt-n(E)kz)} \tag{3.1}$$

E_0 is the modulus of the electric field, k=2π/$\boldsymbol{\lambda}$ is the wave vector and w is the frequency of the oscillating field. k=w/c is the wavevector. Using the complex refractive index n(E), this relation can be rewritten as:

$$E(z,t) = E_0 e^{iw\left(\frac{z}{c}-t\right)} \underbrace{e^{-ik\delta(E)z}}_{\text{Phase shift}} \underbrace{e^{-k\beta(E)z}}_{\text{Absorption}} \tag{3.2}$$

The first term represents the propagation in vacuum while the second term induces a phase shift (δ(E)) and the third term describes the absorption (β(E)).

The absorption of X-ray and materials is macroscopically described by the Beer-Lambert law[93]. This law states that the intensity of X-rays passing through a material is exponentially attenuated with the material thickness. The transmitted intensity is thus given by [20]:

$$I(E,Z,t) = I_0 e^{-\mu_x(E,Z)t} \tag{3.3}$$

with t the thickness of the material, I_0 the incident intensity and μ_x(E, Z) the linear absorption coefficient, which depends on the materials elements (Z) and the incident photon energy E. The experimentally accessible absorption coefficient μ_x(E) can be linked to the absorption cross section:

$$\beta(E) = \frac{\mu_x(E)\lambda}{4\pi} = \frac{\rho_a \lambda}{4\pi}\sigma^{abs}(E) \qquad 3.4$$

3.3.2 X-ray Magnetic Circular Dichroism

It has been observed [94] that the x-ray absorption coefficient of a ferromagnetic material depends for circularly polarized X-rays on the relative orientation of magnetization and X-ray propagation direction. It manifests itself as a difference the absorption coefficient when the vector of the circular polarization is parallel or antiparallel to the incident X-ray wave vector. This effect forms the basis for magnetic contrast in x-ray scattering and imaging technique as we will show later. To take the XMCD effect into account in the macroscopic description the complex refractive index is written as:

$$n \pm (E) \;=\; 1 - (\delta(E) \;\pm \Delta\,\delta(E)) + i(\beta(E) \pm \Delta\beta(E)) \qquad 3.5$$

The ± of $n_{\pm}$(E) refers to parallel vs antiparallel orientation of the circular polarization and the magnetization direction. The additional contributions in the real and imaginary part of $n_{\pm}$ are the magneto optical constants $\Delta\delta$(E) and $\Delta\beta$(E) which represent the magnetic contribution and which introduce a variation in absorption and phase. We note here that in absorption experiment we must expect the contribution of $\Delta\beta$ alone. However, in scattering measurement, both $\Delta\delta$ and $\Delta\beta$ play significant role which allows the realization of our measurement i.e: The Fourier Transform Holography. We will use this form of $n_{\pm}$(E) later in section 4.4.5.

A key property of XMCD is its elemental specificity, which originates from the implication of a core electron in the absorption process. Since the binding energy of core electrons is element specific, this enables the characterization of different components forming complex magnetic materials. Furthermore, XMCD provides quantitative information about the orbital angular momentum and spin components of the magnetization, which can be quantified via so-called sum rules [24]. These properties render XMCD a powerful technique for the characterization of magnetic materials. The main aspect behind the physical origin of XMCD

is that for circularly polarized light, the electric field propagates along a circular helical path and thus the angular momentum of right handed photon(L_{ph}^{+}+ħ) is opposite to that of the left handed photon(L_{ph}^{-}-ħ). Due to angular momentum conservation during the absorption process, the photon's angular momentum is entirely transferred to the excited electron. . In 3d transition metals, the excitation of photoelectrons from the $2p_{3/2}$ and $2p_{1/2}$ states into the 3d states correspond to the L_3 and L_2 absorption edges, which differ in their respective spin-orbit coupling (L_3=l+s and L_2=l-s). During the 2p → 3d dipole transition the spin of the excited photoelectron is conserved. One can show that at the L_2 edge left circularly polarized light excites 25% spin up and 75% spin down electrons[24]. Right circular polarized light does the opposite. At the L_3 edge, 62.5% spin up electrons and 37.5% spin down electrons are excited by left circular polarized light. Right circular polarized light does the opposite.

Once the core level electron is excited, the unoccupied exchange split d bands serves as a spin detector for the excited spin polarized electrons. The 3d valence band of transition metals exhibits an imbalance between spin up and spin down unoccupied states. Therefore, the absorption probability which depends directly on the number of available empty states is different for spin up and spin down electrons. In consequence, the XMCD effect at the $L_{2,3}$ edge of Iron is bigger than the one of Cobalt and Nickel [24].

In other words, the absorption spectra measured at the $L_{2,3}$ edges of a transition metal depends on the helicity of the circular polarized X-rays and thus differ from each other. The dichroism signal is given by the difference between these two spectra.

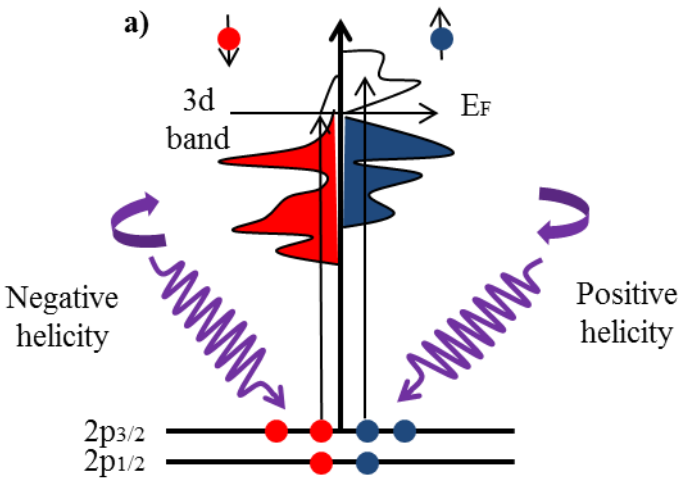

Figure 3-3: Excitation of spin polarized electron from the 3p band into the d-bands using X-rays with opposite helicity.

Since the material's magnetization defines the quantization axis of the internal spin detector, we now understand that the XMCD effect is proportional to the relative alignment of the polarization vector and the magnetization direction. The maximum effect is measured when the incident light polarization vector is parallel or antiparallel to the sample magnetization direction. For a perpendicular orientation of magnetization and light polarization vector, the spectra recorded for opposite polarization (right and left) will be identical, i.e., the XMCD signal will be zero.

The transmitted XMCD intensity is given by[20]:

$$I^{\pm} \propto P_{\circ} . < m > cos\theta \qquad 3.6$$

where P_o is the degree of circular polarization, <m> the expectation value of the magnetization carried by the 3d band, and θ is the angle between the direction of the incident X-rays and the magnetization direction. Equation (3.6) underlines that reversing the helicity is equivalent to reversing the sample magnetization.

In the following, we will discuss the XMCD spectra of Iron, Cobalt and Nickel at the $M_{2,3}$ edges ($3p_{1/2}$ and $3p_{3/2}$ → 3d). We note here that the 3p edge is analogue to the 2p edge and an XMCD effect must be present for circularly polarized resonant X-rays. However, due to the smaller spin-orbit splitting of the 3p shell, the two resonances edges M2 and M3 overlap which reduces the amplitude of the XMCD effect. In addition, experiments are complicated

by the significantly stronger absorption of the valence electron in this spectral range. Meanwhile, deriving optical constants in the XUV photon energy range is very important for any quantitative analysis of the magnetization dynamics as well for simulation of experiments. To this purpose, we measured the X-ray absorption spectra of the three elements (Fe, Co and Ni) at the M edge using right and left circularly polarized light. The magnetic layer has a thickness of 15 nm and was deposited by sputtering on a 20 nm thick Si_3N_4 membrane. These measurements, in which I participated, were carried in transmission geometry at the UE112 end station of BESSYII synchrotron.

The $M_{2,3}$-edge absorption spectra of magnetically saturated Fe, Co and Ni films were recorded for two opposite circular helicities. Employing equation (3.3) and equation (3.4), we can directly deduce the absorption coefficient $\beta(E)$ which is represented in figure-3-4. As discussed above, the M_2 and M_3 absorption edges are almost overlapping for Iron (52.7 eV), Cobalt (59 eV) and Nickel (66.5 eV and 68 eV). Due to this, one can't apply the sum rules to separate the spin and the orbital components of the magnetization. The magneto optical constant $\Delta\beta$(E) for the three samples is plotted in the right panel of the figure. This energy dependency of the $\Delta\beta$(E) shows the percentage of the dichroism effect. The maximum values of the $\Delta\beta$(E) reach 6%, 14%, and 8% for Fe, Co and Ni respectively.

We compare these values with the results obtained by Valenica *et al* in 2006[95]. Those authors measured the Faraday rotation at the $M_{2,3}$ absorption edges of Iron, Cobalt and Nickel. From this data, they derived $\Delta\beta$ using the Kramers-Krong relations [96].We note that the shape of the curves obtained in our experiments is in agreement with that of $\Delta\beta$ measured in [95]. The maximum values of the magneto optical constants $\Delta\beta$ up to 14% for Cobalt and 8% for Nickel as found by us are aligned with values reported in [95]. For Iron, the maximum value of the asymmetry does not fit with the literature. This may be due to the fact that the magnetization of the iron sample was not completely saturated out of plan.

One can also compare the XMCD measured at the 3p edges with these measured at the 2p edges. The 2p absorption edges L_2 and L_3 are well separated[24] while the 3p edges M_2 and M_3 are nearly overlapping. This is due to the above mentioned significantly smaller spin-oribt splitting of the 3p states with respect to the 2p states[97]. We can notice also that for the 2p edges the XMCD effect are directly proportional to the difference between the spin up and

spin down 3d densities of states[98]. Taking into account the effect measured for Co and Ni, we can say that this proportionality remains valid for the 3p edges as observed elsewhere [95].

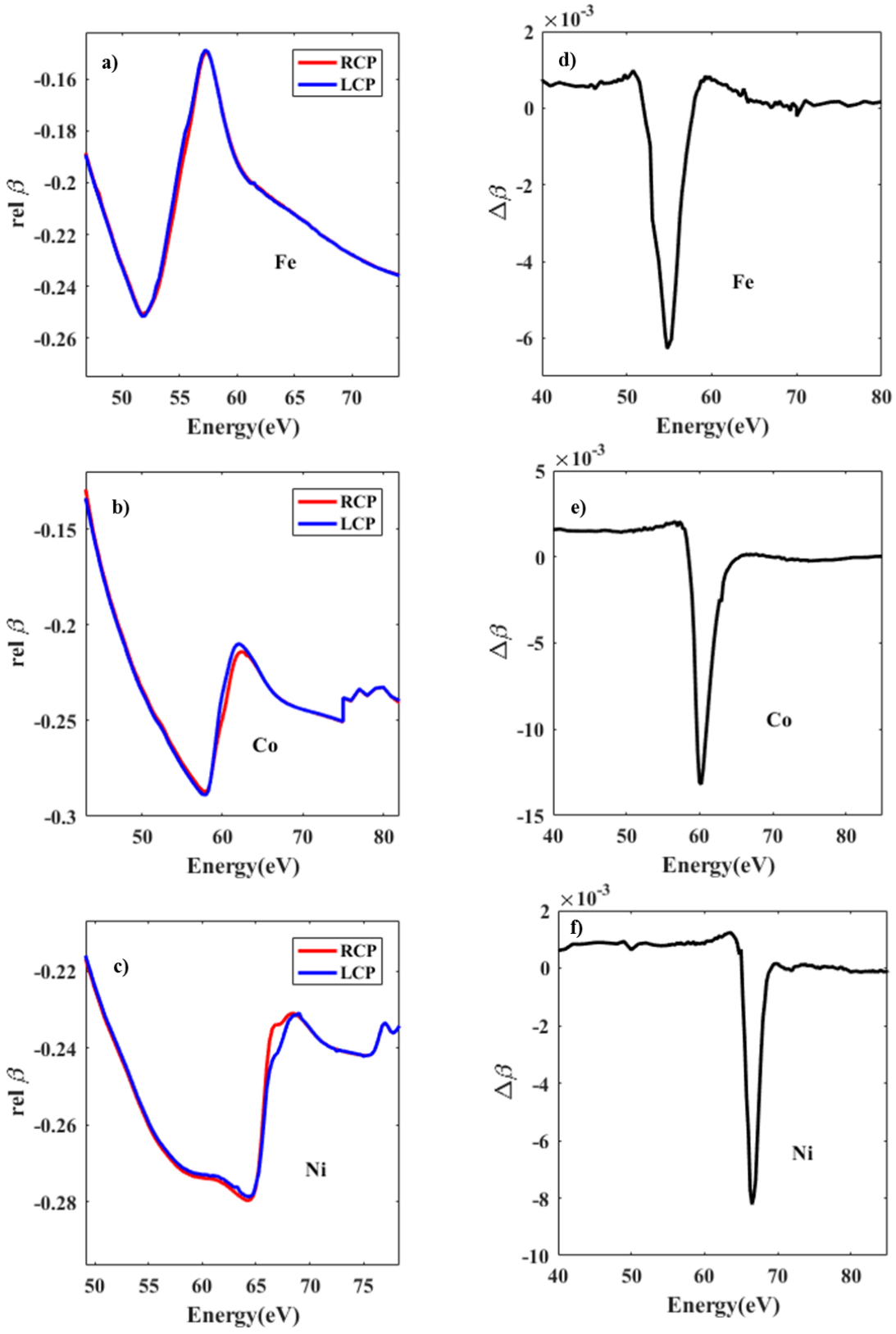

Figure 3-5: Absorption spectra as recorded with circularly left and right polarized light around the $M_{2,3}$ edges of a) Iron (52.7 ev) ,b) Cobalt (58.9 ev and 59.9 ev) and c) Nickel (68ev and 66.2ev). These spectra were measured in transmission at beamline UE112 (BESSY II). The derived magneto optical constant $\Delta\beta$ spectra are represented in d) for Iron, e) Cobalt and f) Nickel.

3.3.3 X-ray scattering cross sections

The scattering of X-rays by an atom is caused by interaction with the electron cloud. The classical model of X-ray scattering considers that the oscillating electric field of the incident radiation exerts a Coulombic force on the electrons, thus accelerating them. This leads to an oscillatory motion of the electrons. As any charged, accelerated particle, the electron therefore emits an electromagnetic wave, which frequency is given by the one of the incident radiation provoking the oscillation. Note that within this picture one can understand that the interaction with the nucleus does not give rise to (significant) X-ray scattering due to its higher mass.

The electron oscillates and emits the scattered X-ray. In an atom, all the electrons scatter the X-rays individually. The radiation emitted by the individual electron interferes. Therefore, the total scattering amplitude of the atom is given by the sum of complex scattering amplitudes of all electrons. This is described by the atomic form factor f(θ), where θ is the angle between the incident beam and the scattered beam[99]. Note that the atomic form factor corresponds to the Fourier transform of the charge density$\rho_e(r)$. Its amplitude in forward scattering (θ = 0) is directly proportional to the number of electrons, given by the atomic number Z. The mathematically representation of this factor is given by[20]:

$$F_0(Q) = \frac{-1}{e}\int \rho_e(r) e^{iQr} dr \qquad 3.7$$

where Q=k'-k=$\frac{4\pi sin\theta}{\lambda}$ is the s-called momentum transfer. Q is a vector of the reciprocal space, which is related to the real space by Fourier Transformation. The momentum transfer Q is therefore linked to a real space periodicity length scale *a* by Q=$\frac{2\pi}{a}$.

Thus, the amplitude of the non-resonant magnetic scattering is very small [100]and the atomic scatterings cross section which represent the scattered intensity into a solid angle Ω is expressed by

$$(\frac{d\sigma}{d\Omega})_{atom} = r_0^2 P|F_0(Q)|^2 \qquad 3.8$$

where r_0 is the Thomson scattering length or the classical radius of the electron (r_0=2.82 * 10^{-15} m). P=$|\vec{\varepsilon}.\vec{\varepsilon}'|^2$is the polarization factor, where $\vec{\varepsilon}$ and $\vec{\varepsilon}'$ are the unit polarization vector of the incident and scattered x-rays respectively. Note that within the current model, the cross

section is independent of the incident photon energy, which is a consequence of considering free electrons.

In resonant X-ray scattering, the energy of the incident photon coincides with the binding energy of a core electron (note that resonant scattering is also referred to as anomalous scattering, especially in the context of hard X-ray scattering). Consequently, the electron cannot be treated as a free electron anymore, since it can absorb the incident wave. The bound electron can be approximated as a harmonic oscillator, where the resonance energy is given by the electron binding energy [101]. The photon energy dependence of the atomic form factor can be written as[24]:

$$F(Q,E) = F_0(Q) + F'(E) - iF''(E) \qquad 3.9$$

$F'(E)$ is the real term that accounts for refractive contributions and $F''(E)$ is the imaginary part that accounts for absorptive contributions to the scattering process.

In the case of forward scattering (Q=0) the first term $F_0(Q)=Z$. The resonant forward scattering factor F(E) can be written as $F(E)= f_1(E)+if_2(E)$ with $f_1(E)=Z+F'(E)$ and $f_2(E)=F(E)''$ [24], [102]. These factors are known as the Henke-Gullikson scattering factors. The optical theorem [24] provides a direct link between scattering and absorption since the imaginary part of F(E) can be represented as a function of the absorption cross section or the absorption index $\beta(E)$ (see equation(3.4)) with:

$$f_2(E) = \frac{1}{2\lambda r_0}\sigma^{abs}(E) = \frac{4\pi}{\rho_a \lambda^2 r_0}\,\beta(E) \qquad 3.10$$

As mentioned before, the dispersion term $f_1(E)$ can be derived from $f_2(E)$ using the Kramers-Kronig relations[103]. To give an example, Figure 3-6 shows the energy dependence resonance factor of F'(E) and F"(E) corresponding to the Iron $L_{2,3}$ absorption edges.

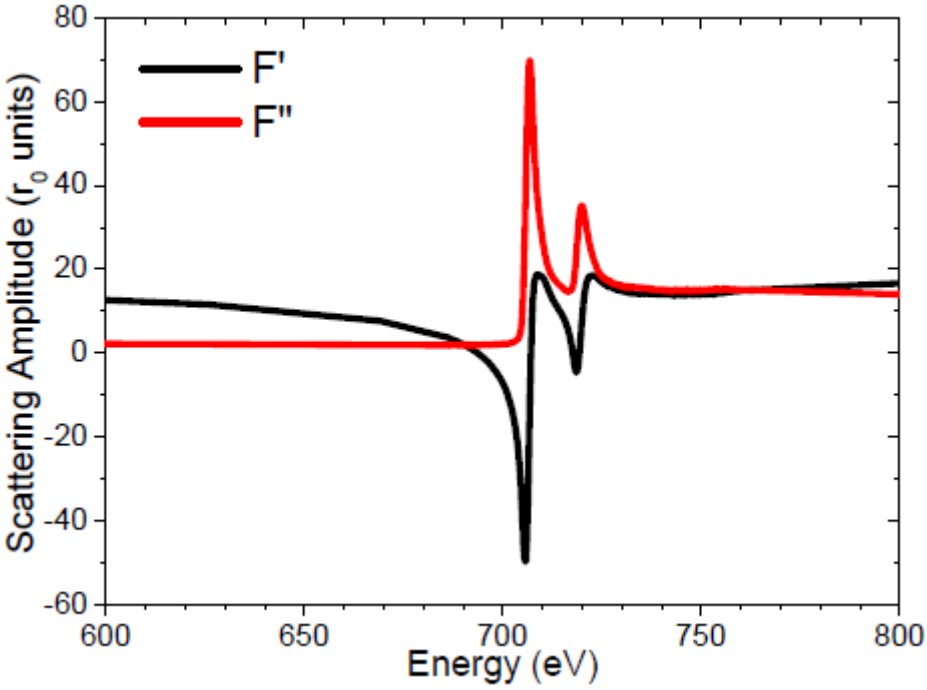

Figure 3-6: F' and F'' of Iron around the $L_{2,3}$ absorption edges[104].

We note that in quantum mechanics, the X-ray scattering cross sections and the absorption of X-rays can be determined within the framework of the perturbation theory. We consider |a> to be the ground state of the electron. When it absorbs a photon of energy $\hbar\omega \approx E_n - E_a$, the electron goes through an intermediary state where E_n and E_a represent the energies of the states |a> and |n>, respectively. Subsequently, it returns to its initial state by emitting a photon of the same energy. Therefore, the resonant elastic scattering differential cross section in dipole approximation is given by

$$\left(\frac{d\sigma}{d\Omega}\right)_{atom} = r_0^2 |F(E)|^2 = \frac{\hbar^2\omega^4}{c^2}\alpha_f^2 \left| \sum_n \frac{< a|r.\varepsilon'|n >< n|r.\varepsilon|a >}{\hbar\omega - (\mathrm{En} - \mathrm{Ea}) + i\left(\frac{\Delta_n}{2}\right)} \right| \qquad 3.11$$

With α_f is the fine structure constant and Δ_n is the resonance width. At the magnetic resonance the scattering amplitude is expressed by [105]

$$F(E) = f_{res}^{E1}(E) = f_0 + f_{circ}(E) + f_{lin}(E) \qquad 3.12$$

With

$$f_0 = (\varepsilon'.\varepsilon)G_0 \quad 3.13$$

$$f_{circ}(E) = i(\varepsilon' * \varepsilon)\hat{\mathrm{m}}G_1 \quad 3.14$$

$$f_{lin}(E) = (\varepsilon'.\hat{\mathrm{m}})(\varepsilon.\hat{\mathrm{m}})G_2 \quad 3.15$$

$\hat{\mathrm{m}}$ is the unit vector of the magnetization and $G_{0,1,2}$ are the dipole transition matrix elements. We remark that the three terms have different polarization properties. The first term f_0 is independent of the material's magnetization with incident photons and describes the resonant charge scattering. The second term f_{circ} depends linearly on the magnetic moment and it is the analogue of XMCD in absorption spectroscopy[105], [106]. The third part, which depends quadratically on the magnetic moment, is the X-ray Magnetic Linear Dichroism effect in scattering (XMLD)[98]. XMLD is generally employed to study antiferromagnetism. It is important to note, that in our experiments the polarization of the electric field vector is always perpendicular to the magnetization direction. The XMLD contribution thus vanishes, since $\varepsilon.\hat{\mathrm{m}}=0$.

The relation between X-ray scattering and X-ray absorption can also be found for magnetic samples from the imaginary part of the elastic resonant magnetic scattering amplitude F(E).

$$Im[F(E)] = f_2^{\pm}(E) = \frac{1}{2\lambda r_0}\sigma_{\pm}^{abs}(E) \quad 3.16$$

$$f_2^{\pm}(E) = \pm fm$$

Where the + and – in this equation corresponds to parallel and antiparallel orientation of circular polarization and magnetization. As discussed above, f_0 is the charge contribution to the resonant scattering and f_m is the polarization-dependent XMCD effect ($f_{circ}=f_m$).Using equation (3.4) and equation3.16) the linear absorption coefficient can be represented in function of the imaginary part of the resonant scattering factor by

$$\mu_x^{\pm}(E) = \rho_a\sigma_{\pm}^{abs}(E) = \rho_a 2\lambda r_0 f_2^{\pm}(E) = \rho_a 2\lambda r_0(\pm f_m) \quad 3.17$$

We remark that for the experiments presented in this manuscript the contribution of charge scattering can be neglected. The reason for this is that the samples do not exhibit any charge heterogeneity on the length scale of relevance for the investigated magnetic scattering.

3.3.4 Resonant small X-ray scattering from magnetic stripe domains

In this part, we will discuss the resonant X-ray scattered intensity obtained from magnetic samples presenting a network of stripe domains with opposite out of plane magnetization direction as shown in section 2.3.1. We will limit this discussion to the case of small angle X-ray scattering in transmission geometry (SAXS).

The incident X-rays are scattered by the sample's magnetic domain pattern. As discussed above the intensity of the resonant magnetic scattering depends on the energy, i.e., the wavelength of the incident x-rays. Scattering is observed at the momentum transfer Q =k-k' with the incident wave vector k and k' the scattered wave vector; $|k|=|k'|=\frac{2\pi}{\lambda}$ (elastic scattering). An illustration of the small angle scattering (SAXS) from a network of magnetic stripe domains is shown in the Figure 3-7 below. In this SAXS geometry the modulus of Q is given by

$$|Q| = \frac{4\pi}{\lambda} sin\theta \qquad 3.18$$

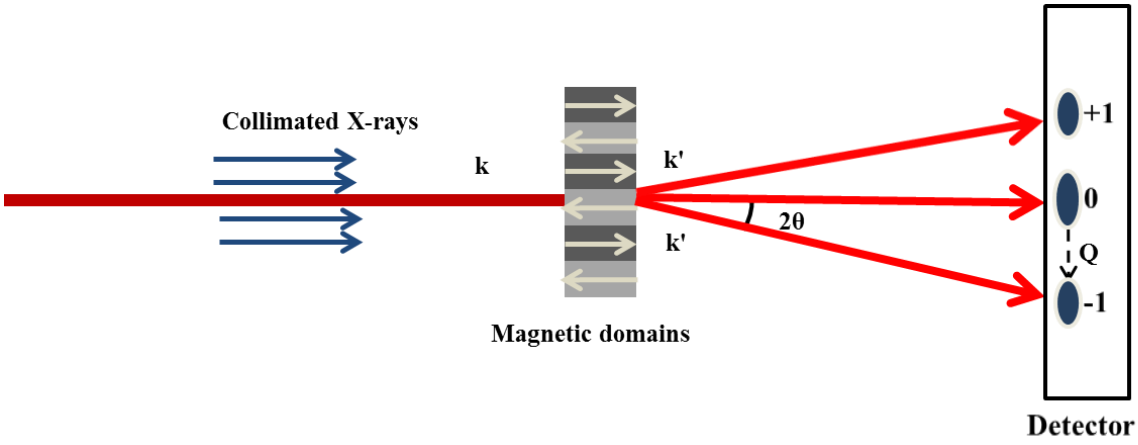

Figure 3-7: Illustration of small-angle scattering in transmission geometry from a magnetic stripe domain. The angle between the scattered beam and the incident beam is termed as 2θ and represents the scattering angle. The momentum transfer Q is given by the difference between the scattered (k') and the incident (k) wave vector. The pattern on the detector shows the positive and negative spots obtained from the first order of scattering.

We showed in equation 3.7) that the amplitude of the scattered waves is given by the Fourier transform of the electron density $\rho(\vec{r})$. Let us suppose that in the Fourier space this amplitude

is given by $A(\vec{q})$. The electron density $\rho(\vec{r})$ in return is obtained as the inverse Fourier transform of the amplitude function $A(\vec{q})$:

$$\rho(\vec{r}) = \frac{1}{(2\pi)^3} \int A(\vec{q})\, e^{i\vec{q}\vec{r}} dv_q \qquad 3.19$$

X-ray detectors, however, cannot detect the scattering amplitude A(q), but measure the scattering intensity $I(\vec{q})$. This leads to phase problem where we lose any information about the relative phases of diffraction. In order to determine the structure of the scattering data, one has to solve the phase problem.

The magnetic scattering intensity I(Q) is given by the modulus of the Fourier transform of the scattering amplitudes $A_n(q)$ originating from the lattice sites n located at position r_n [27]–[29].

$$I(Q) = |\sum_n F_n \exp(-iQr_n) = |\int_V F(r) \exp(iQr)\, dr\,|^2 \qquad 3.20$$

Where the scattering amplitude F_n is given by equation (3.12). The sum in equation 3.20) runs overs effective domains instead of single scatters [109].

As motivated above, the charge scattering can be neglected and the scattering intensity can be written as [9], [110]

$$I(Q) \alpha\, |\int_v \left(k_0 . \hat{m}(r)\right) G1 \exp(iQr)\, dr|^2 \;\alpha\; |\int_A m_z(r) \exp(iQr)\, dr|^2 \qquad 3.21$$

with $k_0 = \varepsilon' * \varepsilon$ the cross product of the polarization unit vectors in equation 3.14). Note that k_0 is also the unit vector of the incident X-rays. The magnitude of the magnetic moment is assumed constant throughout the magnetic sample and that the X-ray radiation propagates along the sample depth, in the z direction. The period area is denoted by A and $-1<m_z(r)<1$ represents the local out of plane components of the magnetization. It follows from the last equation that the magnetic scattering intensity I(Q) is proportional to the squared modulus of the two dimensional Fourier transform of the magnetic domain pattern $m_z(r)$.

Alternatively, the scattering intensity of a magnetic sample exhibiting an ordered domain structure of alternative up and down magnetic domains with equal width can be derived using a one dimensional model[107], [111] (see Figure 3-8). The magnetization profile is expressed as a convolution of the magnetic unit cell with a lattice structure:

$$m(x) = \sum_{n=-\infty}^{\infty} f(x - nd) = f_m(x) * \sum_{n=-\infty}^{\infty} \delta\,(x - nd) \qquad 3.22$$

where $f_m(x)$ represents the magnetic unit cell consisting of an up and down domain pair and the sum of δ functions represents the points of the lattice with the domain period d.

The Fourier transform of the convolution product of equation 3.22) is the product of the Fourier transforms of both constituents. We thus obtain from equation 3.22):

$$F_m(Q) = f_m(Q).\sum_{n=-\infty}^{\infty} exp(-iQnd) = f_m(Q).\frac{2\pi}{d}\sum_{n=-\infty}^{\infty} \delta\left(Q - n\frac{2\pi}{d}\right) \qquad 3.23$$

Where $f_m(Q)$ is the Fourier transform of the magnetic unit cell, i.e., so to speak the magnetic form factor of the scattering object. Using equation (3.23), the SAXS intensity can be expressed by

$$I(Q) = |F_m(Q)|^2 = |f_m(Q)|^2.|\sum_{n=-\infty}^{\infty} \exp(-\mathrm{iQnd})\,|^2 = |f_m(Q)|^2 S(Q) \qquad 3.24$$

S(Q) is the so called structure factor and accounts for the spatial configuration of the scattering objects. We will use these relations in Chapter 4 to derive an interpretation of the magnetic diffraction pattern and their correlation with the real-space domain structure.

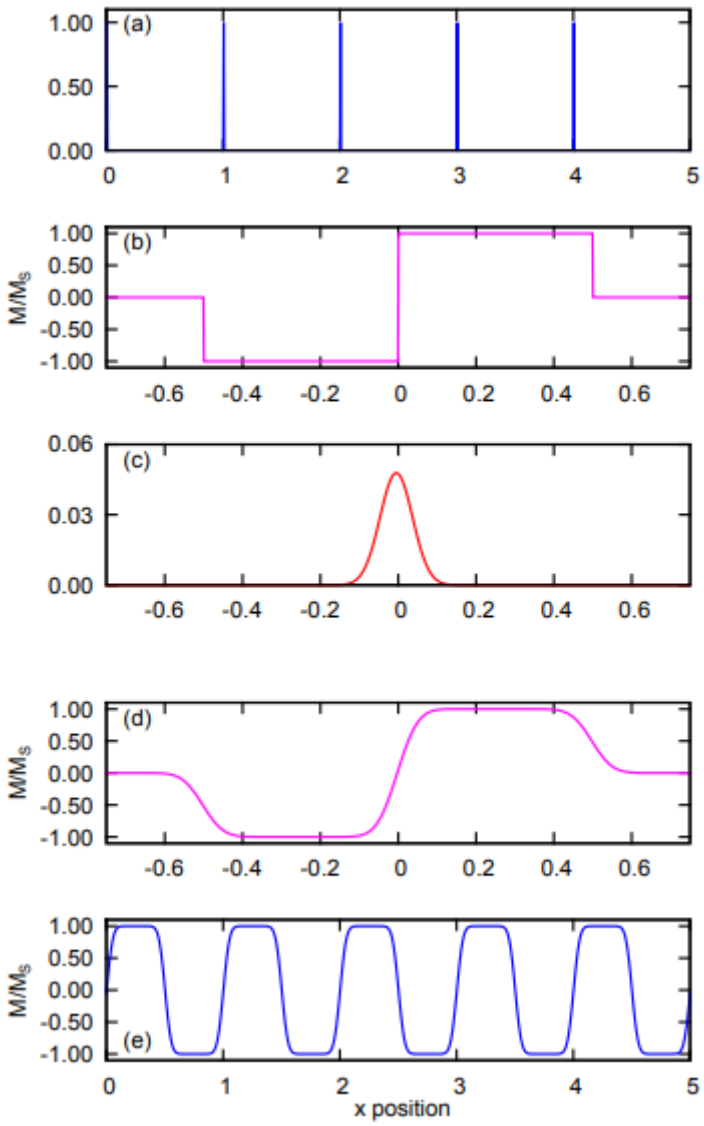

Figure 3-8: Illustration of the magnetization profile considering one-dimensional domain model extracted from the supplementary discussion of [9]. a) Lattice structure in the real space. b) Magnetic unit cell. c) Kernel of the smoothing function. d) Smoothed magnetic profiles obtained by convolution of c) and b). e) The complete model structure obtained from the convolution of a) and d). This model is described by equation 3.22.

3.3.5 Multi-color imaging of magnetic domain structures

The XMCD effect can be exploited as contrast mechanism for X-ray imaging of magnetic domain structures. This presents the possibility to image domains in heterogeneous magnetic materials composed of different elements. Taking into account the two color scheme of Free Electron Lasers like FERMI, it's possible now to record real space images corresponding to a distinct element of the investigated sample. As a direct application of the different parts presented in this chapter, we will present in the following the first experimental realization of a coherent imaging experiment of a Co/Pt multilayer sample with a simultaneous and direct access to the element specific magnetization of the two constituents Co and Pt.

In this experiment, we used Fourier Transform Holography as imaging technique, which is ideally suited for XFELs and which yields a spatial resolution of 50 nm or better [87]. In this holography version, the radiation of the object is superposed with a reference wave originating from an object positioned on an adjacent site of the sample. In the far field, the radiation of the reference and the object interfere and lead to the formation of a hologram (see Figure 3-8d). The real space image of the object is reconstructed by calculating the two dimensional Fourier transform (2D) of this hologram. A more detailed description can be found in Ref. [87], [112].

In order to realize the two color imaging we employed the two color scheme implemented at FERMI[90] and described in section 3.2.3. In this study we were interested in a simultaneous arrival time of the XUV pulses. For this we used the two color scheme which employs a single seed pulse to generate coherent XUV radiation with a photon energy given by multiple harmonics of $\boldsymbol{\lambda}_{seed}$. In two subsections of the undulator the FEL wavelengths are tuned to multiple harmonics of the seed laser $\boldsymbol{\lambda}_{seed}$/m and $\boldsymbol{\lambda}_{seed}$/n. By changing the wavelength of the seed laser and the number of the amplified harmonics (by modifying m and n) different probe wavelengths are obtained. The goal was to choose the FEL wavelengths such that the magnetic contrast for Pt and Co is comparable. In Figure 3-9.a) we show the FEL energy as a function of the seed wavelength for harmonics H12 to H15. In Figure 3-9.b) we present the magnetic domain contrast for the two edges as a function of the probing energy. The graph shows that the optimal FEL wavelength correspond to $\boldsymbol{\lambda}_{FEL,1}$=20.2 nm for Co and $\boldsymbol{\lambda}_{FEL,2}$=17.3 nm for Pt. This is indicated by the solid orange lines in Figure 3-9.a).b).

The FTH mask geometry was chosen such that spatial overlap between the two images was avoided. For this, two reference holes separated by 13 μm were added to the mask, which is sufficient to separate in the reconstruction the images of the 2 μm sized object recorded at the two different wavelengths. More information about the sample design and the experimental setup can be found in [113].

We recorded holograms for circularly right and circularly left polarized XUV pulses. The difference between these two holograms emphasis the magnetic contribution. This is shown in Figure 3-9.c). One notes that the magnetic scattering extends all the way to the detector edges, which is a prerequisite to obtain a high spatial resolution. Calculating the two dimensional Fourier transforms of these holograms, we get simultaneously the real space image of the magnetic domain pattern recorded at the edge of Co and Pt shown Figure 3-9.d). This demonstration of multi-color imaging paves the way for imaging of ultrafast dynamics in complex materials composed of different constituent elements.

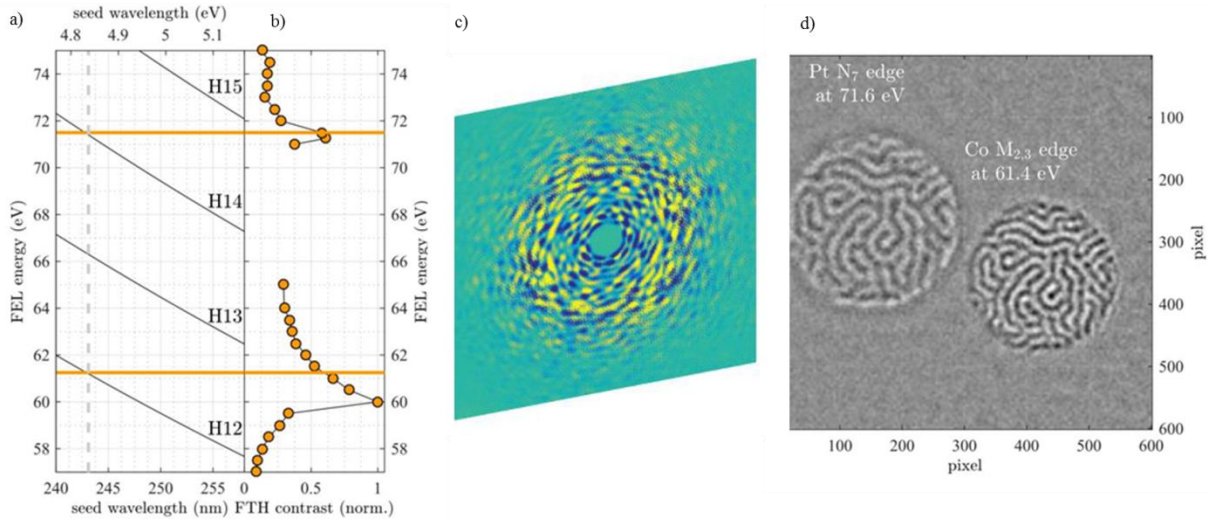

Figure 3-9 a)b) FEL energy as a function of seed wavelength shown for harmonic H12 to H15. As one can see, for $\boldsymbol{\lambda}_{seed}$=242.2 nm the magnetic domain contrast at the Pt N7 edge at 71.6 eV (H14) is comparable to the signal H12 at 61.4 eV at the Co $M_{2,3}$ edges. c) Hologram pattern obtained as the difference between the images obtained for right and left circularly polarized light . d) Reconstruction of the magnetic domain pattern for Pt and Co reconstructed from the two color difference hologram.

4 Ultrafast demagnetization of CoTb

4.1 Introduction

In this chapter we discuss the ultrafast laser induced dynamics of CoTb on short (< 1 ps) and longer (up to 150 ps) timescales. To investigate these dynamics we used the resonant small angle X-ray scattering technique, introduced in section 3.3.4. First, we present the experimental setup and the data analysis of the experimentally recorded scattering patterns, from which we extract the structure factor S(Q). We then discuss the temporal evolution of the magnetization as a function of the IR pump fluence. We show that for our CoTb films, the characteristic time of the ultrafast magnetization drop is independent of the excitation fluence. Next, we compare the individually probed dynamics of the Co and Tb sub-lattices. The thermalization time of the Tb lattice found in this study is significantly shorter than the values reported in the literature for other CoTb compositions.

Our main experimental results are presented in section 4.4.3, where we present the temporal evolution of the first and third scattering order detected at the Co M_3 edge. The ratio between these two orders provides information on the modification of the sample's magnetic domain structure. To interpret these data, we employ two different models that establish a link between the detected scattering intensities and the domain wall width. Using these models we find evidence for a broadening of the domain wall width on the time scale of a few picoseconds. We argue that the main reason behind this wall widening is the reduction of the uniaxial anisotropy due to the thermal heating of the lattice. At the end, we investigated the ultrafast dynamics of the Co/Pt multilayer by following the magnetic domain structure as a function of pump-probe time delay.

4.2 Beamline and setup

The resonant small angle X-ray scattering experiments reported here were carried out at the DiProI(Diffraction and Projection Imaging) end station of the FERMI free electron laser at the Elettra laboratory in Italy. This instrument meets the requirements of different coherent scattering experiments[114] which range from resonant magnetic small angle X-ray scattering to Fourier Transform Holography [87] and Coherent Diffraction Imaging[115]. The polarization of the seeded FERMI can be fully controlled [116]. The pulse wavelength covers the spectral range from ultraviolet to soft x-rays[116].

Figure 4-1 gives an overview of the IR pump - XUV probe setup. One notes that this is an essentially jitter-free setup, since the IR laser pulse is intrinsically synchronized with the FEL pulse [117]. This synchronization comes from the fact that a fraction of the IR pulse used to seed the FEL is employed to pump the sample. The delay line between the two pulses is implemented on the optical path of the pump pulse as one can see in the Figure 4-1. The XUV probe pulse is generated by FEL-1 (see section 3.2.3). At the entrance flange of the DiProl chamber, a four quadrant photodiode provides an accurate shot to shot measurement of the FEL intensity. This allows normalizing the detected scattering intensity by the incoming photon flux (I_0). In addition this device allows monitoring the pointing stability of the beam. For the probe beam, we used 50 fs short XUV pulses which photon energy was tuned either to the Cobalt M_3 absorption edge at 20.8 nm (59.6 eV) or the Terbium O_1 absorption edge at 27 nm (45.9 ev). The wavelength of the IR pump pulse was 780 nm and the pulse duration was ~100 fs. On the sample, the angle between the pump and the probe pulse is very small, which avoids degradation of the achievable time resolution. The investigated sample was a 50 nm thin $Co_{88}Tb_{12}$ film, which presents a network of opposite stripe domains. For the detection system an in vacuum charge coupled device (CCD) detector with a pixel width of 13.5 um was posed 4.95 cm behind the sample. To increase the read-out speed the CCD pixels have been binned 2 by 2 yielding an effective pixel size of 27 μm. In order to block the intense transmitted beam, a cross like beam stop was placed in front of the CCD camera. This beam stop was oriented such that it does not cover the magnetic scattering peaks.

The spot size diameter of the probe and the pump beam are respectively 190 *180 μm^2 and 400*400 μm^2. The focal size ensures a uniform illumination across one membrane of 200 um. In the present measurements, we investigated the demagnetization dynamics of the CoTb

sample after pumping with three different laser fluence values (3.7 mJ.cm^{-2}, 5 mJ.cm^{-2}, and 8 mJ.cm^{-2}).

At this magnetically dichroic absorption resonance, the magnetic domain structure of the film acts like a diffraction grating and the positive and negative scattering orders are recorded as shown in Figure 4-1.a). One can see clearly that these spots are perpendicular to the magnetization of the stripe domains.

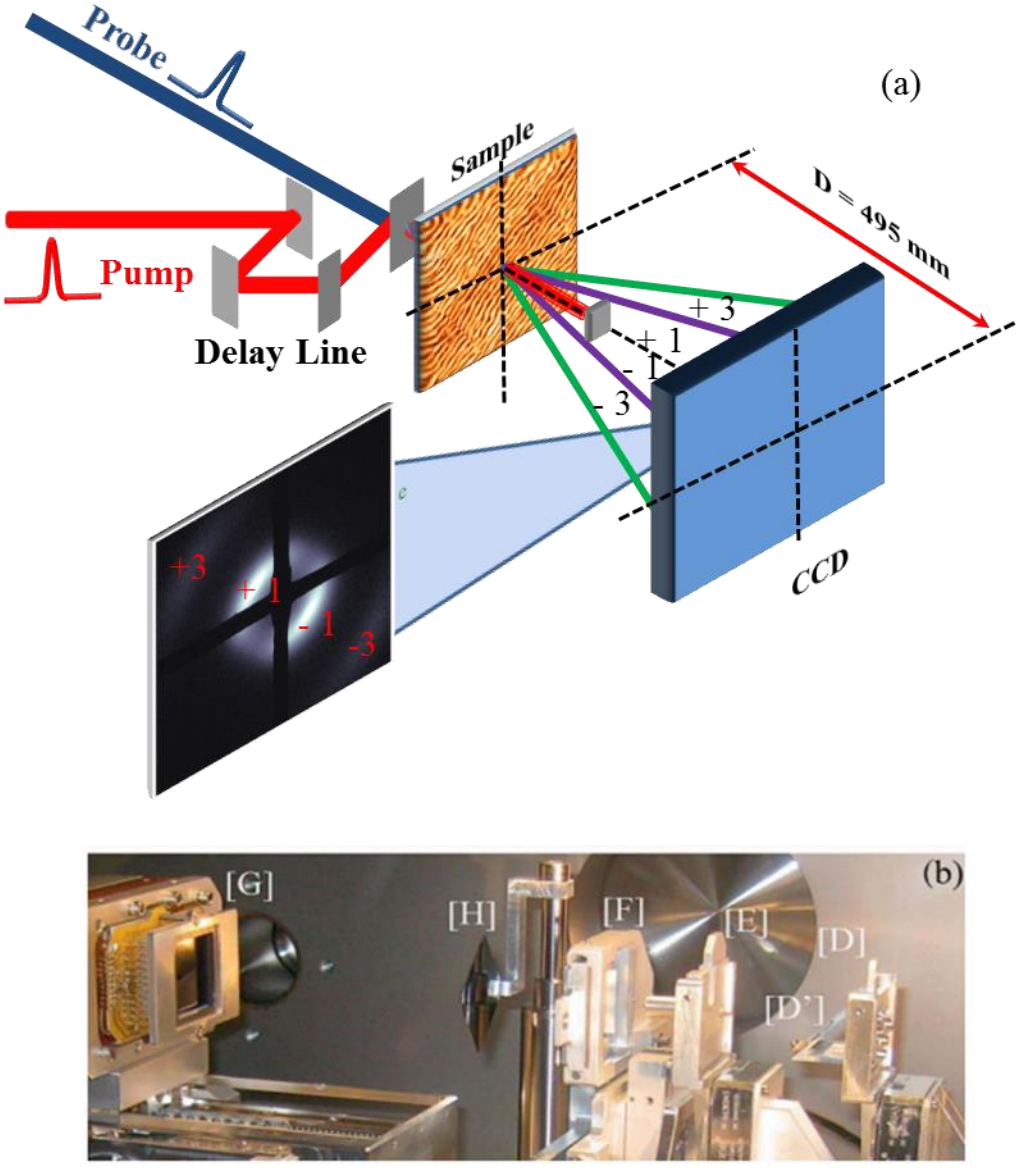

Figure 4-1: a) Illustration of the pump probe configuration used in the resonant small angle X-ray scattering experiment at DiproI. Positive and negative scattering orders recorded at the Co M_3 edge give rise to the intense spots on the CCD camera. b) Photo of the experimental setup inside the DiProI vacccum chamber (from Ref [6]). The beam pass through the aperture

set [D], the screening plate [E] carved off the stray radiation, [F] is the sample, [H] is the beam stop and the [G] is the CCD where diffraction pattern are detected.

4.3 Data treatment

The panel in Figure 4-1.a) shows a typical resonant magnetic diffraction pattern as recorded at the Co absorption edge by the CCD camera for a given time delay. Prior to analysis, all images have been background corrected by subtracting a reference dark image. The preferential alignment of the magnetic domain gives rise to the concentration of the scattering intensities in spots which are the positive and negative first and third scattering orders of the grating-like domain structure. The vanishing of even diffraction orders asserts that the up and down domains have equal width.

For each delay the scattering intensity of the first and third order is extracted by summing up the integrated intensity of the plus and minus area indicated by the blue regions for the third order and red regions for the first order, see Figure 4-2.b). In this figure we chose a logarithmic scale of the scattering intensity in order to display both, the first and third scattering order. This scattering intensity is then divided by the I_0 intensity detected by the 4 quadrant diode.

One can see two small points in the bottom left and the top right of the Figure 4-2.a). These two spots correspond to the diffraction pattern of the Al grating deposited on the top of the sample oriented perpendicularly to the magnetic stripe domains. This scattering intensity gives an additional I_0 signal, which can be used alternatively to the signal of the 4 quadrant diode. To analyze the data in more detail, we have renormalized the scattering intensity for each delay by referencing it to the intensity recorded for negative delays where the system is unpumped.

In equation (3.23), we showed that the scattering intensity is proportional to the form factor and the structure factor. Thus, the position of the first scattering order in Fourier space delivers information about the domain periodicity and orientation. The scattering intensity of the first order is proportional to the mean magnetization profile of the domains. The ratio between the first and third order scattering intensity provides information on the magnetic wall separating two opposite domains.

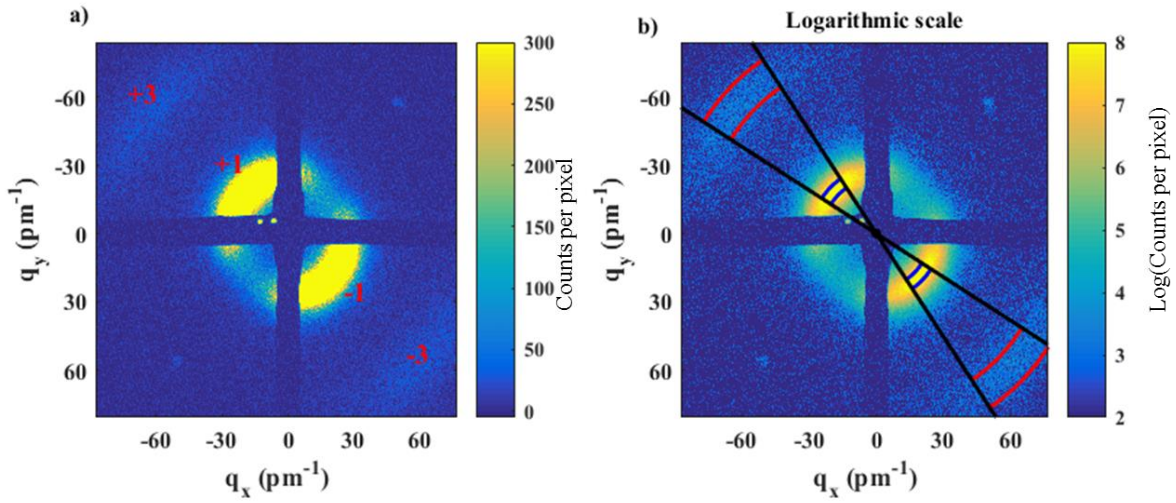

Figure 4-2: a) Resonant magnetic scattering pattern recorded at the Co M_3 edge (59.6 eV). One can see the positive and negative first and third scattering order. Note that even orders are suppressed because opposite domains have the same size. The linear color scale is saturated to render the third order visible. b) Same as (a) but on a logarithmic color scale. The integration boundaries for 1st and 3rd order of scattering are indicated.

In order to study the spatial distribution of the scattering intensities we performed an angular integration which yields the radial distribution of the scattering intensity as a function of the momentum transfer magnitude q.

In Figure 4-3.b) we plot in logarithmic scale the radial integrated of the scattering intensity at the Co edge as a function of the scattering vector q. The wave vector q in nm^{-1} is calculated according to the following relation [11]:

$$q = \frac{4\pi}{\lambda} sin\left(\frac{1}{2} arctan\left(\frac{Pixelwidth * r}{D}\right)\right) \qquad 4.1$$

with $\boldsymbol{\lambda}$=20.8 nm (Co edge), D = 4.95 cm as the distance between the CCD camera and the sample, a pixel width of 27 μm, and r the radial distance in number of pixels.

The momentum transfer q corresponding to the peak positions of these radial profiles reveals information on the magnetic domain structure as we will show later. The temporal evolution of the local magnetization is revealed by the variation of the intensity of the peak of these radial integrals as a function of pump-probe delay.

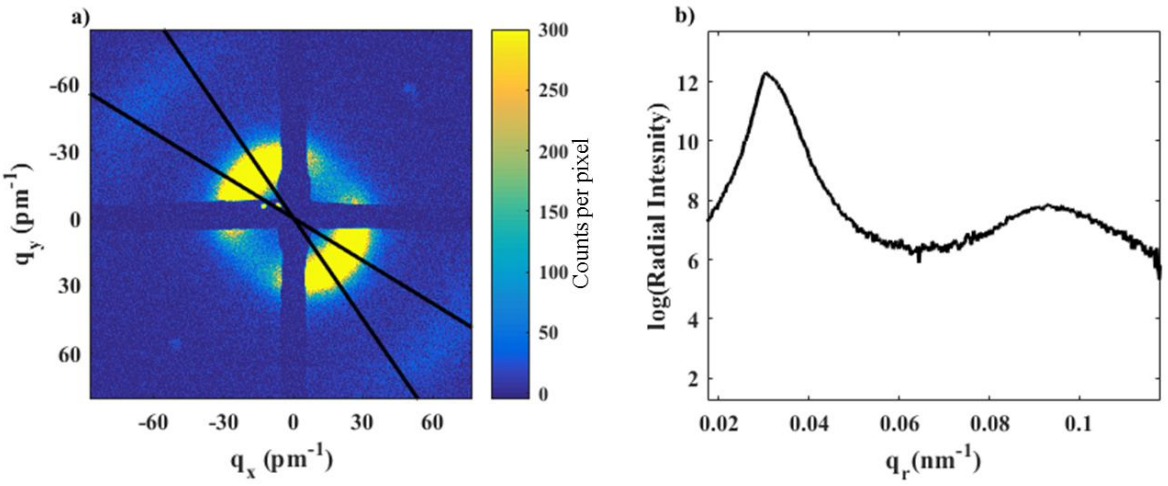

Figure 4-3: a) Cone representing the area used for angular integral. b) Radial integral of the selected conic area as a function of the momentum transfer q.

4.4 Results and discussion

4.4.1 Fluence dependence of the ultrafast demagnetization

In this section we discuss the temporal evolution of the magnetization at the Co edge as a function of pump fluence. Here, we are interested in the ultrafast magnetization quenching following immediately the laser excitation. We therefore focus on short time delays only up to 3 ps. In Figure 4-4, we show the normalized intensity of the first scattering order as a function of the time delay for three different pump fluence values. Note that the intensity is proportional to the square of the magnetization, $I \alpha |M^2|$, as we discussed in section 3.3.4. The right axis of the figure indicates the derived magnetization (M), which is normalized to the unpumped magnetization (M_0).

We can see that these three curves exhibit similar behaviors. The intensity pursues an ultrafast drop during the first hundreds of femtosecond which is followed by a partial recovery that occurs on a slower time scale. This initial intensity drop manifests the rapid decrease of the magnetization within each magnetic domain. The partial recovery of the magnetization is attributed to the equilibration between the hotter spin and the phonon bath which is still colder at this moment in time.

As expected, the demagnetization amplitude increases with increasing pump fluence. A demagnetization of 12 % is observed for the highest pump fluence of 8 mJ.cm^{-2}. The time

needed to reach the transient minimum of the magnetization, however, is similar for the three fluence values. This observation indicates that in this material the time constant of the ultrafast magnetization quenching is independent of the IR pump fluence. This observation was also made before for other systems like Co/Pd multilayers [11], [119]. We remark that this observation is in contradiction with other studies which found that with increasing pump fluence the demagnetization takes more time to reach the minimum value. One notes that the difference between these studies is that in the latter case optical probe methods were employed to follow the ultrafast dynamics of transition metals samples like Co and Ni [39], transition metals multilayers like Co/Pd and Co/Pt[120]. It is thus interesting to ask whether this difference may be caused by an artifact affecting one (or both) types of experimental techniques. This point should be addressed in future studies.

To evaluate quantitatively the temporal evolution of the magnetization we used an analytic expression [1] to fit these 3 curves. This expression is derived from the three temperature model [1] assuming that the spin specific heat is negligible and that the laser excitation triggers an instantaneous increase of the electron temperature [120]–[122]. This analytical expression allows us to extract parameters like the achieved degree of demagnetization and the time constants for demagnetization and relaxation. It is given by:

$$\frac{\mathrm{I(t)}}{\mathrm{I_0}} = [1 - [\left(\frac{A_1}{\sqrt{\frac{t}{\tau_0} + 1}} - \frac{(A_2\tau_E - A_1\tau_M)\exp\left(\frac{-t}{\tau_M}\right)}{\tau_{E-}\tau_M} - \frac{\tau_E(A_1 - A_2)\exp\left(\frac{-t}{\tau_E}\right)}{\tau_{E-}\tau_M} \right) * \theta(t)]^2] * \Gamma(t, \tau_G) \quad (4.2)$$

I(t) is the scattering intensity at a time delay t, I_0 is the scattering intensity of the unpumped system, A_1 represents the amplitude of the degree of partial recovery once electrons, spins and lattice have reached thermal equilibrium. A_2 measures the initial magnetization quenching, τ_M is the time constant of this quenching and τ_E is the characteristic time of the magnetization's partial recovery. $\theta(t)$ is the step function that sets the expression to zero for negative time delays. The experimental time resolution is given by the convolution of the probe and pump pulse. Assuming Gaussian pulse shapes, the time resolution is also given by a Gaussian function $\Gamma(t, \tau_G)$, with τ_G the full width at half maximum (FWHM) of the

combined time resolution. Note that a common offset was subtracted from all delay scans such that pump - probe time overlap correspond to t = 0 ps.

In order to compare the demagnetization dynamics during the first 3 ps, we summarize in table 3 the values of demagnetization rate, demagnetization time τ_M and relaxation time τ_E obtained by fitting the data with the analytical expression. We find that τ_M is within the given uncertainty the same for all three curves (110 fs$\pm$30 fs). This indicates that the fit model confirms our qualitative observation.

In the following, we will discuss these derived characteristic time scales of τ_M and τ_E . In a former publication, Lopéz *et al* [123] investigated the ultrafast demagnetization dynamics of Co in $Co_{0.74}Tb_{0.26}$, $Co_{0.86}Tb_{0.14}$ and $Co_{0.8}Gd_{0.2}$ at the femtoslicing source of BESSY (Germany). A similar thermalization time for Co (τ_M =200 $\pm$ 40 fs) was found for the $Co_{0.74}Tb_{0.26}$ and $Co_{0.8}Gd_{0.2}$. However, a comparison of the Co demagnetization dynamics for the two CoTb samples was not reported. They proposed also that in the vicinity of Tc the demagnetization time of these alloys is inversely proportional to T-Tc. These results are confirmed by Atxitia *et al*. [124] based on the LLB model, which shows that τ_M scales with $1/(T - T_C)$ when T is close to T_C. This means that when approaching Tc the demagnetization dynamics of the TM element become slower. One notes that our sample is richer in Co than the other alloys studied by Lopéz *et al* [123]. Due to this we expect a higher Curie temperature of the $Co_{0.88}Tb_{0.12}$ alloy[125]. While the working temperature of our experiment T=420 K is very close to that reported in [123]. Therefore, we can claim that demagnetization time found (τ_M =110$\pm$ 30 fs) in our measurement at the Co M_3 egde, is lower than that reported by López-Flores *et al* [123].

The characteristic time of the magnetization recovery increases slightly while increasing pump fluence which is in line with what has been observed previously[126].

Fluences ($mJ.cm^{-2}$)	$1-M/M_0$ (%)	τ_M (fs)	τ_E (fs)
3.75	6	110$\pm$30	880$\pm$50
5	8	105$\pm$30	970$\pm$40
8	11	110$\pm$30	1400$\pm$150

Table 3: Demagnetization rate and characteristic values of the demagnetization dynamics for different pump fluencies

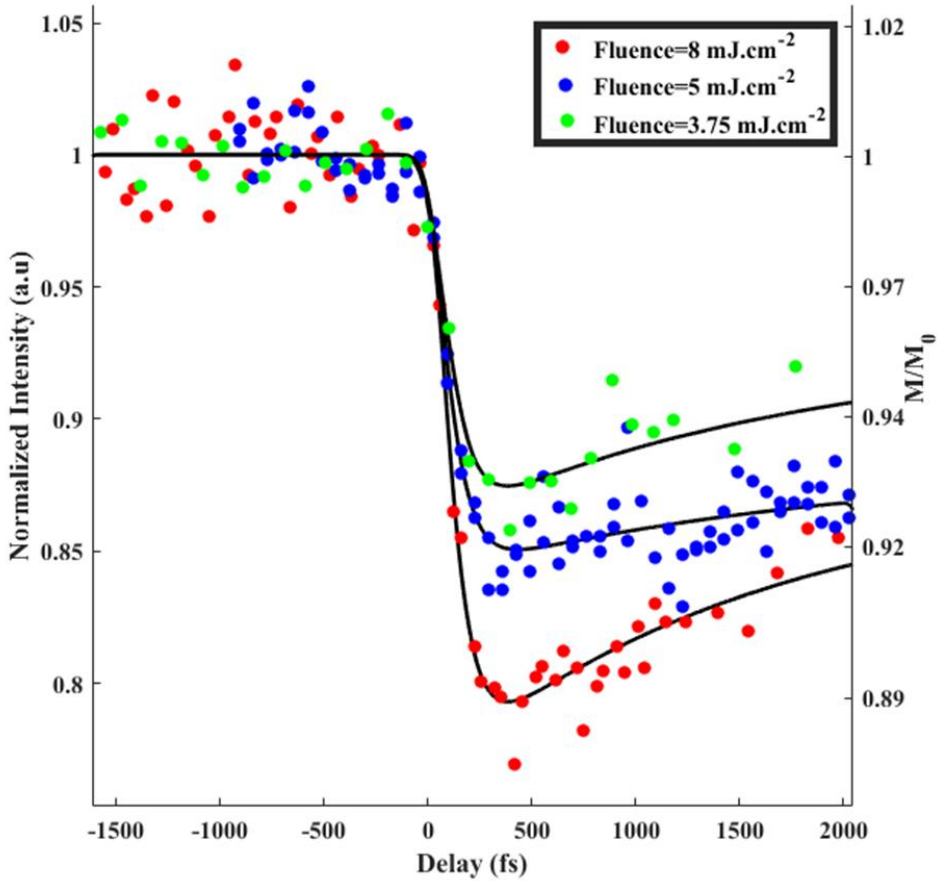

Figure 4-4: Scattering intensity as function of delay for the different pump fluences 8 mJ.cm$_{-2}$ (red symbols), 5 mJ.cm^{-2} (blue symbols) and 3.7 mJ.cm^{-2} (green symbols). The left y axis shows the magnetic signal after calculating the square root of the normalized intensity. The solid lines are the best fit obtained for each curve by using equation (4.2). The characteristic demagnetization times τ_M found are all around 110 fs $\pm$ 30 fs.

4.4.2 Probing the individual dynamics of the Co and Tb sub-lattice

Previous studies have shown that transition metal layers [127] and rare earth layers [128] exhibit different laser pulse induced magnetization dynamics. These differences reflect the different electron localization in these materials. While in 3d metals electrons are delocalized, 4f electrons are localized in orbits with well-defined angular momentum[50], [128]. Generally one finds that magnetic transition metals (Ni, Fe, Co) have faster demagnetization dynamics than rare earth materials (Tb, Gd, Dy..). This hold true even in the case of TM-RE alloys[123], [129], [130]. The induced excitation of the two sub-lattices has been intensively

investigated in such TM-RE alloys by probing selectively the magnetization dynamics of the 3d elements with their itinerant electrons and the 4f elements with their localized electrons[109], [111]. We note that this type of experiment has been realized before on CoTb alloys[123], [132]. However, published data focus on the femtosecond dynamics of the Tb sub-lattices obtained for different sample compositions and compensation temperature. In addition to repeating these measurements we add data extending to longer time scales.

We will compare the temporal evolution measured at the edge of Co and Tb of the $Co_{88}Tb_{12}$ sample in the case of the highest pump fluence ($F=8\ mJ.cm^{-2}$), where the demagnetization rate is the strongest and any difference between the sub lattice dynamics should be the most pronounced. It shall be mentioned here, however, that we found similar behavior for lower pump fluence values.

In Figure 4-5, we present the normalized intensity of the Co and Tb first scattering order as a function of pump-probe delay. The quantitative analysis of the demagnetization dynamics is carried out using the same analytical equation 4.2) as before.

A first observation is that these element selective demagnetization curves have within our time resolution the same t_0. This indicates the absence of a significant delay between the onsets of the two dynamics as observed. We note that for both elements the intensity drops initially by ~20 %, which indicates very comparable degrees of magnetization quenching. On the other hand, it is obvious that the demagnetization dynamics at the Tb edge is significant slower than the dynamics revealed at the Co edge. We note that this observation of a faster dynamics for the TM component is consistent with observations reported in the literature [123], [132].

Once the magnetization reaches its minimum value, the two curves exhibit distinctly different dynamics. At the Co edge, the data show that a partial recovery takes place, while the Tb data do no indicate any significant recovery. One can see this clearly in Figure 4-5.b) where we plotted the normalized intensity for longer delays, up to 40 ps.

In the section 4.4.1 we compared the characteristic time of demagnetization dynamics at the Co edge with other studies reported in literature. In the following we will discuss the demagnetization dynamics measured at the Tb edge in the $Co_{88}Tb_{12}$ alloy. The thermalization time ($\tau_{M=}$ 220 fs) of Tb in this alloy is two times smaller than the demagnetization time found in pure Tb[128]. In the literature, the characteristic time of this intensity drop at the Tb edge in CoTb alloys depends on the sample composition[123]. The reported sample which present the closet chemical composition to our alloy is the $Co_{86}Tb_{14}$[123]. The thermalization time of

Tb in this alloy (τ_M = 500 fs) is, however, slower than what we found for $Co_{88}Tb_{12}$ ($\tau_{M=}$ 220 fs). One should note that the two alloys $Co_{86}Tb_{14}$ and $Co_{88}Tb_{12}$ are considered Co rich samples[69] which implies that demagnetization dynamics must almost similar for the both alloys. On the other hand, we note that Lopez *et al* [123] investigated the demagnetization dynamics of the 4f localized electron by probing directly the M_5 edge (~1240 eV) while in our measurement we probe the O_1 edge (~45 eV) corresponding to the excitation of 5s electrons. Meanwhile, for Rare Earth elements, the exchange interaction produces a large spin polarization of the 5s-5p shells which lie spatially outside the 4f shell [133]. This helps to explain the demagnetization dynamics observed in our experiment and open the question about different dynamics depending on the probing energy.

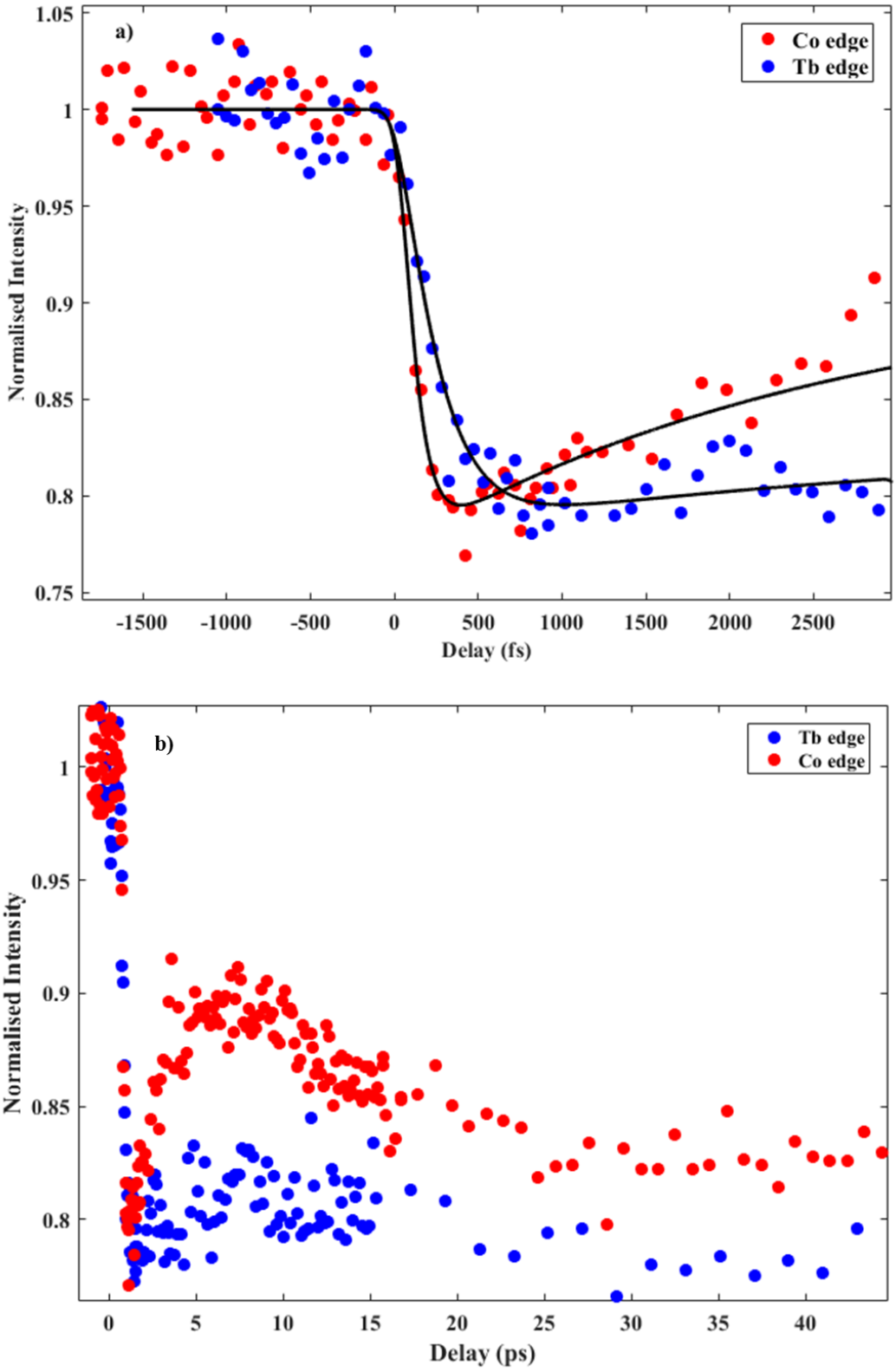

Figure 4-5: a) Ultrafast dynamics of Co M_3 (red symbols) and Tb O_1 (blue symbols) for the Co.88Tb.12 alloy. The best fit is obtained for $\tau_M = 110$ fs at the Co edge and for $\tau_M = 220$ fs at the Tb edge. b) Long delays showing that the Tb doesn't recover even after 40 ps.

4.4.3 Evolution of the intensity of first and third scattering order

The primary motivation for this experiment was to probe for the existence of ultrafast changes in the magnetic domain structure. In a previous experiment Pfau *et al* [9] investigated the time evolution of the magnetic scattering pattern of a thin Co/Pt multilayer film, which exhibits a lateral labyrinth domain pattern. It was observed that for high pump fluence the center of mass of the scattering ring moves to smaller q. These authors interpreted this observation as evidence for the occurrence of an ultrafast spatial modification of the domain wall structure. To motivate this interpretation, the authors proposed that a spin dependent super diffusive transport of the excited electrons exists. The difference in the propagation speed of the majority and minority electron (see section 1.4.2) leads to accumulation of minority electrons in the respective areas of the magnetic domain walls. This causes a broadening of the domain wall. In a more recent experiment Sant *et al* [10] probed the optically excited domain structure of a Co/Pd thin film using XUV diffraction in grazing incidence. They showed that their data also indicate the presence of a broadening of the domain walls caused by diffusion of majority spins into the domain area of opposite magnetization. Close to the domain wall, this may even lead to a spatially confined, transient ultrafast magnetization reversal.

To obtain a more direct proof of the existence of this domain wall broadening, we decided to determine the intensity ratio of the third and first scattering order. This ratio is inversely proportional to the domain wall width as we will show later in section 4.4.5. To realize this experiment, we chose a sample presenting a network of stripe domains with opposite magnetization direction. As discussed previously, this domain structure will act as a diffraction grating allowing different scattering orders to be detected. In the following we will discuss the temporal evolution of the first and third scattering order as well the ratio between these two orders. These scattering intensities were measured at the Co M_3 edge and for the highest pump fluence of F = 8 mJ.cm^{-2} which we could reach in our experiment. We remark already here that for such low pump fluence values, Pfau *et al* [9]did not observe any indication for domain wall broadening.

In Figure 4-6.a) we show the scattering intensity of the first and third order as a function of a short pump-probe time delay. The data show clearly that the two orders behave in the same way where an ultrafast intensity drop is followed by partial recovery. In Figure 4-6.b) we present the ratio between the two orders. One can clearly see that for the shown delay range up to 3 ps the ratio does not exhibit any clear evolution, it appears within the noise as

constant. Together with the invariant of the peak position discussed below this indicates that there is no spatial modification of the magnetic domain structure within this time delay range.

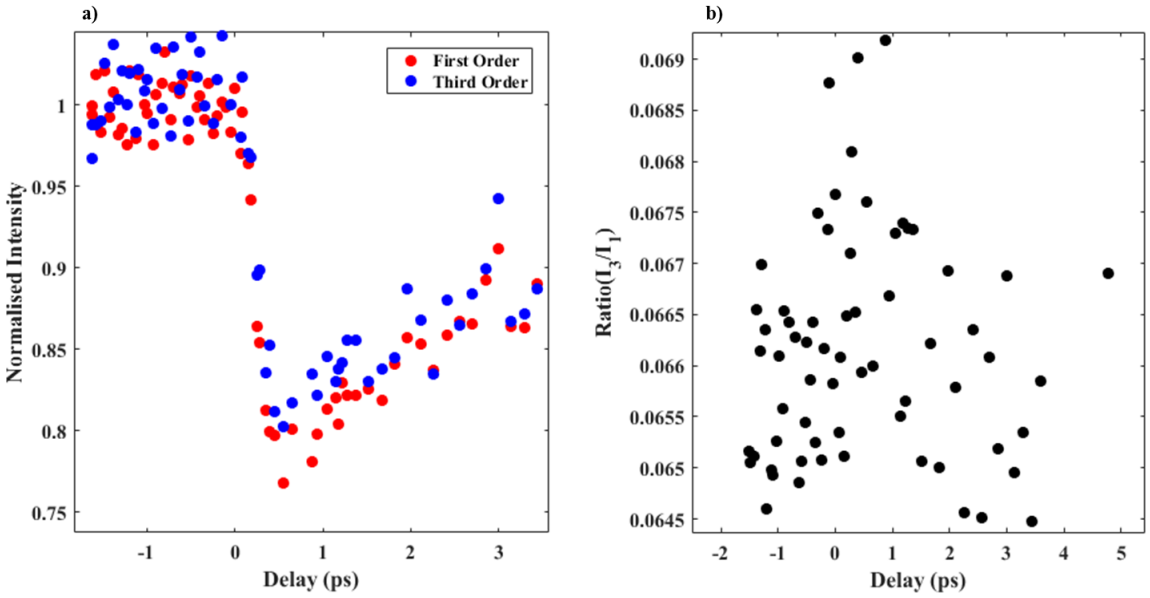

Figure 4-6: a) Ultrafast temporal evolution of the first (red) and third (blue) scattering order . These values are obtained after integrating azimuthally the positive and negative regions indicated in Figure 4-2.b) for each time delay. b) Intensity ratio of the 3rd and 1st scattering order as function of pump-probe time delay.

In order to verify that there is no general change of the magnetic domain structure, we precede our analysis relying on the same method used in [9]. We investigated the relative change $\Delta q_{peak}/q_{peak}$ of the SAXS distribution's modal value as a function of the time delay. In Figure 4-7.a), we plotted the normalized radial scattering intensity as a function of the magnitude of the momentum transfer q for unpumped and pumped delays. By comparing the unpumped (blue) and pumped (green) spectra, one can see that there is no shift of the peak position at q_{peak}. The black and red solid lines represent the fit of two spectra using a polynomial equation, to be used here just as a guide to the eye. In the Figure 4-7.b), we represent the relative change $\Delta q_{peak}/q_{peak}$ of the radial integration as function of pump-probe time delay. We observe that the difference in the SAXS distribution's modal value is negligible (0.12 %) and without any systematic evolution. We therefore conclude that the pump doesn't have any effect on the modal value q_{peak}, indicating that there are no changes in the domains structure during the first picoseconds. As mentioned above this observation is in line with the previous study of Pfau *et al* [9], who did not observe either any significant peak shift for such a low pump fluence [9].

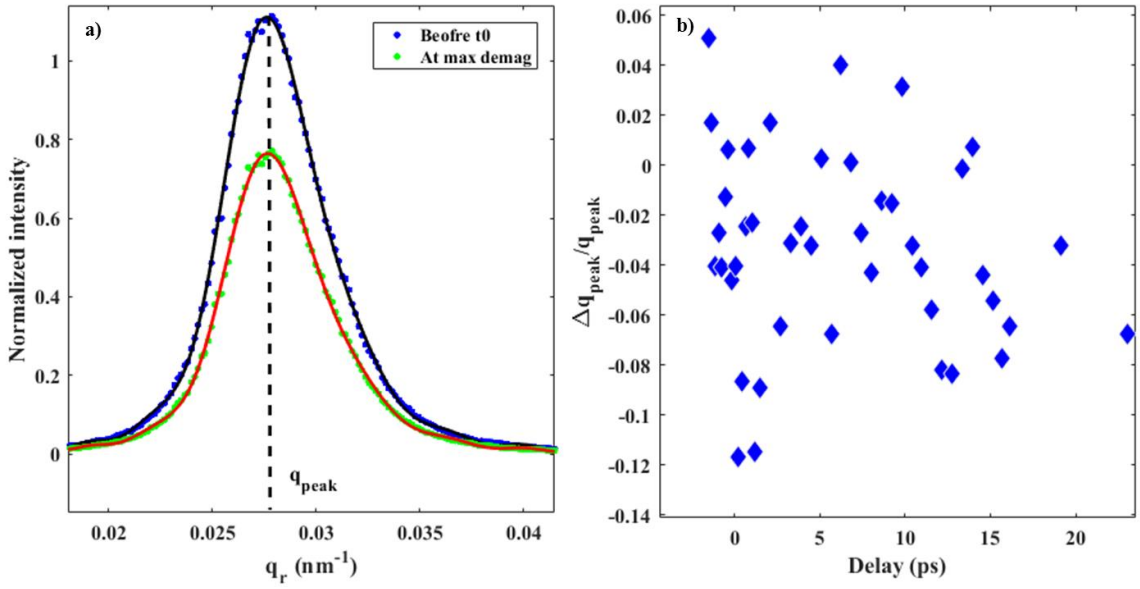

Figure 4-7: a) Radial scattering intensity of the SAXS distribution (first order) for negative delay (t<t0 in blue) and for positive delay (t~0.5 ps in green). The solid lines show the fit for the two spectra and used here as a guide to the eye. Clearly, we can observe a decrease of the intensity after pump meanwhile we can't observe any shift in the peak position. b) $\Delta q_{peak}/q_{peak}$ modal value as a function of the pump-probe delay. This data is the average of each three points. The variation of the q peak in time delay is almost negligible.

We next look at longer time delays beyond 3 ps. These data are shown in Figure 4-8.a). It is evident that on these longer time scales the first and third scattering order exhibit distinctly different dynamics. After the partial recovery of the intensity in the two orders, the intensity of the 1st order decreases slightly over a long time period. The intensity of the 3rd order, on the other hand, exhibits a sharp drop. This dissimilarity between the two orders on the time scale of a few to tens of ps has not been observed before. We can exclude as origin of this angular momentum transport by the of spin polarized hot electrons [4], because this would manifest itself on the sub-picosecond timescale when hot electrons are present, i.e., prior to thermalization.

We plot in Figure 4-8 b) the ratio between the two orders as a function of time delay which is obtained by dividing the intensity of the 3rd order by that of the 1st order. As we will show later in section 4.4.5.1, this ratio is linked to the domain wall width. We can therefore interpret this variation of the ratio as a modification of the domain wall width. To summarize, we saw above that during the first picoseconds after pumping this ratio is constant, which indicates that the domain wall width does not change. After about 4 ps, however, the ratio starts to decrease significantly, reaching its minimum value after about 20 ps, which indicates a broadening of the domain wall width during this time period.

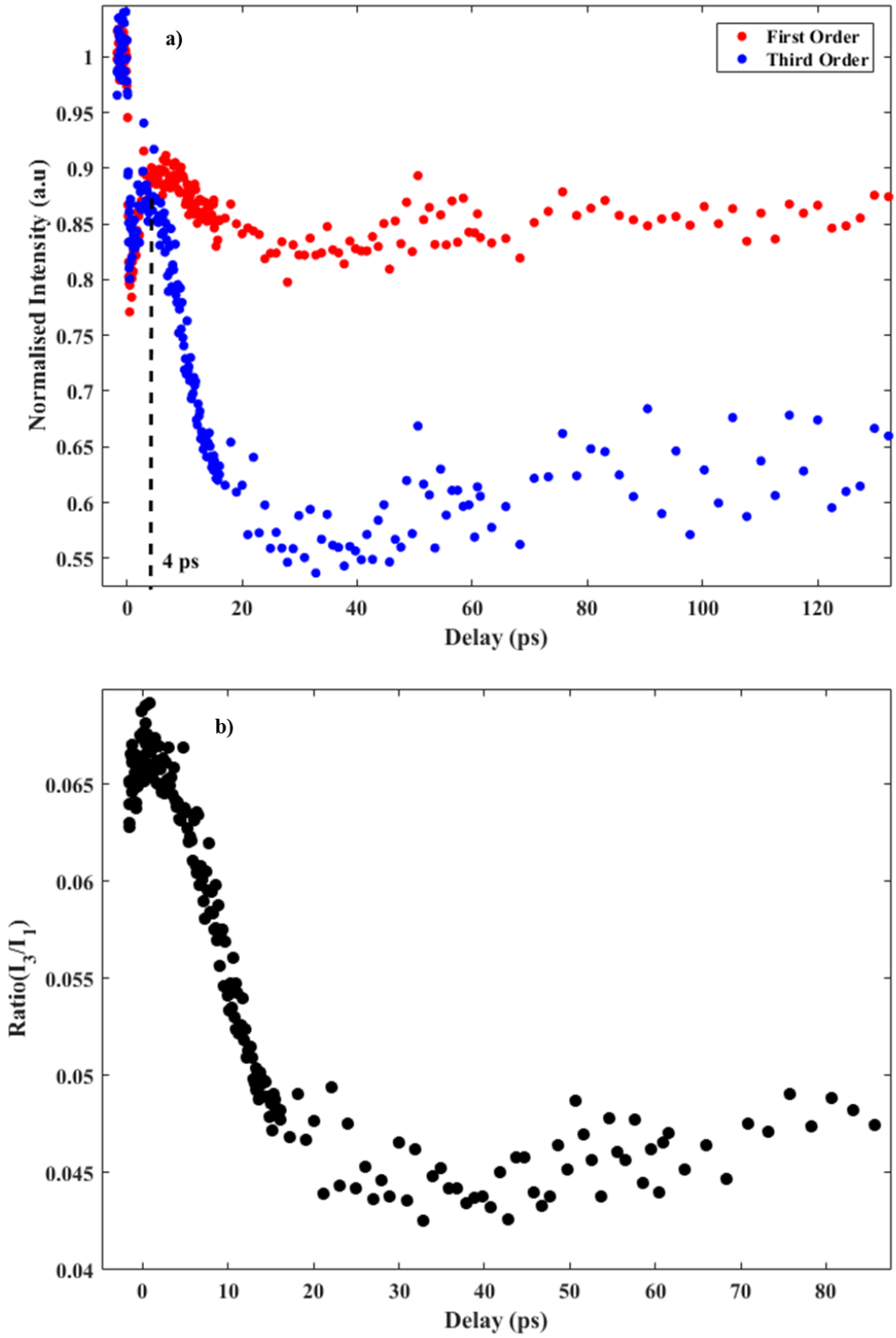

Figure 4-8: a) Intensity of the first and third scattering order as a function of pump-probe time delay. The vertical dashed line indicates the onset of the drop of the third order intensity. b) $3^{rd}/1^{st}$ scattering intensity ratio as function of the time delay.

4.4.4 Deriving the domain wall size from a scattering pattern

In order to quantify this variation of the domain wall width, we have to derive the size of the domain wall for each pump probe time delay. To do this we will consider two different methods. In the following we will introduce these two models and we will present the temporal evolution of the domain wall width as derived and quantified by these models. At the end, we will discuss the difference between these models by indicating which model is better applicable to the case of our measurement.

4.4.4.1 Model developed by Hellwig *et al.* [71]

In a previous experiment Hellwig *et al* [71] used magnetic X-ray scattering to investigate the stripe domain structure of Co/Pt-based multilayers exhibiting out of plane magnetization. The result of their measurement is reproduced in Figure 4-9. This shows the scattering intensity obtained from the two different domains systems, aligned stripe domains (open points) and labyrinth domains (closed points). For the aligned stripe domain system, the high degree of order permits to clearly observe the 1^{st}, 3^{rd} and 5^{th} scattering order. To interpret the data and to derive in addition to the domain size also information about the domain wall width, Hellwig *et al.* [71] developed a model to reproduce the recorded scattering profile. The quality of this modeling is underlined by the high accuracy with which this model, shown by the solid line, reproduces the experimental data.

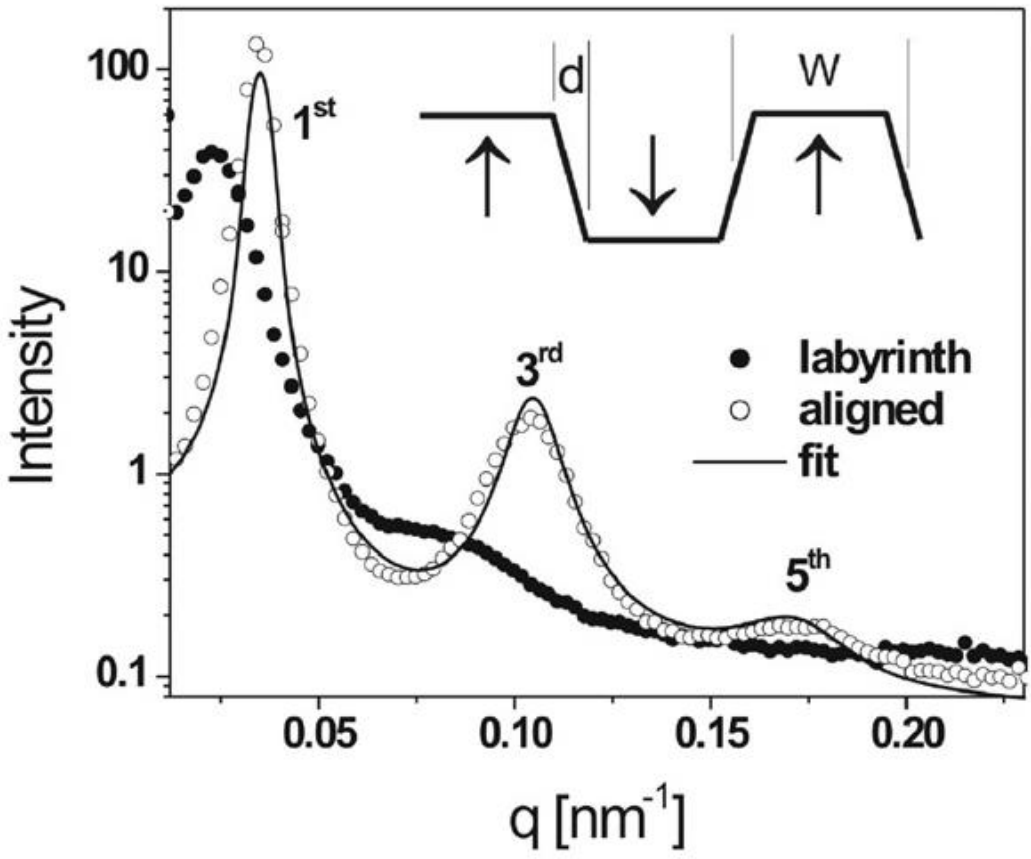

Figure 4-9: Radial intensity of the resonant magnetic scattering pattern of a Co/Pt multilayer reproduced from [71]. Open symbols represent the scattering pattern recorded for a stripe alignment of the magnetic domains, which exhibits significant higher order scattering due to the present high degree of order. The closed symbols show the scattering intensity detected for a labyrinth like domain pattern. The solid line is a fit of the developed model to the stripe domain state which allows extracting the two parameters d and w of the one-dimensional real space profile of the magnetic domain pattern shown in the figure inset.

One notes that this model implements Gaussian fluctuations of the domain size to take into account spatial disorder of the periodic lattice. Also, the out-of-plane component of the magnetization within the domain wall is assumed to vary linearly throughout the wall. We note that this is only a crude approximation of the variation within the present Bloch domain wall, where the magnetization turns like a screw (see section 1.2.4).

In the following we will present the model developed by Hellwig [71] and then apply it to the analyses of our scattering data.

Based on kinematical approximation, this model assumes that the expected scattering intensity for a stripe domain system with a periodicity D is given by:

$$S(qx) = |F|2 \frac{1 - exp(iq_x ND)}{1 - exp(iq_x D)} \qquad 4.3$$

with D representing the periodicity. To take into account fluctuations in the domain periodicity, the authors introduced disorder in this model by using the approach developed by Hendricks and Teller [134]. By averaging the intensity of all possible sequences of different domain thicknesses the scattering intensity can be written as:

$$\mathrm{F} = \int_0^D M_z(x)\exp(iq_x x)\ dx \qquad 4.4$$

with D representing the periodicity. To take into account the fluctuation in the domain periodicity, the authors introduced disorder in this model by using the approach developed by Hendricks and Teller [134]. By averaging the intensity of all possible sequences of different domain thicknesses the scattering intensity can be written as:

$$S^{int}(q_x) = <|\sum_N^n F_n \exp(iq_x \sum D_n)|^2> \qquad 4.5$$

with F_n and D_n the structure factor and domain period of the nth period, respectively. Under the assumption that each layer is statistically independent, the fluctuations of the average domain structure are considered cumulative. This model explicitly includes the inter-domain effect of the disorder [135], i.e., the phase error in one layer perturbs all subsequent layers. Expression (4.5) can be divided into two main parts:

$$S^{int}(q_z) = N < F * F > +2real(< F > \frac{\Phi\Psi}{T}) \qquad 4.6$$

with <F*F> and <F> the ensemble average over all possible scattering amplitudes and intensities from individual domain periods. The term that considers the interference of the scattering from different domains is given by:

$\mathrm{T}=<\exp(iq_zD)>$, $\Phi=<\exp(iq_zD)\ F^*>$ and $\Psi=\frac{N-N(N+1)T+T^{N+1}}{(1-T)^2}-N$

In order to be able to fit the data, the authors simplify these expressions by using a unit cell of a pair of an up and a down domain. Details about this are given in the appendix of their publication [71]. The final parameters to be fitted to the data are the domain periodicity, the domain wall width and the root mean square of the domain width fluctuation. Analyzing the development of this model in detail we noticed a mistake in their equations, which was preventing us from fitting successfully our experimental data by this model.

Expression (A.7) which gives the scattering amplitude for one domain F_A reads in their manuscript:

$$\mathrm{F_A}(q_x)=\int_0^d \left(-M+\frac{2Mx}{D}\right)\exp(iq_x x)\ dx + \int_d^{w_A} M\exp(iq_x x)\ dx$$

$$=\left(\frac{2Mx}{dq_x^2}\right)(\exp(iq_x w_A)-1)-(\frac{iM}{q_x})(\exp(iq_x w_A)+1) \qquad 4.7$$

with w_A the domain width, q the momentum transfer and d the domain wall width. The second line, however, contains a (probably typographic) error, since the integration of the first term should end at the boundary d and not w_A. The correct line should read:

$$\left(\frac{2Mx}{dq_x^2}\right) \qquad 4.8$$

One notices in Figure 4-10 that even with the incorrect expression of (A.7) we can easily fit the first scattering order, which explains why this model was widely used by others without that this typing error was noticed before. However, by looking at the inset of Figure 4-10one notices that the curve (red line) goes to negative values, which is an unphysical behavior and which prevents a correct fit of the higher scattering orders. A clear comparison of these models is shown by using the logarithmic scale in Figure 4-10.b). The additional peaks of the red curves represent the real part of a complex number.

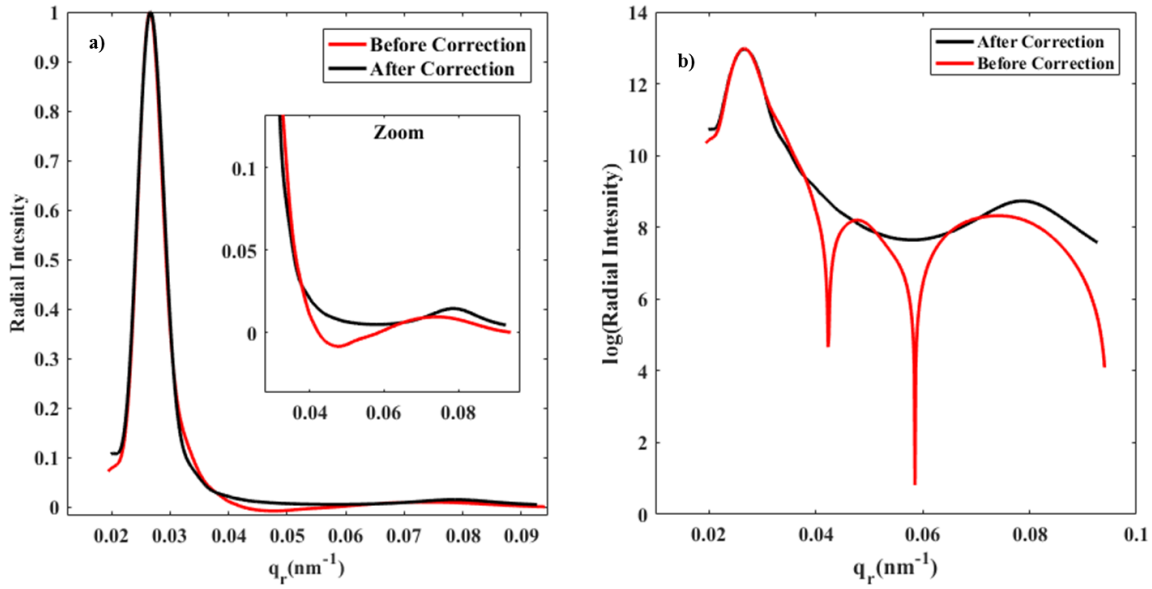

Figure 4-10: a) The initial and the corrected scattering model developed by Hellwig *et al* [71]. In the inset one can see that the red initial curve reach negative value which is unphysical and prevents to fit higher scattering orders. b) Logarithmic scale of the two curves presented in a).

4.4.4.2 Domain wall width as function of pump probe time delay

In order to find the domain wall width for each time delay, we fitted the radial profiles of the scattering patterns for each time delay using the corrected model developed by Hellwig *et al* [71]. This model yields three parameters which characterize the domain periodicity, the domain wall width and the root mean square of the domain size fluctuations, respectively. In Figure 4-11.a) we present the radial integral as a function of the momentum transfer for $t < t_0$.

We find a narrow maximum of the radial intensity at q_{peak}= 0.02676 nm^{-1}, which corresponds to a domain periodicity of D = $\frac{2\pi}{q_{peak}}$ = 244 nm $\pm$10 nm. The average domain width is D/2 which is equal to 122 nm $\pm$5 nm. MFM images of another $Co_{88}Tb_{12}$ film composition show a domain size of 105 nm (see Figure 2-8). Within the general uncertainties, these values are in reasonable agreement with the domain size found in our experiment. One notes also that the scattering value is statistically more relevant, since a larger area is studied, which may explain the slightly different values. The solid black line is the fit of the radial profile of the scattering pattern for negative delay i.e the un-pumped sample. One notices that the analytical expression reproduces well the experimental data of the first and third scattering order. Even when plotting the data on a logarithmic scale (Figure 4-11.b), one finds a remarkably good agreement. From the fit parameters, we obtained a value of 122 nm $\pm$5nm for the domain width (w_A in the expression) with a root mean-square fluctuation of 10 nm about the average domain width. The domain wall width is quantified to be 35 nm $\pm$ 2nm . As seen before in Figure 4-7.b) the peak position does not change, and in line with this we obtain a domain width of 122 nm $\pm$5nm for all pump probe time delays. For the domain wall width, on the other hand, we expect a variation, since the intensity ratio decreases as shown before in Figure 4-8.b). These values are plotted as a function of the pump probe delay in Figure 4-12. At the beginning the wall thickness is 35 nm. At about 4 ps, the wall width starts to expand up to about 43 nm. This is an increase by about 20%. We note that the onset of the domain wall broadening begins after the partial magnetization recovery and that it is reflected in the second drop of the intensity of the 3rd scattering order. The data thus show that the wall separating two opposite domains becomes larger and that this occurs at the expense of the domain width, i.e, the domain structure does not change. Before further interpreting this observation, we will confirm this interpretation using a model we developed ourselves.

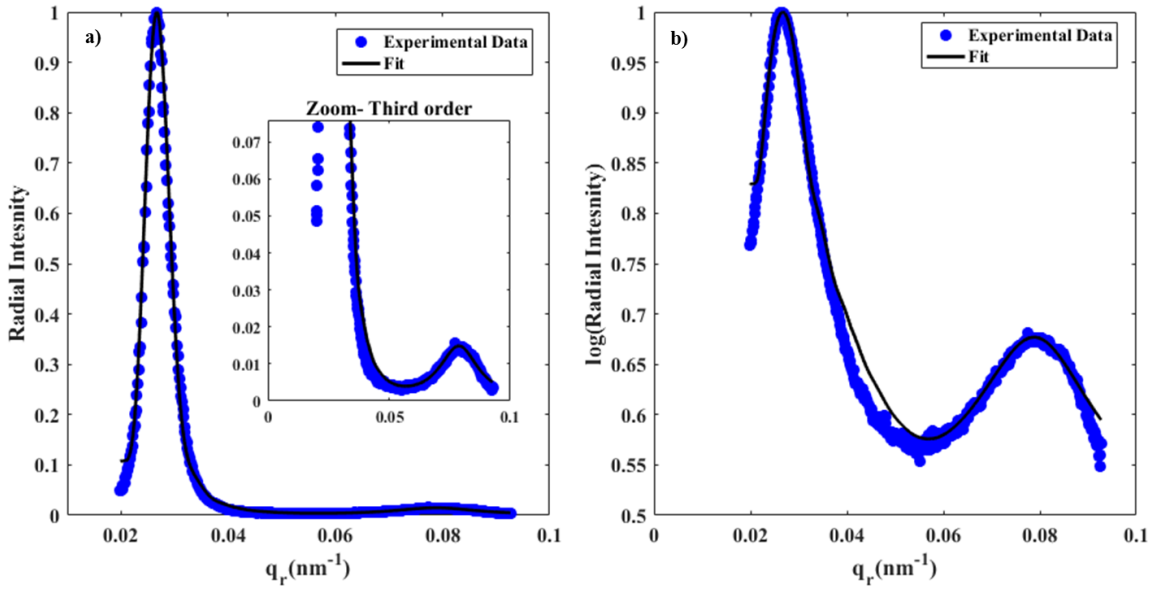

Figure 4-11: a) Radial intensity of the scattering profile pattern normalized by the maximum intensity value. The solid line represents the fit using expression developed in [71].In the inset a zoom of the third order. b) Logarithmic scaling of the curves shown in a).

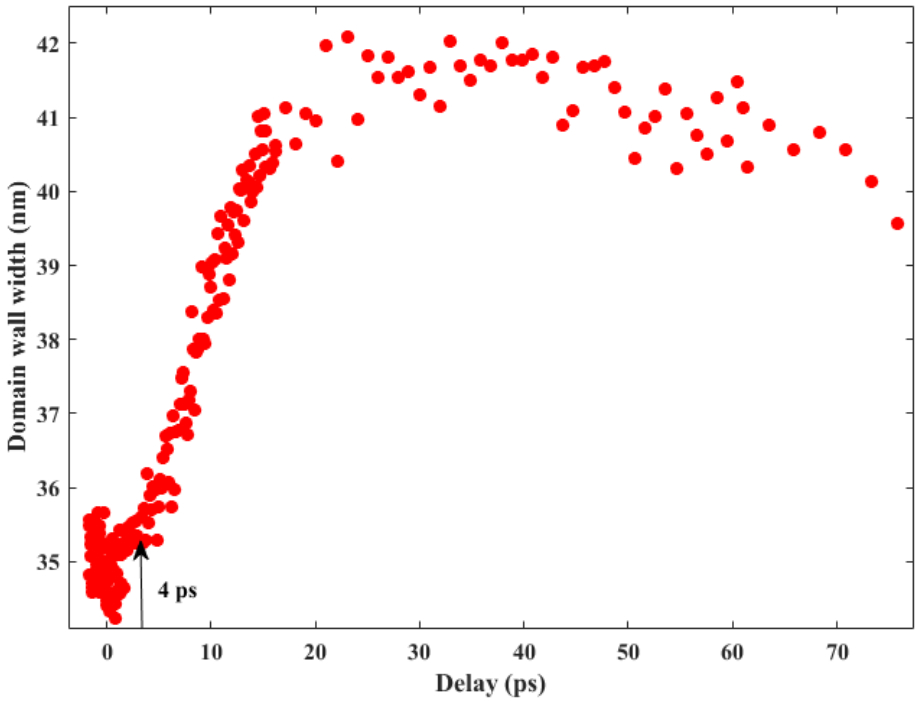

Figure 4-12: Domain wall width as a function of pump-probe delay. An expansion of the domain wall sets in after about 4 ps.

4.4.5 The Fourier analysis method of different scattering order

In this part we will present the model we developed ourselves to analyze the evolution of the intensities ratio of different scattering orders. We note that in this model we don't consider any fluctuation of the domain size, assuming that the obtained value is the average width of the probed domain walls. Like done by Hellwig *et al*. [71],we also consider a linear profile of the magnetization within the domain wall.

Our approach is based on the observation that any periodic signal can be represented as a sum of its frequency components by calculating the coefficient of the corresponding Fourier series, the k-th coefficient corresponds to the relative intensity of the k-th scattering order. Since our sample present a network of up and down domains separated by domain walls, we will develop here the Fourier series assuming that our sample presents a perfect trapezoidal network. An illustration of this one dimensional model is presented in figure 4-13.a). If we consider that $I \propto |t^2|$ denotes the intensity after transmission through the sample, this intensity is periodic in space and depends only on the real space variable x. The Fourier series representation of t is a trigonometric series given by:

$$t(x) = \sum_{k=-\infty}^{\infty} C_k exp(ikwx) \qquad 4.9$$

with k being the order coefficient, $w = \frac{2\pi}{L}$ with L the periodicity (see figure 4-13.a). The coefficient of order k is given by:

$$C_k = \frac{1}{L}\int_{-L_0}^{+L_0} t(x) exp(-ikwx)dx \qquad 4.10$$

The transmitted intensity depends on the refractive index, which in turn depends on the magnetization. Note that the reflectivity of X-rays for near normal incidence is negligible (~10^{-4} for 60 eV in general). If we represent the refractive index by $n=1-(\delta_0 + \delta_1 * M(x)) + i(\beta_0 + \beta_1 * M(x))$ we can write :

$$t(x) \propto \exp(ikTn(x)) = \exp(ikT(1 - \delta_0 + i\beta_0)) * \exp(ikT(-\delta_1 + i\beta_1)M(x)) \qquad 4.11$$

where T is the sample thickness, k the wave vector and M(x) is the spatially varying magnetization. Since δ_1 and β_1 are small, we can perform the Taylor expansion on the second exponential and t(x) becomes:

$$t(x) \propto t0\,(1 + (-ikT\delta_1 - kT\beta_1)\,M(x)) = t0 + t1\,M(x) \qquad 4.12$$

With $t0 = \exp(ikT(1-\delta_0 + i\beta_0))$ and $t1 = (-ikT\delta_1 - kT\beta_1)$.

To calculate the Fourier coefficients we therefore have to find the expression of M(x). For this we need the periodicity, the domain wall width and M_0, the magnetization within the domain. This can be done by considering that the shape of the trapezoid can be represented as the difference between the two triangles shown in figure 4-13.b). To take into account the positive and negative values of the magnetization, we subtract a rectangular function from M_0. With this M(x) can be written as:

$$M(x)=M_1 * \wedge \left(\frac{2x}{L_1}\right) - M_2 * \wedge \left(\frac{2x}{L_2}\right) - M_0 \mathrm{rect}\left(\frac{x}{2L_0}\right) \quad 4.13$$

with M_1 the magnetization (or the height) of the big triangle, M_2 corresponds to the magnetization of the small triangle, $\wedge$ the triangular function that is discussed later (see figure 4-13.c), L_1 the width of the big triangle,L_2 the base width of the small triangle and rect the rectangular function.

Comparing the illustrations in figure 4-13.a) and b), one notices that the big triangle represents one domain with its left and right domain walls while the base of the small triangle represents the width of the domain without its domain walls. For this reasons L_1 and L_2 can be expressed in function of the domain periodicity and the domain wall width as follow:

$$L1 = \frac{L}{2} + d = L0 + d \quad 4.14$$

$$L2 = \frac{L}{2} - d = L0 - d \quad 4.15$$

We can express M_1 and M_2 as a function of M_0 by comparing the tangent of angle θ of the two triangles presented in the figure 4-13.a):

$$\tan(\theta) = \frac{\frac{d}{2}}{M_0} = \frac{\frac{L_1}{2}}{M_1}$$

Therefore

$$M1 = M0\left(\frac{L_1}{d}\right) = M0\left(\frac{L_0}{d} + 1\right) = M0\left(\frac{L}{2d} + 1\right) \quad 4.16$$

In the same way one finds:

$$M2 = M0\left(\frac{L_2}{d}\right) = M0\left(\frac{L_0}{d} - 1\right) = M0\left(\frac{L}{2d} - 1\right) \quad 4.17$$

Substituting M(x) in equation (4.13), t(x) is now expressed as:

$$t(x) = (t0 - t1M0)\,\mathrm{rect}\left(\frac{x}{2L_0}\right) + t1\left(M1 * \wedge \left(\frac{2x}{L_1}\right) - M2 * \wedge \left(\frac{2x}{L_2}\right)\right) \quad 4.18$$

In order to avoid complex equations, we will develop the integral of the triangular function ∧(x) before replacing each term by its corresponding values in the equation (4.18). An illustration of this function is given in figure 4-13.c), which can be written as:

$$\wedge(x)=\begin{cases}1+x for -1<x<0\\ 1-x for 0<x<+1\end{cases}$$

The integral of this function is given by:

$$\text{Int}=\int_{-1}^{0}(1+x)\exp(-i*2\pi kx)\,dx+\int_{0}^{1}(1-x)\exp(-i*2\pi kx)\,dx$$

$$\text{Int}=\left[\frac{-\exp(-i*2\pi kx)}{i*2\pi k}\right]_{-1}^{0}+\left[\frac{-x\exp(-i*2\pi kx)}{i*2\pi k}\right]_{-1}^{0}+\left[\frac{\exp(-i*2\pi kx)}{(i*2\pi k)^2}\right]_{-1}^{0}+\left[\frac{-\exp(-i*2\pi kx)}{i*2\pi k}\right]_{0}^{1}-\left[\frac{-x\exp(-i*2\pi kx)}{i*2\pi k}\right]_{0}^{1}-\left[\frac{\exp(-i*2\pi kx)}{(i*2\pi k)^2}\right]_{0}^{1}$$

Developing these terms we find:

$$\text{Int}=\frac{2(1-\cos(2\pi k)}{-4(\pi k)^2}=\frac{sin^2(\pi k)}{(\pi k)^2}=sinc^2(k) \qquad 4.19$$

The coefficient of the k-th scattering order can therefore be written as:

$$\text{Ck}=\frac{1}{L}\int_{-L_0}^{+L_0}t(x)\exp\left(\frac{-i2\pi kwx}{2L0}\right)dx=\frac{1}{2L0}F\{t(x)\}_{F_x} \qquad 4.20$$

with $F_x=\frac{kx}{2L_0}$

Using equations (4.18) and (4.20) we obtain:

$$C_k=\frac{2L_0}{2L_0}(t_0-t_1M_0)sinc(2L_0F_x)+\frac{t1}{2L_0}\left(\frac{M_1L_1}{2}sinc^2\left(\frac{L_1F_x}{2}\right)-\frac{M_2L_2}{2}sinc^2\left(\frac{L_2F_x}{2}\right)\right)$$

Replacing M1, L1, L2 and F_x by their values using equations (4.16) and (4.17) we obtain:

$$C_k=(t_0-t_1M_0)sinc(k)+\frac{4t_1M_0\eta_0}{\pi^2k^2}sin\left(\frac{k\pi}{2}\right)sin\left(\frac{k\pi}{2\eta_0}\right) \qquad 4.21$$

with $\eta_0=\frac{L_0}{d}$, which represents the domain width divided by the domain wall width. Note that the first term is zero for k equal to any real integer.

To test the validity of our model, we look at the case of $\eta_0=1$ which means that L_0 = d the network is triangular and C_k simplifies to:

$$C_k = \frac{4t_1 M_0}{\pi^2 k^2} sin^2\left(\frac{k\pi}{2}\right) \quad 4.22$$

Using the trigonometric relation that $\sin^2(a)=\frac{1-cos(2a)}{2}$ then C_k can be expressed as:

$$C_k = \frac{2t_1 M_0}{\pi^2 k^2}(1 - \cos(k\pi)) \quad 4.23$$

This value of C_k is consistent with the literature of a perfect triangular network and confirms the validity of the developed model.

Looking back at equation (4.21), we can calculate the coefficients of the first and third scattering orders which are given by:

$$\mathrm{C1} = \frac{4t_1 M_0 \eta_0}{\pi^2} sin\left(\frac{\pi}{2\eta_0}\right) \quad 4.24$$

$$\mathrm{C3} = \frac{4t_1 M_0 \eta_0}{9\pi^2} sin\left(\frac{3\pi}{2\eta_0}\right) \quad 4.25$$

The ratio of these two intensities follows as:

$$\mathrm{R} = \frac{I_3}{I_1} = \frac{|C_3|^2}{|C_1|^2} = \frac{sin^2\left(\frac{3\pi}{2\eta_0}\right)}{81 * sin^2\left(\frac{\pi}{2\eta_0}\right)} \quad 4.26$$

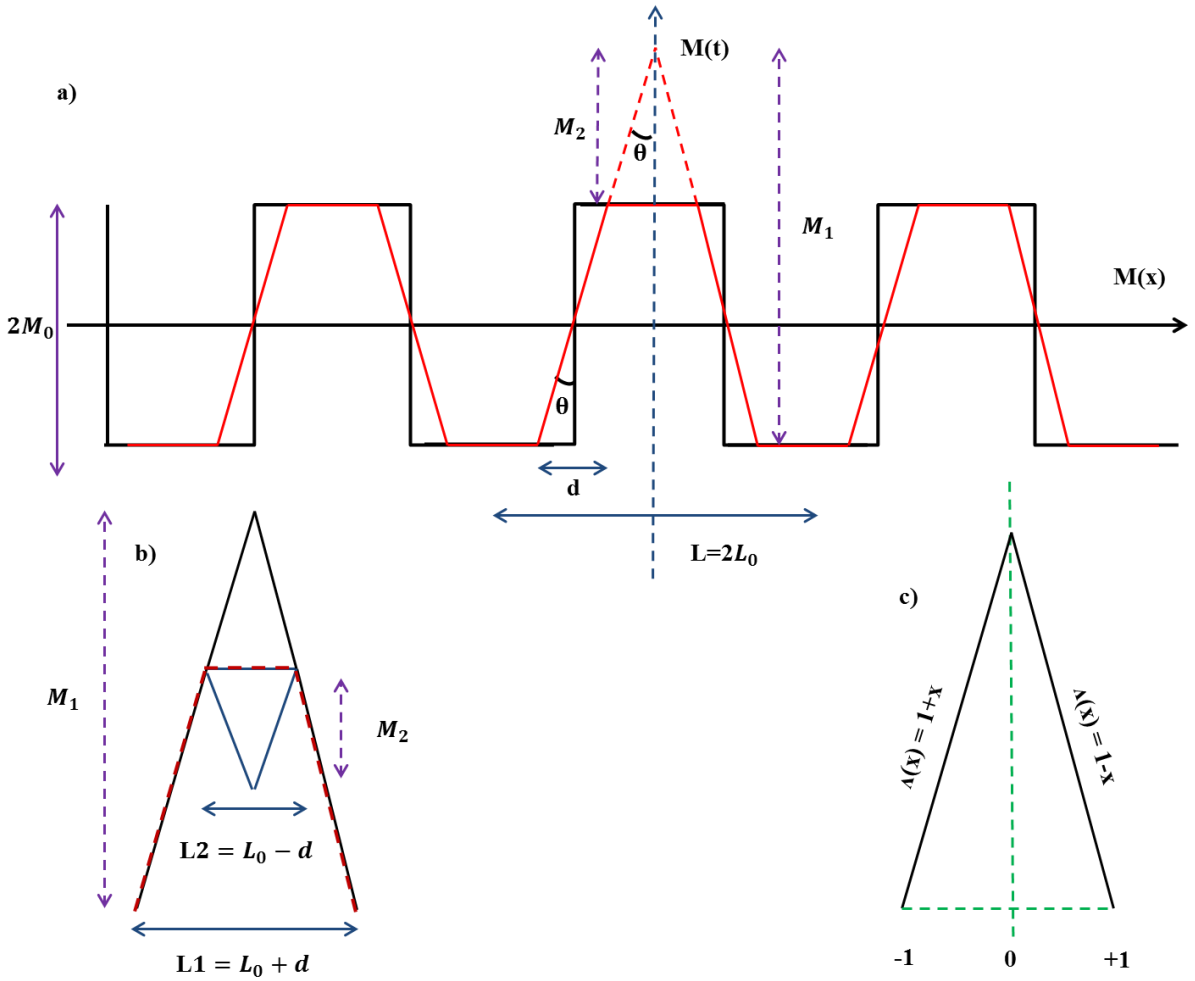

figure 4-13: a) Illustration of a series of isosceles trapezoids to represent the network of magnetic domains in our sample. L_0 is the half periodicity and represent the domain width while d is the domain wall width. b) Illustration of the trapezoid that can be obtained by subtracting the triangle in blue from the triangle in black. c) Illustration of the hat function (triangular function)

4.4.5.1 Determination of the domain wall width using the Fourier model

Using the model developed in section 4.4.5, we can determine the domain wall width for each pump-probe delay value. Replacing $\eta_0 = \frac{L_0}{d}$, equation (4.26) reads :

$$R = \frac{I_3}{I_1} = \frac{C_3^2}{C_1^2} = \frac{sin^2\left(\frac{3\pi d}{2L_0}\right)}{81 * sin^2\left(\frac{\pi}{2L_0}\right)} \qquad 4.27$$

We see in equation (4.27) that the ratio between the intensity of the third and first scattering order depends only on two parameters: the domain width and the domain wall width. From

Figure 4-7.a) showing the radial integral as function of momentum transfer, we can deduce that the domain periodicity $D = 2L_0 = (244 \pm 10)$ nm. In section 4.4.3 we show that there is no considerable modification of the peak position, which implies that the domain periodicity does not change as a function of pump probe delay. This leads to the conclusion that any variation of the ratio R is due to a change of the domain wall width.

The ratio can be calculated by dividing the intensity of the third order by that of the first order. Figure 4-7.b) shows the ratio between the two orders as a function of the pump probe delay. Using the values of L_0 and R, we can determine with equation (4.27) the wall width for each pump probe delay. These values are plotted in Figure 4-14. The initial wall thickness is 33 nm before t_0. Wall expansion starts at about 4 ps reaching a final value of 42 nm. The broadening of the domain wall begins after the partial recovery of the magnetization at the moment of the onset of the second drop of the intensity of the 3rd scattering order.

Comparing the results of the two models developed in section 4.4.4.2 and section 4.4.5.1 we notice a very close agreement. Using the Hellwig model we extract an expansion of the domain wall from 35 nm to 43 nm while this Fourier analysis method propose a domain wall broadening from 33 nm to 42 nm. This similar value between the two models gives confidence in the respective approximation considered in our developed model. The difference in the initial wall width values could be due to the absence of fluctuations in our Fourier analysis method, while these were taken into consideration in the model of Hellwig *et al*[71]

In the following discussion we will use the domain wall width values derived with the model of Hellwig *et al*[71] since these takes the presence of width fluctuations into account.

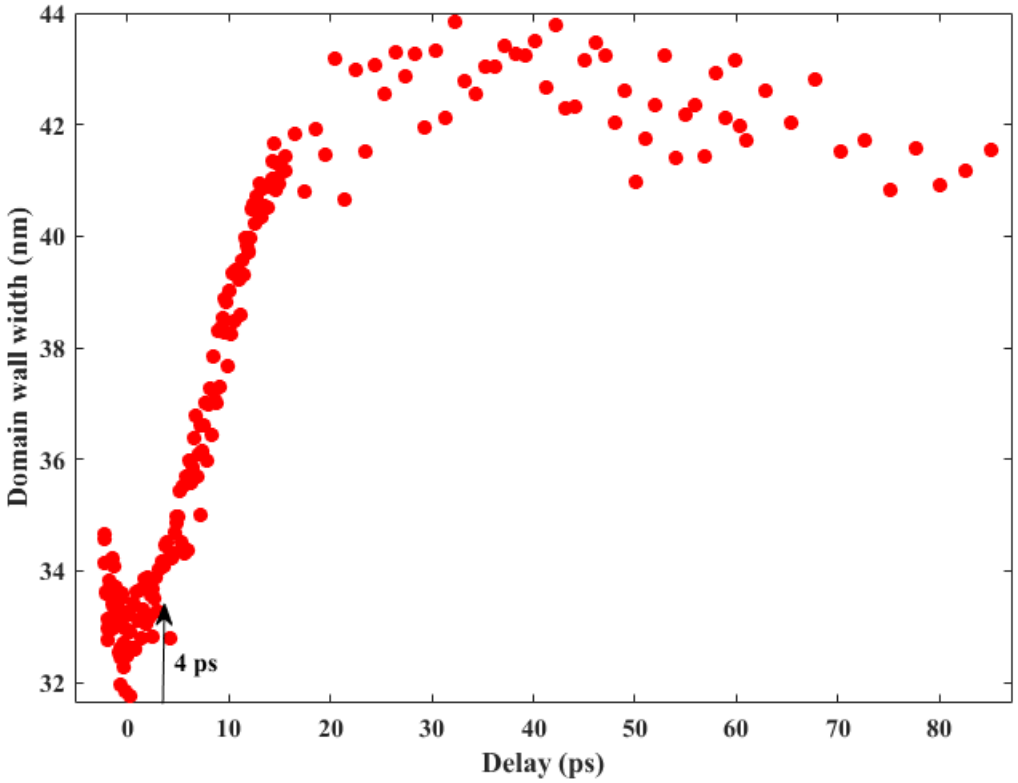

Figure 4-14: Domain wall width as a function of pump-probe delay. These values are obtained by applying the method developed in section 4.4.5. An expansion of the domain wall sets in after a pump-probe delay of about 4 ps.

4.4.6 Determination of the uniaxial anisotropy K_u

We discussed in section 1.2.4 that for the most general case of a 180° Bloch wall, the domain wall width of a magnetic thin film is given by [136], [137]:

$$\delta = \pi \sqrt{\frac{A_{ex}}{K_u}} \qquad 4.28$$

with A_{ex} the exchange stiffness of the material and K_u the uniaxial anisotropy. This relationship opens up the possibility to link the observed change in the domain wall width with a variation of the uniaxial out of plane anisotropy of our CoTb film. The reason for this is that we can suppose that on the timescale of a few picoseconds after excitation, the exchange stiffness is constant. On one hand one may argue that the exchange stiffness depends on the exchange coupling between neighboring atoms. Hence, any variation in A_{ex}

should take place on the timescale of the exchange interaction, which is sub-fs. On the other hand, the exchange stiffness depends also on the interatomic distance as one can see in equation (4.29). Now if we consider that the broadening of the domain wall is due to the variation of A_{ex}, then the interatomic distance should decrease leading to an increase of the exchange stiffness value. This seems, however counter intuitive, since with increasing temperature the interatomic distance generally increases. Note that in a recent experiment, E. Jal *et al* [138] observed that laser induced demagnetization dynamics in a thin Ni film is indeed accompanied on the picosecond time scale by a film thickness increase. However, even in the employed case of strong pumping, this thickness increase was less than about 1%. For these reasons, we assume in the following that the exchange stiffness can be considered to be essentially constant on the picosecond time scale in our measurements.

As one can see in the equation (4.28) δ and K_u are inversely proportional. This implies that an increase of the domain wall width indicates a reduction of the uniaxial anisotropy K_u. To quantify K_u as a function of the pump probe delay, we need to obtain an initial value of K_u for $t < t_0$ where the system is not pumped. In section 2.2.2 we showed that the magnetic anisotropy can be determined, if the anisotropy field H_A and the saturation magnetization M_S are known (see equation 2.2). The anisotropy field is the magnetic field needed to overcome the coupling of the magnetization to the crystal lattice. Thus, H_A is the external magnetic field needed to turn the magnetization from out plane to in plane direction, or inversely[69]. However for samples having small magnetic moments, as out CoTb samples, it is difficult to decide whether the magnetization is saturated or not [69]. This introduces a great uncertainty about the value of the anisotropy field[69]. Since our sample presents an out plane magnetization, we measured a static in plane SQUID-VSM of the CoTb sample to determine the uniaxial anisotropy. The hysteresis loop of the magnetization as function of the applied external field obtained from this measurement is shown in Figure 4-15. As one can see, in order to saturate the magnetization in the sample plane we need to apply an external field of $H_A = (1.5 \pm 0.5) \times 10^4$ Oe = $\frac{(1.5 \pm 0.5) x 10^7}{4\pi}$ A/m, which is also referred to as the anisotropy field. Furthermore, the value of the magnetic moment at saturation is $M_{sat} = (8 \pm 0.2) \times 10^{-4}$ emu. By dividing this value by the volume of the measured sample, we can determine the magnetization per unit volume which is equal to:

$$M_{sat}(\text{emu/cm}^3) = \frac{(8 \pm 0.2) * 10^{-4}}{0.5 * 0.5 * 50 * 10^{-7}} = 640 \pm 15 \text{ emu/cm}^3$$

Converting units (1 emu/cm^3 = 10^3 A/m) we obtain M_{sat}= (6.4± 0.15)*10^5 A/m. We remark that this value is consistent with the literature [69]. The incertitude of the anisotropy field H_A and the saturation magnetization leads to a large incertitude for the calculated uniaxial anisotropy. Using equation (2.2), we obtain the value of the uniaxial anisotropy K_u=737 ± 180 KJ/m^{-3}. We remark that once again this value is in close agreement with values reported for $Co_{88}Tb_{12}$ films in the literature [69]. Using equation (4.28) we can derive now the value of the exchange stiffness for our sample, which we find to be A_{ex} = (7.6± 2.2) x10^{-11} J/m^{-1}. We note that this value is of good order of magnitude. On the other hand, the obtained value of A_{ex} is 5 times greater than that reported in the literature[139]. Also by using an expression given by [140], one can approximates primitively the exchange stiffness value of $Co_{1-x}Tb_x$:

$$A = \frac{n_{11}J_{Tb-Tb}\bar{S}_1^2(1-x)^2}{a_{11}} + \frac{(n_{12}+n_{21})|J_{Tb-Co}|\bar{S}_1\bar{S}_2x(1-x)}{a_{12}} + \frac{n_{22}J_{Co-Co}\bar{S}_2^2x^2}{a_{11}} \qquad 4.29$$

where n_{ij} the number of the pairs per unit volume, J the corresponding exchange constant, $S_{i,j}$ the corresponding angular momentum value and x the concentration of Cobalt. According to [141], we can suggest that $n_{11}=n_{12}=n_{21}=n_{22}=2$. The exchange constant between the Tb, Fe and Co are given by [142] with:

- J_{Co_Tb}= -2.4*10^{-22} J
- J_{Tb_Tb}= 0.2*10^{-22} J
- J_{Co_Co}=(2.4-2.5*x_{Tb}) J for x_{Tb}=0.12 we then have J_{Co_Co}=2.1x10^{-22} J

The average angular momentum of Tb is S_{Tb}=5.05 [142] and that of Co is given by S_{Co}=0.775 – 0.848 $[\frac{x_{Tb}}{1-x_{Tb}}]^2$. Thus, for our $Co_{88}Tb_{12}$ sample S_{Co}=0.73. The interatomic distance are a_{11}=3.5 Å, a_{12}=3 Å, a_{22}=2.5 Å[69]. Replacing these values, we can calculate the exchange stiffness which is A_{ex} ~ 1x10^{-11} J/m. We can notice clearly that our extracted value of A_{ex} from equation (4.28) is not consistent with the calculated value.

This deviation from the literature could be due to the assumption of a linear domain wall profile in our model instead of a Bloch wall profile. This assumption approximates the FWHM of the domain wall into a larger area that considers the two wall borders. Subsequently, for smaller domain walls, one expects to find the actual value of A_{ex}.

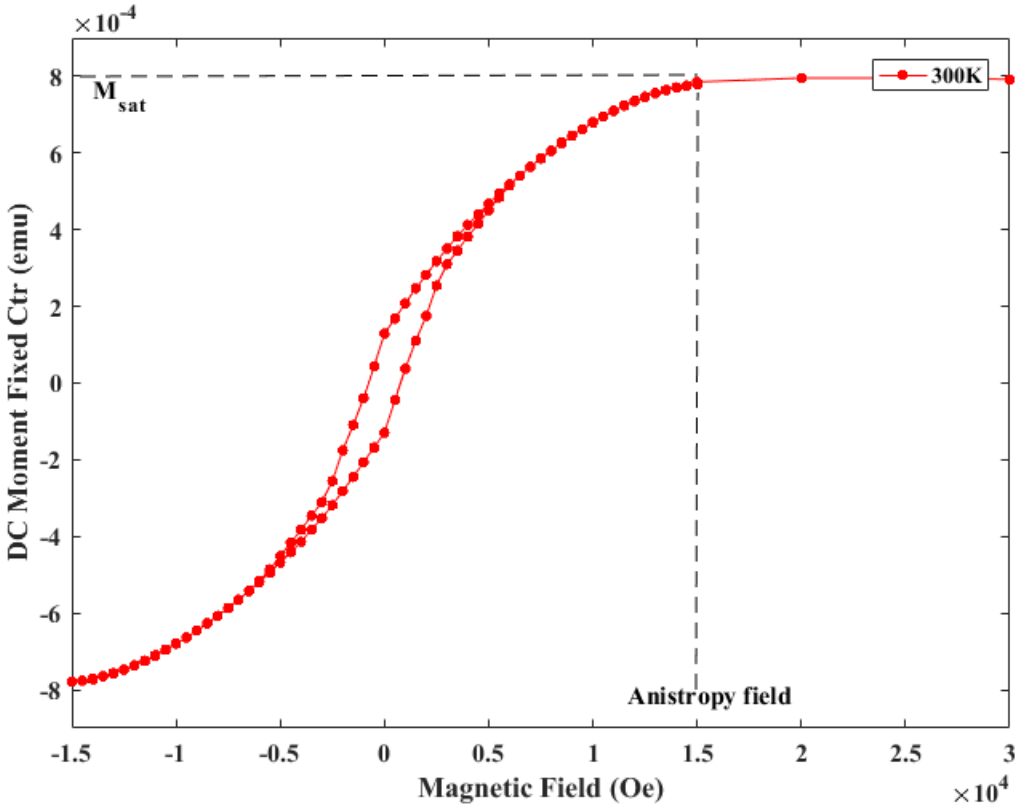

Figure 4-15: Hysteresis loop of the $Co_{88}Tb_{12}$ sample measured with SQUID-VSM with the magnetic field applied in the film plane. At saturation we find the M_{sat} = (8±0.2) x10^{-4}(emu) and the anisotropy field H_A= (1.5±0.5) x10^4 (Oe).

Supposing that A_{ex}= (7.6± 2.2) x10^{-11} J/m^{-1}, we can now employ equation (4.28) to determine the uniaxial anisotropy which is plotted in Figure 4-16 as a function of the pump probe delay. Not surprisingly, it exhibits the same dynamics. To obtain a quantitative description of the dynamics we use a simple exponential fit, which is shown by the solid line in the figure. From this fit we obtain that the onset of the drop start at 4 ± 0.5 ps and that the characteristic times scale of this drop is about 8 ps.

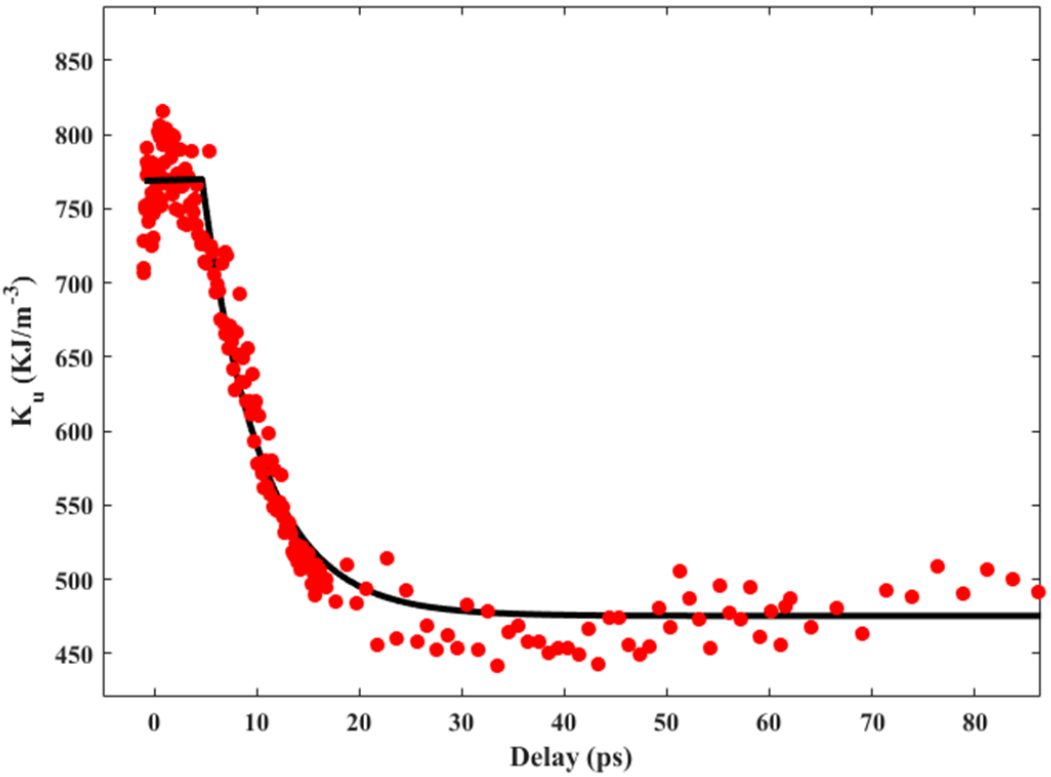

Figure 4-16: Uniaxial anisotropy as a function of pump-probe delay. These values are derived by using equation (4.28).The solid line represents a fit using an exponential function.

It is known for films with out of plane magnetization that with increasing temperature the magnetization tends to drop into the film plane[143]. This implies that the uniaxial anisotropy decreases with temperature. For this reason we interpret the observed decrease of K_u to be the consequence of an increase of the lattice temperature. We note that the time scale of an onset at about 4 ps after the initial excitation is in line with such an interpretation. At this point in time, the electron, spin and lattice degrees of freedom are typically close to reaching thermal equilibrium and thermally driven phenomena can be expected to occur.

As shown by equation (4.28), a drop of K_u leads to an expansion of the domain wall, i.e., an increase of its width. This broadening of the domain wall is detected via the change in the intensity ratio of the third and first scattering order. To test this interpretation linking the change in K_u to an increase in temperature, we performed in plane SQUID-VSM measurements as a function of sample temperature. The recorded hysteresis loops are shown in Figure 4-17.a). One notices that the anisotropy field decreases with increasing temperature.

This indicates a reduction of the uniaxial anisotropy K_u. The form of the hysteresis loop recorded at 600 K indicates that the magnetization lies within the film plane.

In Figure 4-17.b), we show the derived uniaxial anisotropy values as a function of sample temperature. By comparing the minimum value of the uniaxial anisotropy from Figure 4-16 with the values presented in Figure 4-17.b), we can quantify the lattice heating by the pump laser to be about ΔT = 160° K. To understand whether this temperature increase is realistic, we can estimate the transient temperature increase due to the energy deposited by the laser pulse. For this we use the formula [144]

$$\Delta T = \frac{F_c}{C * t} \tag{4.30}$$

thickness of the sample. To estimate the reflectivity of our sample we approximate the Co rich CoTb film as a pure Co film for which the reflectivity is known to be R = 0.7. The absorbed fluence is then Fc=(1-R) x F= 2.4 mJ/cm^{-2}. For the heat capacity we choose the heat capacity of cobalt which is C= 3.3*10^6 J/m^{3}K. Employing equation (4.30) we find that ΔT= 145° K for a film thickness of 50 nm. The close agreement between this crude estimate and the temperature increase obtained from the derived change in anisotropy supports our interpretation that the reduction of the anisotropy is due to thermal heating of the lattice.

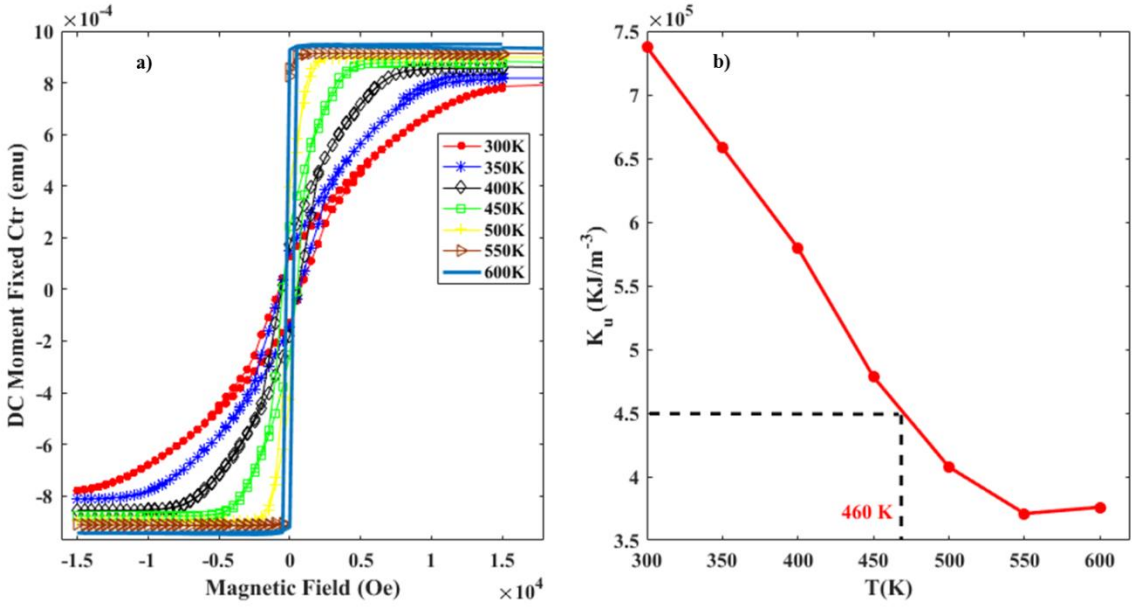

Figure 4-17: a) Hysteresis loop as a function of the heating temperature obtained by the SQUID-VSM measurements. Clearly, the applied field needed to saturate the magnetization of the film decreases for higher heating temperature. b) The uniaxial anisotropy as a function of the heating temperature. The dashed line present corresponds here to the minimum value of Ku in Figure 4-16 and indicates that the sample is heated up to160 K.

4.5 Ultrafast demagnetization of the Co/Pt multilayer

In order to investigate the role of hot electrons to the ultrafast demagnetization process, Vodundgbo *et al* [119] studied the magnetization dynamics of a Co/Pd multilayer capped by an Aluminum layer. In the same run they measured the ultrafast demagnetization of an uncapped Co/Pt multilayer using the resonant magnetic small angle scattering technique. The Infrared pump soft X-ray probe measurements were performed at the SXR instrument of the X-ray Free Electron laser LCLS. The investigated sample consisted of 20 repetitions of $[Co_{0.6nm}/Pt_{0.8nm}]$, and was prepared in order to present a network of opposite stripe domains (see section 2.3.2). When the X-ray photon energy is tuned to the absorption edges of Co or Pt, this domain structure will act as a diffraction grating and different localized scattering orders are obtained. At the Co L3 edge (778 eV), the high degree of domain alignment give rise to the positive and negative first, third and fifth scattering order as one can see in Figure 4-18. For the detection of the scattering, an in vacuum charge coupled device (CCD) detector was used.

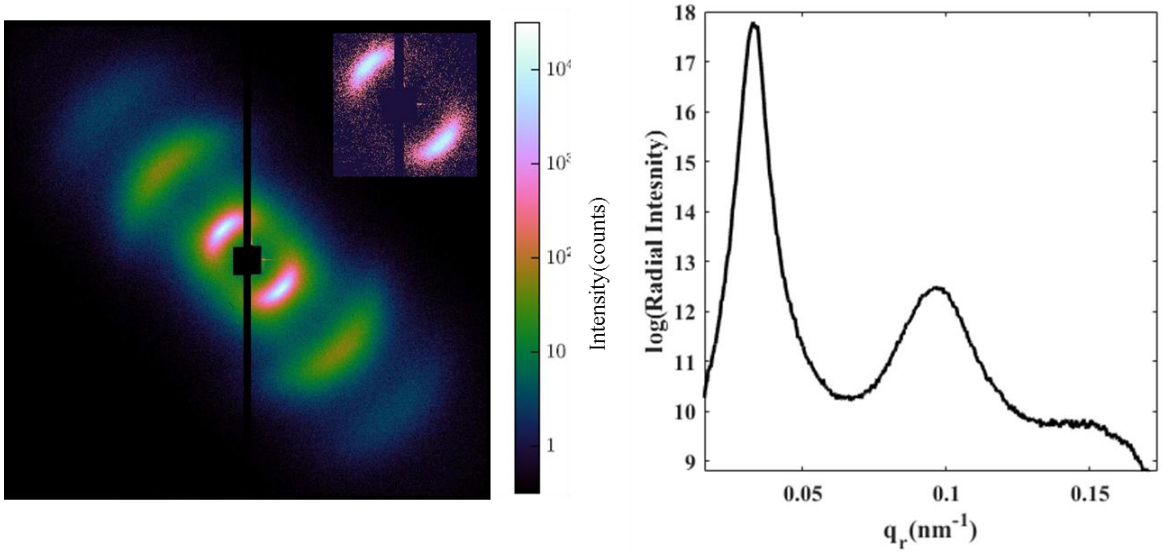

Figure 4-18: Resonant magnetic scattering pattern recorder at the Co L_3 absorption edge (778 eV). One can see the positive and negative first, third and fifth scattering order. b)Radial integral of the scattering pattern.

In this thesis, we will limit our analysis to the temporal evolution of the different scattering order as well the intensity ratio. This would help us to determine any ultrafast variation in the domain wall width of the Co/Pt thin film. Regarding data treatment, we proceeded using the same analysis method of the CoTb data (see section 4.3).

In Figure 4-19.a), we show the scattering intensity of the first and third scattering order as a function of the pump-probe time delay. We note that the two orders display the typical

ultrafast behavior where a drastic drop of the intensity occurs on a sub-picosecond time scale and a partial recovery takes place within tens of picoseconds. The ratio between the two orders dos not exhibit any clear evolution and it is almost constant (see Figure 4-19.b). This indicates that the pump doesn't have any effect on the magnetic domain structure of the Co/Pt sample.

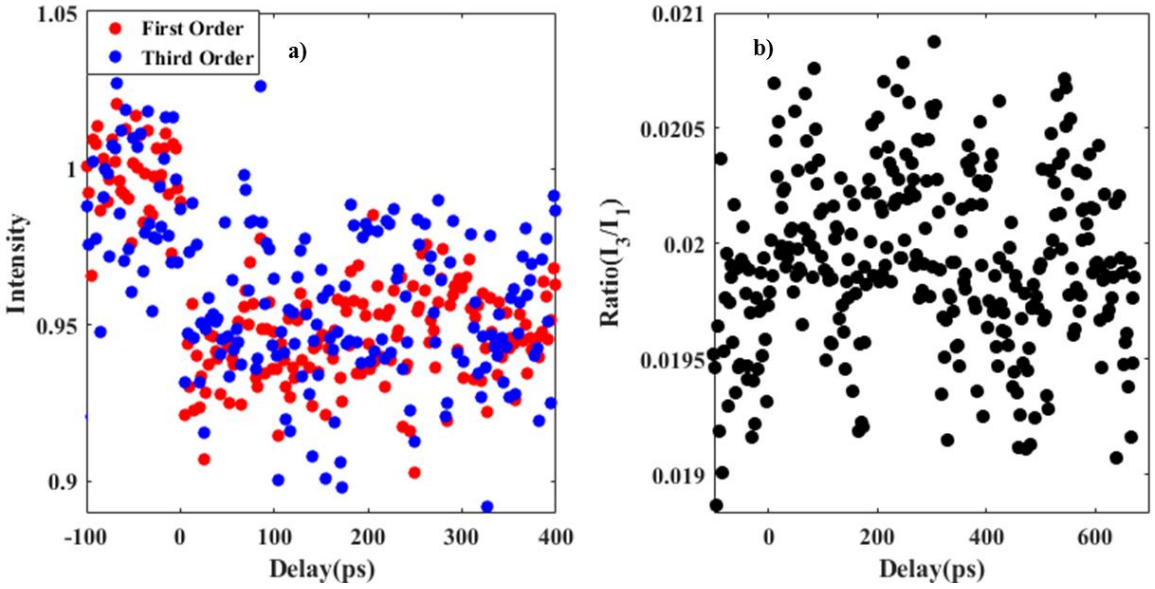

Figure 4-19: a) Ultrafast temporal evolution of the first (red) and third (blue) scattering order. b) Intenisty ratio of the 3rd and 1st scattering order as function of pump-probe time delay.

To determine the domain wall width for each time delay, we fitted the radial profile of the scattering patterns for each time delay using the corrected model developed by Hellwig *et al* [71] (see section 4.4.4.1).

In Figure 4-20.a), we plot the radial integral on logarithmic scale as function of the momentum transfer for negative delay i.e: the un-pumped sample. The solid line is the fit of the radial profile of the scattering pattern. We find a narrow maximum of the radial intensity at q peak=, which corresponds to an average domain size of 90 $\pm$5 nm. Within the uncertainties ranges, these values are in reasonable agreement with the MFM images showing a domain size of 85 nm. There is no considerable modification of the first order peak position, which implies that the domain periodicity does not change as a function of the pump probe delay. Contrary to the expansion of the CoTb domain wall, for the Co/Pt, we observe a near constant domain wall width of 21 $\pm$ 1nm (see Figure 4-20.b).

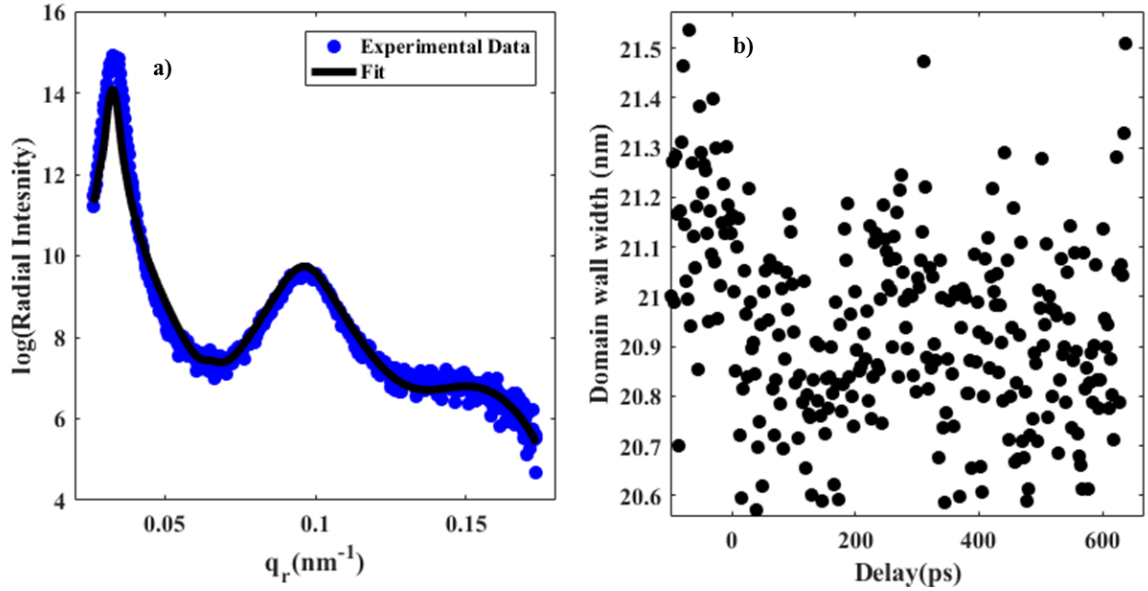

Figure 4-20: a) Radial intensity of the scattering profile pattern in a logarithmic scale. The solid line represents the fit using expression developed in[71]. b) Domain wall width as a function of pump-probe delay.

Or we show in section 4.4.3, that the domain wall width is directly linked to the uniaxial out of plane anisotropy of the thin film. For a constant wall width, we predict no change in Ku's value. This implies that the lattice heating induced by the pump pulse is not sufficient to introduce a variation of Ku. To verify this interpretation, we performed in plane SQUID-VSM measurements as a function of sample temperature. The recorded hysteresis loops are shown in Figure 4-21. One can clearly see that even for a heating temperature of 600 K, the anisotropy field shows no change. We note that we can't quantify the lattice heating by the pump laser since the beam profile was not measured at the sample position. However in this measurement the pump heating cannot exceed the 600 K.

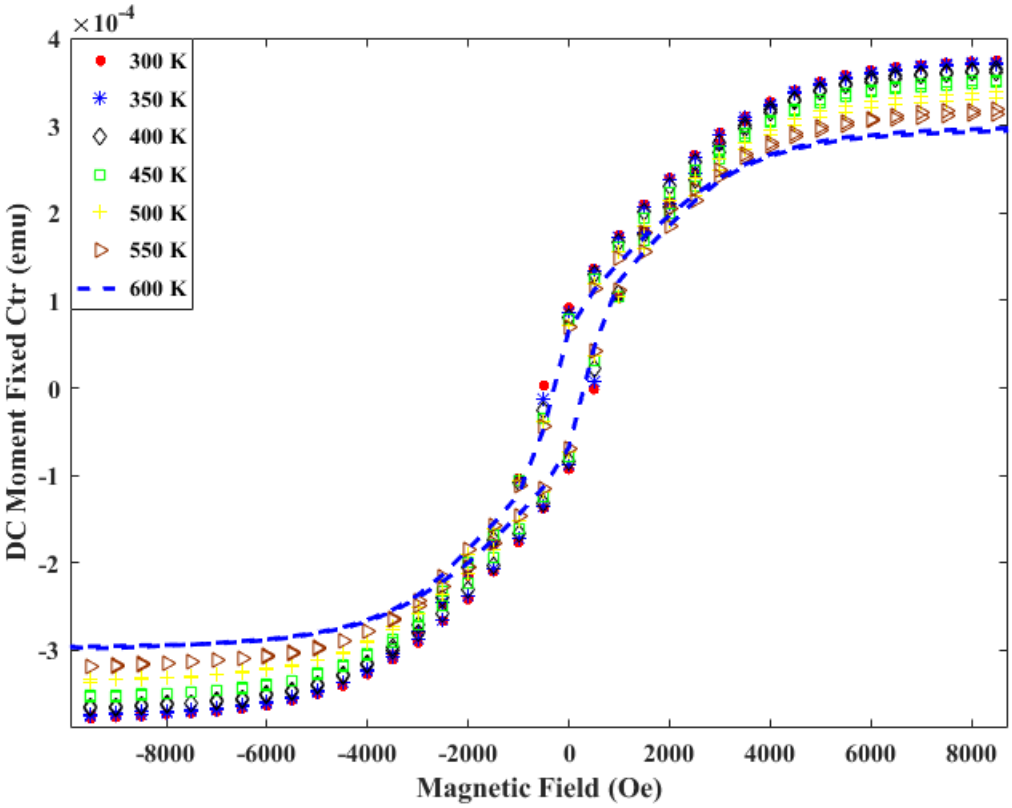

Figure 4-21: Hysteresis loop as a function of the heating temperature obtained by the SQUID-VSM measurements. Clearly, the applied field needed to saturate the magnetization of the film is constant.

4.6 Conclusion and perspectives

In conclusion, we presented in this section a time resolved resonant magnetic small angle X-ray scattering experiment performed on a $Co_{88}Tb_{12}$ alloy showing a network of stripes domains. We followed the ultrafast demagnetization dynamics of this sample using the pump probe approach. Using three different excitation fluence values, we showed that the demagnetization time of this sample is independent of the IR pump fluence. We probed different magnetization dynamics at the Co and Tb edges. We report here that the Tb magnetization doesn't show any significant recovery even ~150 ps after excitation. In order to study the ultrafast changes in the magnetic domain structure, we investigated the temporal evolution of the first and third scattering order detected at the Co M_3 edge, as well the intensity ratio of these orders. Radial scattering intensity profile extracted from the diffraction pattern reveals information about the peak position, width and intensity. We showed that the supperdiffusive spin transport between opposite domains does not induce any detectable broadening of the domain walls at the employed pump fluence. However, an intriguing phenomenon was observed after ~4 ps where the intensity of the first and third scattering order exhibits distinctly different dynamics. To interpret these observations two different models have been employed. A one dimensional model has been developed to link the ratio between different scattering order intensities to the domain width and the domain wall width.

We showed that due to thermal heating of the lattice by the pump laser, a decrease of the uniaxial anisotropy K_u sets in a few picoseconds after laser excitation. This drop in K_u leads to an increase of the domain wall width. This broadening of the domain wall is observed in the experiment as a decrease of the intensity of the third scattering order, which sets in after the partial magnetization recovery. These interpretations were verified by comparing the obtained results with a static measurement of the uniaxial anisotropy as a function of the heating temperature. We note that this dynamic has not been observed for the Co/Pt system.

In future projects, we want to perform temperature dependent Lorentz microscopy measurements. This technique offers a 10 nm spatial resolution which allows imaging of the domain wall as a function of sample temperature. This study will also provide model independent the real domain wall width. Furthermore, it is interesting to investigate the behavior of the uniaxial anisotropy for different chemical compositions of the CoTb alloy.

Bibliography

[1] E. Beaurepaire, J.-C. Merle, A. Daunois, and J.-Y. Bigot, “Ultrafast Spin Dynamics in Ferromagnetic Nickel,” *Phys. Rev. Lett.*, vol. 76, no. 22, pp. 4250–4253, May 1996.

[2] C. D. Stanciu *et al.*, “All-Optical Magnetic Recording with Circularly Polarized Light,” *Phys. Rev. Lett.*, vol. 99, no. 4, p. 047601, Jul. 2007.

[3] B. Koopmans, J. J. M. Ruigrok, F. D. Longa, and W. J. M. de Jonge, “Unifying Ultrafast Magnetization Dynamics,” *Phys. Rev. Lett.*, vol. 95, no. 26, p. 267207, Dec. 2005.

[4] M. Battiato, K. Carva, and P. M. Oppeneer, “Superdiffusive Spin Transport as a Mechanism of Ultrafast Demagnetization,” *Phys. Rev. Lett.*, vol. 105, no. 2, p. 027203, Jul. 2010.

[5] V. Shokeen *et al.*, “Role of Spin Flips versus Spin Transport in Non Thermal Electrons Excited by Ultrashort Optical Pulses in Transition Metals,” *Physical Review Letters*, vol. 119, no. 10, Sep. 2017.

[6] D. Attwood, *Soft X-Rays and Extreme Ultraviolet Radiation: Principles and Applications*, 1st ed. New York, NY, USA: Cambridge University Press, 2007.

[7] A. Mougin, M. Cormier, J. P. Adam, P. J. Metaxas, and J. Ferré, “Domain wall mobility, stability and Walker breakdown in magnetic nanowires,” *EPL*, vol. 78, no. 5, p. 57007, 2007.

[8] J. Trützschler, K. Sentosun, B. Mozooni, R. Mattheis, and J. McCord, “Magnetic domain wall gratings for magnetization reversal tuning and confined dynamic mode localization,” *Scientific Reports*, vol. 6, p. 30761, Aug. 2016.

[9] B. Pfau *et al.*, “Ultrafast optical demagnetization manipulates nanoscale spin structure in domain walls,” *Nature Communications*, vol. 3, p. 1100, Oct. 2012.

[10] T. Sant *et al.*, “Measurements of ultrafast spin-profiles and spin-diffusion properties in the domain wall area at a metal/ferromagnetic film interface,” *Scientific Reports*, vol. 7, no. 1, Dec. 2017.

[11] B. Vodungbo *et al.*, “Laser-induced ultrafast demagnetization in the presence of a nanoscale magnetic domain network,” *Nature Communications*, vol. 3, p. 999, Aug. 2012.

[12] A. Goldman, *Modern Ferrite Technology*, 2nd ed. Springer US, 2006.

[13] T. Himeno and T. Katoku, “High-density magnetic tape recording by non-tracking method,” *Journal of Magnetism and Magnetic Materials*, vol. 134, no. 2, pp. 255–261, Jun. 1994.

[14] L. Pan and D. B. Bogy, “Data storage: Heat-assisted magnetic recording,” *Nature Photonics*, vol. 3, no. 4, pp. 189–190, Apr. 2009.

[15] S. Okamoto, N. Kikuchi, M. Furuta, O. Kitakami, and T. Shimatsu, “Microwave assisted magnetic recording technologies and related physics,” *J. Phys. D: Appl. Phys.*, vol. 48, no. 35, p. 353001, 2015.

[16] M. Vopsaroiu, J. Blackburn, A. Muniz-Piniella, and M. G. Cain, “Multiferroic magnetic recording read head technology for 1Tbit/in.2 and beyond,” *Journal of Applied Physics*, vol. 103, no. 7, p. 07F506, Apr. 2008.

[17] E. Beaurepaire, G. M. Turner, S. M. Harrel, M. C. Beard, J.-Y. Bigot, and C. A. Schmuttenmaer, “Coherent terahertz emission from ferromagnetic films excited by femtosecond laser pulses,” *Appl. Phys. Lett.*, vol. 84, no. 18, pp. 3465–3467, Apr. 2004.

[18] S. Blundell, *Magnetism in condensed matter*, Reprinted. Oxford: Oxford Univ. Press, 2003.

[19] “Goudsmit on the discovery of electron spin.” [Online]. Available: https://lorentz.leidenuniv.nl/history/spin/goudsmit.html. [Accessed: 08-Sep-2018].

[20] J. Stöhr, “Exploring the microscopic origin of magnetic anisotropies with X-ray magnetic circular dichroism (XMCD) spectroscopy,” *Journal of Magnetism and Magnetic Materials*, vol. 200, no. 1–3, pp. 470–497, Oct. 1999.
[21] C. Kittel, “Introduction to Solid State Physics, 8th Edition,” p. 64.
[22] J. M. D. Coey, “Magnetism and Magnetic Materials,” p. 633.
[23] L. D. Landau, “LD Landau and EM Lifshitz, Phys. Z. Sowjetunion 8, 101 (1935).,” *Phys. Z. Sowjetunion*, vol. 8, p. 101, 1935.
[24] J. Stöhr and H.-C. Siegmann, *Magnetism: from fundamentals to nanoscale dynamics ; with 325 figures and 39 tables*. Berlin: Springer, 2006.
[25] S. Middelhoek, “Domain Walls in Thin Ni–Fe Films,” *Journal of Applied Physics*, vol. 34, no. 4, pp. 1054–1059, Apr. 1963.
[26] K. H. J. Buschow and F. R. de Boer, *Physics of Magnetism and Magnetic Materials*. Springer Science & Business Media, 2007.
[27] “(IPCMS, Strasbourg) Electron holography on Magnetic - PDF Free Download,” *dochero.tips*. [Online]. Available: https://dochero.tips/ipcms-strasbourg-electron-holography-on-magnetic.html. [Accessed: 19-Sep-2018].
[28] D. Campos and M. Flavio, “Coercivity Mechanism in Hard and Soft Sintered Magnetic Materials,” *Materials Science Forum*, 2014. [Online]. Available: https://www.scientific.net/MSF.802.563. [Accessed: 18-Aug-2018].
[29] D. D. Tang and Y.-J. Lee, *Magnetic Memory: Fundamentals and Technology*. Cambridge University Press, 2010.
[30] S. Lemerle, J. Ferré, C. Chappert, V. Mathet, T. Giamarchi, and P. Le Doussal, “Domain Wall Creep in an Ising Ultrathin Magnetic Film,” *Physical Review Letters*, vol. 80, no. 4, pp. 849–852, Jan. 1998.
[31] M. van Kampen *et al.*, “All-Optical Probe of Coherent Spin Waves,” *Phys. Rev. Lett.*, vol. 88, no. 22, p. 227201, May 2002.
[32] C. H. Back *et al.*, “Magnetization Reversal in Ultrashort Magnetic Field Pulses,” *Phys. Rev. Lett.*, vol. 81, no. 15, pp. 3251–3254, Oct. 1998.
[33] Ando et al., “Optimum condition for spin-current generation from magnetization precession in thin film systems: Applied Physics Letters: Vol 94, No 15.” [Online]. Available: http://aip.scitation.org/doi/10.1063/1.3119314. [Accessed: 23-Feb-2018].
[34] X. Ma *et al.*, “Ultrafast spin exchange-coupling torque via photo-excited charge-transfer processes,” *Nature Communications*, vol. 6, p. 8800, Oct. 2015.
[35] cwe20@cam.ac.uk, “Thin film magnetization reversal dynamics — Thin Film Magnetism Group (TFM).” [Online]. Available: https://www.tfm.phy.cam.ac.uk/Research/thin/mag-reversal. [Accessed: 18-Sep-2018].
[36] A. Vaterlaus, T. Beutler, D. Guarisco, M. Lutz, and F. Meier, “Spin-lattice relaxation in ferromagnets studied by time-resolved spin-polarized photoemission,” *Phys. Rev. B*, vol. 46, no. 9, pp. 5280–5286, Sep. 1992.
[37] A. Vaterlaus, T. Beutler, and F. Meier, “Spin-lattice relaxation time of ferromagnetic gadolinium determined with time-resolved spin-polarized photoemission,” *Phys. Rev. Lett.*, vol. 67, no. 23, pp. 3314–3317, Dec. 1991.
[38] A. Guha and P. K. Das, “q-deformed Einstein’s Model to Describe Specific Heat of Solid,” *Physica A: Statistical Mechanics and its Applications*, vol. 495, pp. 18–29, Apr. 2018.
[39] B. Koopmans *et al.*, “Explaining the paradoxical diversity of ultrafast laser-induced demagnetization,” *Nature Materials*, vol. 9, no. 3, p. nmat2593, Dec. 2009.
[40] G. Ju *et al.*, “Ultrafast nonequilibrium spin dynamics in a ferromagnetic thin film,” *Phys. Rev. B*, vol. 57, no. 2, pp. R700–R703, Jan. 1998.

[41] C. Stamm *et al.*, “Femtosecond modification of electron localization and transfer of angular momentum in nickel,” *Nature Materials*, vol. 6, no. 10, p. nmat1985, Aug. 2007.
[42] S. Essert and H. C. Schneider, “Electron-phonon scattering dynamics in ferromagnetic metals and their influence on ultrafast demagnetization processes,” *Phys. Rev. B*, vol. 84, no. 22, p. 224405, Dec. 2011.
[43] C. Illg, M. Haag, and M. Fähnle, “Ultrafast demagnetization after laser irradiation in transition metals: Ab initio calculations of the spin-flip electron-phonon scattering with reduced exchange splitting,” *Phys. Rev. B*, vol. 88, no. 21, p. 214404, Dec. 2013.
[44] K. Leckron, S. Vollmar, and H. C. Schneider, “Ultrafast spin-lattice relaxation in ferromagnets including spin-orbit fields,” *Phys. Rev. B*, vol. 96, no. 14, p. 140408, Oct. 2017.
[45] M. Battiato, K. Carva, and P. M. Oppeneer, “Theory of laser-induced ultrafast superdiffusive spin transport in layered heterostructures,” *Phys. Rev. B*, vol. 86, no. 2, p. 024404, Jul. 2012.
[46] D. Rudolf *et al.*, “Ultrafast magnetization enhancement in metallic multilayers driven by superdiffusive spin current,” *Nature Communications*, vol. 3, p. 1037, Sep. 2012.
[47] A. J. Schellekens, W. Verhoeven, T. N. Vader, and B. Koopmans, “Investigating the contribution of superdiffusive transport to ultrafast demagnetization of ferromagnetic thin films,” *Appl. Phys. Lett.*, vol. 102, no. 25, p. 252408, Jun. 2013.
[48] J.-Y. Bigot, M. Vomir, and E. Beaurepaire, “Coherent ultrafast magnetism induced by femtosecond laser pulses,” *Nat Phys*, vol. 5, no. 7, pp. 515–520, Jul. 2009.
[49] G. P. Zhang, W. Hübner, G. Lefkidis, Y. Bai, and T. F. George, “Paradigm of the time-resolved magneto-optical Kerr effect for femtosecond magnetism,” *Nature Physics*, vol. 5, no. 7, p. nphys1315, Jun. 2009.
[50] C. Boeglin *et al.*, “Distinguishing the ultrafast dynamics of spin and orbital moments in solids,” *Nature*, vol. 465, no. 7297, pp. 458–461, May 2010.
[51] E. Carpene, E. Mancini, C. Dallera, M. Brenna, E. Puppin, and S. De Silvestri, “Dynamics of electron-magnon interaction and ultrafast demagnetization in thin iron films,” *Phys. Rev. B*, vol. 78, no. 17, p. 174422, Nov. 2008.
[52] M. Fähnle, M. Haag, and C. Illg, “Is the angular momentum of a ferromagnetic sample after exposure to a fs laser pulse conserved?,” *Journal of Magnetism and Magnetic Materials*, vol. 347, no. Supplement C, pp. 45–46, Dec. 2013.
[53] B. Koopmans, “Laser-Induced Magnetization Dynamics,” in *Spin Dynamics in Confined Magnetic Structures II*, Springer, Berlin, Heidelberg, 2003, pp. 256–323.
[54] P. J. Clark, “Sputtering apparatus,” US3616450A, 26-Oct-1971.
[55] J. S. Chapin, “Sputtering process and apparatus,” US4166018A, 28-Aug-1979.
[56] M. Faraday, M. Faraday, W. Collin, Royal Society (Great Britain), and donor D. Burndy Library, *On the magnetization of light and the illumination of magnetic lines of force*. [London : The Royal Society], 1846.
[57] J. K. LL.D, “XLIII. On rotation of the plane of polarization by reflection from the pole of a magnet,” *The London, Edinburgh, and Dublin Philosophical Magazine and Journal of Science*, vol. 3, no. 19, pp. 321–343, May 1877.
[58] J. A. C. Bland, M. J. Padgett, K. D. Mackay, and A. D. Johnson, “Investigation of the magnetic properties of sandwiched epitaxial Fe and Co films using the magneto-optic Kerr effect,” *J. Phys.: Condens. Matter*, vol. 1, no. 27, p. 4407, 1989.
[59] C. KUNCSER, A. KUNCSER, and S. ANTOHE, “A DIDACTICAL PERSPECTIVE ON THE APPLICATION OF THE MAGNETO-OPTIC KERR EFFECT IN VERSATILE STUDIES OF MODERN MAGNETIC MATERIALS,” p. 11.
[60] M. Ali, “Growth and study of magnetostrictive FeSiBC thin films for device applications,” 1999.

[61] J. Zak, E. R. Moog, C. Liu, and S. D. Bader, “Fundamental magneto-optics,” *Journal of Applied Physics*, vol. 68, no. 8, pp. 4203–4207, Oct. 1990.
[62] W. K. Hiebert, A. Stankiewicz, and M. R. Freeman, “Direct Observation of Magnetic Relaxation in a Small Permalloy Disk by Time-Resolved Scanning Kerr Microscopy,” *Phys. Rev. Lett.*, vol. 79, no. 6, pp. 1134–1137, Aug. 1997.
[63] R. C. Jaklevic, J. Lambe, A. H. Silver, and J. E. Mercereau, “Quantum Interference Effects in Josephson Tunneling,” *Phys. Rev. Lett.*, vol. 12, no. 7, pp. 159–160, Feb. 1964.
[64] P. W. Anderson and J. M. Rowell, “Probable Observation of the Josephson Superconducting Tunneling Effect,” *Phys. Rev. Lett.*, vol. 10, no. 6, pp. 230–232, Mar. 1963.
[65] B. D. Josephson, “Possible new effects in superconductive tunnelling,” *Physics Letters*, vol. 1, no. 7, pp. 251–253, Jul. 1962.
[66] S. Foner, “Versatile and Sensitive Vibrating-Sample Magnetometer,” *Review of Scientific Instruments*, vol. 30, no. 7, pp. 548–557, Jul. 1959.
[67] C. Eyrich *et al.*, “Exchange stiffness in thin film Co alloys,” *Journal of Applied Physics*, vol. 111, Mar. 2012.
[68] Y. Martin and H. K. Wickramasinghe, “Magnetic imaging by ‘“force microscopy”’ with 1000 Å resolution,” *Appl. Phys. Lett.*, vol. 50, no. 20, pp. 1455–1457, May 1987.
[69] M. Gottwald, *Nouveaux systèmes modèles à aimantation perpendiculaire pour l’étude des effets de transfert de spin*. Nancy 1, 2011.
[70] W. C. Thoburn, S. Legvold, and F. H. Spedding, “Magnetic Properties of Terbium Metal,” *Phys. Rev.*, vol. 112, no. 1, pp. 56–58, Oct. 1958.
[71] O. Hellwig, G. P. Denbeaux, J. B. Kortright, and E. E. Fullerton, “X-ray studies of aligned magnetic stripe domains in perpendicular multilayers,” *Physica B: Condensed Matter*, vol. 336, no. 1–2, pp. 136–144, Aug. 2003.
[72] H. J. Albert and L. R. Rubin, “Magnetic Properties of the Platinum Metals and Their Alloys,” in *Platinum Group Metals and Compounds*, vol. 98, U. V. Rao, Ed. WASHINGTON, D. C.: AMERICAN CHEMICAL SOCIETY, 1971, pp. 1–16.
[73] X. Liu, M. Bauer, H. Bertagnolli, E. Roduner, J. van Slageren, and F. Phillipp, “Structure and magnetization of small monodisperse platinum clusters,” *Phys. Rev. Lett.*, vol. 97, no. 25, p. 253401, Dec. 2006.
[74] X. Teng, W.-Q. Han, W. Ku, and M. Hücker, “Synthesis of Ultrathin Palladium and Platinum Nanowires and a Study of Their Magnetic Properties,” *Angewandte Chemie International Edition*, vol. 47, no. 11, pp. 2055–2058, Feb. 2008.
[75] C. P. Luo and D. J. Sellmyer, “Magnetic properties and structure of Fe/Pt thin films,” *IEEE Transactions on Magnetics*, vol. 31, no. 6, pp. 2764–2766, Nov. 1995.
[76] C.-H. Lee, Y.-L. Cho, W.-P. Lee, and S.-J. Suh, “The magnetic properties and microstructure of Co-Pt thin films using wet etching process,” *J Nanosci Nanotechnol*, vol. 14, no. 11, pp. 8688–8692, Nov. 2014.
[77] P. F. Carcia, A. D. Meinhaldt, and A. Suna, “Perpendicular magnetic anisotropy in Pd/Co thin film layered structures,” *Appl. Phys. Lett.*, vol. 47, no. 2, pp. 178–180, Jul. 1985.
[78] J.-J. Samueli, “Röntgen’s discovery of X-rays,” p. 11.
[79] “History.” [Online]. Available: https://www.nde-ed.org/EducationResources/CommunityCollege/Radiography/Introduction/history.htm. [Accessed: 24-Jul-2018].
[80] “History of Synchrotron Radiation Sources.” [Online]. Available: http://xdb.lbl.gov/Section2/Sec_2-2.html. [Accessed: 24-Jul-2018].

[81] “Low-Alpha operation | French national synchrotron facility.” [Online]. Available: https://www.synchrotron-soleil.fr/en/research/sources-and-accelerators/electron-beam-parameters/low-alpha-operation. [Accessed: 24-Jul-2018].
[82] G. McFiggans, “Atmospheric science: Marine aerosols and iodine emissions,” *Nature*, vol. 433, no. 7026, pp. E13–E13, Feb. 2005.
[83] C. Marceau, T. J. Hammond, A. Y. Naumov, P. B. Corkum, and D. M. Villeneuve, “Wavelength scaling of high harmonic generation for 267 nm, 400 nm and 800 nm driving laser pulses,” *J. Phys. Commun.*, vol. 1, no. 1, p. 015009, 2017.
[84] J. Ullrich, A. Rudenko, and R. Moshammer, “Free-electron lasers: new avenues in molecular physics and photochemistry,” *Annu Rev Phys Chem*, vol. 63, pp. 635–660, 2012.
[85] L. DiMauro *et al.*, “First SASE and seeded FEL lasing of the NSLS DUV FEL at 266 and 400nm,” *Nuclear Instruments and Methods in Physics Research Section A: Accelerators, Spectrometers, Detectors and Associated Equipment*, vol. 507, no. 1, pp. 15–18, Jul. 2003.
[86] “FLASH.” [Online]. Available: https://www.fels-of-europe.eu/fel_facilities/x_ray_facilities/flash/. [Accessed: 09-Apr-2018].
[87] S. Eisebitt *et al.*, “Lensless imaging of magnetic nanostructures by X-ray spectro-holography,” *Nature*, vol. 432, no. 7019, pp. 885–888, Dec. 2004.
[88] C. von Korff Schmising *et al.*, “Generating circularly polarized radiation in the extreme ultraviolet spectral range at the free-electron laser FLASH,” *Review of Scientific Instruments*, vol. 88, no. 5, p. 053903, May 2017.
[89] E. Allaria *et al.*, “The FERMI free-electron lasers,” *J Synchrotron Rad, J Synchrotron Radiat*, vol. 22, no. 3, pp. 485–491, May 2015.
[90] E. Ferrari *et al.*, “Widely tunable two-colour seeded free-electron laser source for resonant-pump resonant-probe magnetic scattering,” *Nat Commun*, vol. 7, p. 10343, Jan. 2016.
[91] “FERMI.” [Online]. Available: https://www.fels-of-europe.eu/fel_facilities/x_ray_facilities/fermi/. [Accessed: 09-Apr-2018].
[92] D. T. Attwood, *Soft x-rays and extreme ultraviolet radiation: principles and applications*, 1. paperback version, digitally printed (with amendments). Cambridge: Cambridge Univ. Press, 2007.
[93] D. F. Swinehart, “The Beer-Lambert Law,” p. 3.
[94] G. Schütz *et al.*, “Spin-dependent extended x-ray-absorption fine structure: Probing magnetic short-range order,” *Phys. Rev. Lett.*, vol. 62, no. 22, pp. 2620–2623, May 1989.
[95] S. Valencia *et al.*, “Faraday rotation spectra at shallow core levels: 3 p edges of Fe, Co, and Ni,” *New J. Phys.*, vol. 8, no. 10, p. 254, 2006.
[96] N. G. Van Kampen and F. Lurçat, “Causalité et relations de Kramers-Kronig,” *J. Phys. Radium*, vol. 22, no. 3, pp. 179–191, 1961.
[97] E. Tamura, G. D. Waddill, J. G. Tobin, and P. A. Sterne, “Linear and Circular Dichroism in Angle Resolved Fe 3p Photoemission,” *PHYSICAL REVIEW LETTERS*, vol. 73, no. 11, p. 4, 1994.
[98] J. Kuneš and P. M. Oppeneer, “Anisotropic x-ray magnetic linear dichroism at the L 2 , 3 edges of cubic Fe, Co, and Ni: Ab initio calculations and model theory,” *Physical Review B*, vol. 67, no. 2, Jan. 2003.
[99] M. Guymont, “Structure de la matière : Atomes, liaisons chimiques et cristallographie,” p. 448.
[100] T. Brückel, “B 5 Scattering Techniques II: Magnetic X-Ray Scattering,” p. 35.
[101] F. Marsiglio, “The Harmonic Oscillator in Quantum Mechanics: A Third Way,” *American Journal of Physics*, vol. 77, no. 3, pp. 253–258, Mar. 2009.

[102] B. L. Henke, E. M. Gullikson, and J. C. Davis, “X-Ray Interactions: Photoabsorption, Scattering, Transmission, and Reflection at E = 50-30,000 eV, Z = 1-92,” *Atomic Data and Nuclear Data Tables*, vol. 54, pp. 181–342, Jul. 1993.
[103] R. de L. Kronig, “On the Theory of Dispersion of X-Rays,” *J. Opt. Soc. Am., JOSA*, vol. 12, no. 6, pp. 547–557, Jun. 1926.
[104] E. Jal, “Soft X-ray Resonant Magnetic Reflectivity : a probe for complex magnetization distribution in thin films,” Sep. 2013.
[105] J. P. Hannon, G. T. Trammell, M. Blume, and D. Gibbs, “X-Ray Resonance Exchange Scattering,” *PHYSICAL REVIEW LETTERS*, vol. 61, no. 10, p. 4, 1988.
[106] J. Schulz *et al.*, “A method to characterize electronic states of 4s ionized Rb by combined laser and synchrotron spectroscopy,” *EPL (Europhysics Letters)*, vol. 83, no. 5, p. 53001, Sep. 2008.
[107] T. Egami and S. J. L. Billinge, *Underneath the Bragg Peaks: Structural Analysis of Complex Materials*. Elsevier, 2003.
[108] C. Gutt *et al.*, “Resonant magnetic scattering with soft x-ray pulses from a free-electron laser operating at 1.59 nm,” *Phys. Rev. B*, vol. 79, no. 21, p. 212406, Jun. 2009.
[109] T. O. Menteş, C. Sánchez-Hanke, and C. C. Kao, “Reconstruction of magnetization density in two-dimensional samples from soft X-ray speckle patterns using the multiple-wavelength anomalous diffraction method,” *J Synchrotron Rad, J Synchrotron Radiat*, vol. 9, no. 2, pp. 90–95, Mar. 2002.
[110] K. Chesnel *et al.*, “X-ray resonant magnetic scattering study of the magnetic coupling in Co/Pt nanolines and its evolution under magnetic field,” *Physical Review B*, vol. 66, no. 2, Jul. 2002.
[111] B. E. Warren, *X-ray Diffraction*. Courier Corporation, 1990.
[112] T. A. Duckworth *et al.*, “Magnetic imaging by x-ray holography using extended references,” *Opt. Express, OE*, vol. 19, no. 17, pp. 16223–16228, Aug. 2011.
[113] F. Willems *et al.*, “Multi-color imaging of magnetic Co/Pt heterostructures,” *Struct Dyn*, vol. 4, no. 1, Feb. 2017.
[114] F. Capotondi *et al.*, “Invited Article: Coherent imaging using seeded free-electron laser pulses with variable polarization: First results and research opportunities,” *Review of Scientific Instruments*, vol. 84, no. 5, p. 051301, May 2013.
[115] J. Cheng and S. Han, “Phase imaging with partially coherent x rays,” *Optics Letters*, vol. 24, no. 3, p. 175, Feb. 1999.
[116] E. Allaria *et al.*, “Control of the Polarization of a Vacuum-Ultraviolet, High-Gain, Free-Electron Laser,” *Physical Review X*, vol. 4, no. 4, Dec. 2014.
[117] M. B. Danailov *et al.*, “Towards jitter-free pump-probe measurements at seeded free electron laser facilities,” *Opt. Express, OE*, vol. 22, no. 11, pp. 12869–12879, Jun. 2014.
[118] E. Pedersoli *et al.*, “Multipurpose modular experimental station for the DiProI beamline of Fermi@Elettra free electron laser,” *Review of Scientific Instruments*, vol. 82, no. 4, p. 043711, Apr. 2011.
[119] B. Vodungbo *et al.*, “Indirect excitation of ultrafast demagnetization,” *Sci Rep*, vol. 6, Jan. 2016.
[120] N. Moisan *et al.*, “Investigating the role of superdiffusive currents in laser induced demagnetization of ferromagnets with nanoscale magnetic domains,” *Scientific Reports*, vol. 4, no. 1, May 2015.
[121] G. Malinowski *et al.*, “Control of speed and efficiency of ultrafast demagnetization by direct transfer of spin angular momentum,” *Nat Phys*, vol. 4, no. 11, pp. 855–858, Nov. 2008.
[122] B. Vodungbo *et al.*, “Indirect excitation of ultrafast demagnetization,” *Scientific Reports*, vol. 6, p. 18970, Jan. 2016.

[123] V. López-Flores *et al.*, “Role of critical spin fluctuations in ultrafast demagnetization of transition-metal rare-earth alloys,” *Phys. Rev. B*, vol. 87, no. 21, p. 214412, Jun. 2013.
[124] U. Atxitia, J. Barker, R. W. Chantrell, and O. Chubykalo-Fesenko, “Controlling the polarity of the transient ferromagneticlike state in ferrimagnets,” *Phys. Rev. B*, vol. 89, no. 22, p. 224421, Jun. 2014.
[125] P. Hansen, S. Klahn, C. Clausen, G. Much, and K. Witter, “Magnetic and magneto-optical properties of rare-earth transition-metal alloys containing Dy, Ho, Fe, Co,” *Journal of Applied Physics*, vol. 69, no. 5, pp. 3194–3207, Mar. 1991.
[126] C. von Korff Schmising *et al.*, “Imaging Ultrafast Demagnetization Dynamics after a Spatially Localized Optical Excitation,” *Physical Review Letters*, vol. 112, no. 21, May 2014.
[127] C. Stamm *et al.*, “Femtosecond modification of electron localization and transfer of angular momentum in nickel,” *Nat Mater*, vol. 6, no. 10, pp. 740–743, Oct. 2007.
[128] M. Wietstruk *et al.*, “Hot-Electron-Driven Enhancement of Spin-Lattice Coupling in Gd and Tb $4f$ Ferromagnets Observed by Femtosecond X-Ray Magnetic Circular Dichroism,” *Phys. Rev. Lett.*, vol. 106, no. 12, p. 127401, Mar. 2011.
[129] N. Bergeard *et al.*, “Ultrafast angular momentum transfer in multisublattice ferrimagnets,” *Nat Commun*, vol. 5, p. 3466, Mar. 2014.
[130] I. Radu *et al.*, “Transient ferromagnetic-like state mediating ultrafast reversal of antiferromagnetically coupled spins,” *Nature*, vol. 472, no. 7342, pp. 205–208, Apr. 2011.
[131] I. Radu *et al.*, “Ultrafast and Distinct Spin Dynamics in Magnetic Alloys,” *SPIN*, vol. 05, no. 03, p. 1550004, May 2015.
[132] T. Ferté *et al.*, “Ultrafast hot-electron induced quenching of Tb 4 f magnetic order,” *Physical Review B*, vol. 96, no. 14, Oct. 2017.
[133] R. Elliott, Ed., *Magnetic Properties of Rare Earth Metals*. Springer US, 1972.
[134] S. Hendricks and E. Teller, “X-Ray Interference in Partially Ordered Layer Lattices,” *The Journal of Chemical Physics*, vol. 10, no. 3, pp. 147–167, Mar. 1942.
[135] E. E. Fullerton, I. K. Schuller, H. Vanderstraeten, and Y. Bruynseraede, “Structural refinement of superlattices from x-ray diffraction,” *Phys. Rev. B*, vol. 45, no. 16, pp. 9292–9310, Apr. 1992.
[136] A. Hubert and R. Schäfer, *Magnetic Domains: The Analysis of Magnetic Microstructures*. Springer Science & Business Media, 2008.
[137] B. A. Lilley, “LXXI. Energies and widths of domain boundaries in ferromagnetics,” *The London, Edinburgh, and Dublin Philosophical Magazine and Journal of Science*, vol. 41, no. 319, pp. 792–813, Aug. 1950.
[138] E. Jal *et al.*, “Structural dynamics during laser-induced ultrafast demagnetization,” *Phys. Rev. B*, vol. 95, no. 18, p. 184422, May 2017.
[139] J. Finley and L. Liu, “Spin-Orbit Torque Efficiency in Compensated Ferrimagnetic Cobalt-Terbium Alloys,” *arXiv:1610.09200 [cond-mat]*, Oct. 2016.
[140] R. Hasegawa, “Static bubble domain properties of amorphous Gd–Co films,” *Journal of Applied Physics*, vol. 45, no. 7, pp. 3109–3112, Jul. 1974.
[141] G. S. Cargill, “Ferromagnetism in amorphous solids,” 1975, vol. 24, pp. 138–144.
[142] Z. Q. Zou, H. Wang, and C. Yu, “A computational method of temperature characteristics of magneto-optical Kerr effect in amorphous TbFeCo films with a multilayered structure,” *Journal of Applied Physics*, vol. 93, no. 9, pp. 5268–5273, Apr. 2003.
[143] K. Baberschke, “Anisotropy in Magnetism,” in *Band-Ferromagnetism*, vol. 580, K. Baberschke, W. Nolting, and M. Donath, Eds. Berlin, Heidelberg: Springer Berlin Heidelberg, 2001, pp. 27–45.

[144] D. Afanasiev, B. A. Ivanov, R. V. Pisarev, A. Kirilyuk, T. Rasing, and A. V. Kimel, "Femtosecond single-shot imaging and control of a laser-induced first-order phase transition in $HoFeO_3$," *Journal of Physics: Condensed Matter*, vol. 29, no. 22, p. 224003, Jun. 2017.

Annexes -1– Control of the polarization at Flash

The polarizer configuration consists of four metallic mirrors as shown in figure 45. This device does not modify the beam position and the pointing of FLASH1 pulses, but converts the initially linear polarization into a high degree of circular polarization. The whole assembly can be rotated around the beam axis (±60°). The device is placed in an ultra-high vacuum chamber which can avoid any accumulative carbon contamination of the mirrors.

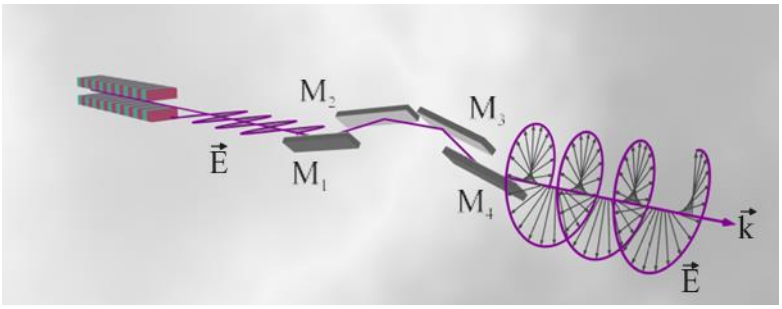

Figure 0-1: Illustration of the four mirror polarizer.

To verify the polarizer functionality, Fourier transform holography experiment of nanoscale magnetic domains was performed at FLASH1. Ferromagnetic materials like Fe, Co and Ni (presenting maze domains structure) were investigated where holograms for circularly right and circularly left polarized XUV pulses were recorded. We note that the difference in detected intensity between two holograms obtained for opposite light helicity is proportional to the magnetization. In figure 46-a) we show the difference hologram showing a pronounced magnetic speckle. Calculating the two dimensional Fourier transforms of these holograms, we get the real space image of the magnetic domain pattern as shown in Figure 0-2-b). We can see the out of plane magnetic domains in opposite direction as black and white contrast.

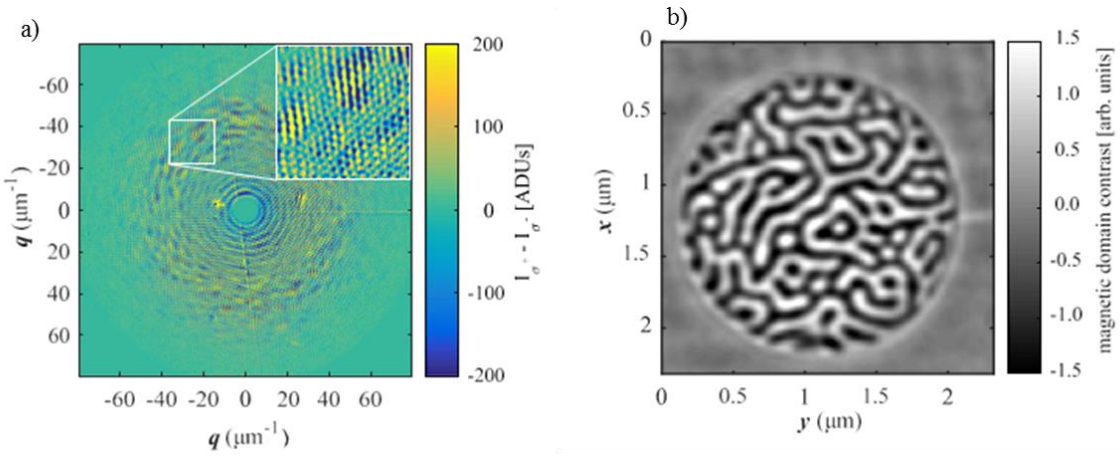

Figure 0-2: a) Difference hologram between signal recorded for opposite circular helicity b) Reconstruction of the hologram using the 2Dimensional Fourier transform

Table des illustrations

[Modification ultrarapide de l'anisotropie magnétique dans un alliage CoTb]

Résumé :
Dans cette thèse, nous rapportons l'évolution temporelle du premier et du troisième ordre de la diffusion magnétique d'un film CoTb amorphe après une excitation femtoseconde. Ces résultats sont obtenus en appliquant une diffusion résonnants de rayons X aux petits angles au seuil d'absorption magnétique de Co M3 via des expériences de pompe sonde répétitives. Une différence de comportement entre le premier et le troisième ordre de diffusion a été observée après 3,5 ps, où une seconde baisse de l'intensité du troisième ordre apparaît. En utilisant des modèles appropriés, nous montrons que cette différence est due à une augmentation de la largeur de la paroi du domaine séparant deux domaines opposés. Nous supposons que cet élargissement de la paroi est généré par une variation de l'anisotropie uniaxiale hors plan due au réchauffement thermique du réseau par l'impulsion laser femtoseconde. Cette interprétation est vérifiée en mesurant l'anisotropie uniaxiale en fonction de la température de chauffage en effectuant des mesures statiques SQUID-VSM.

Mots clés : [Désaimantation ultrarapide, CoTb, paroi de domaine, diffusion magnétique résonnante, anisotropie uni-axiale, transport supper diffusif]

[Ultrfast modification of the magnetic anisotropy in a CoTb alloy]

Abstract :
In this thesis, we report the time evolution of first and third order of magnetic scattering from an amorphous CoTb film after a femtosecond excitation. These results are obtained by applying a resonant small angle X ray scattering at the Co magnetic absorption edge M3 via a repetitive pump probe experiments. Difference in behaviours between the first and third scattering orders was observed after 3.5 ps where a second drop of the third order intensity appears. Using suitable models, we show that this difference is due to an increase of the domain wall width separating two opposite domains. We suppose that this wall broadening is generated by the variation of the out of plane uniaxial anisotropy due to the thermal heating of the lattice by the femtosecond laser pulse. This interpretation is verified by following the uniaxial anisotropy as function of the heating temperature by doing static SQUID-VSM measurements.

Keywords : [Ultrafast Demagnetization, CoTb, domain wall, resonant magnetic scattering, uniaxial anisotropy, supper diffusive transport]